

Air Force Institute of Technology

**AFIT Scholar**

---

Theses and Dissertations

Student Graduate Works

---

12-22-2011

## Electroluminescence studies on longwavelength indium arsenide quantum dot microcavities grown on gallium arsenide

John C. Ramsey

Follow this and additional works at: <https://scholar.afit.edu/etd>



Part of the [Other Engineering Commons](#), and the [Plasma and Beam Physics Commons](#)

---

### Recommended Citation

Ramsey, John C., "Electroluminescence studies on longwavelength indium arsenide quantum dot microcavities grown on gallium arsenide" (2011). *Theses and Dissertations*. 1148.

<https://scholar.afit.edu/etd/1148>

This Thesis is brought to you for free and open access by the Student Graduate Works at AFIT Scholar. It has been accepted for inclusion in Theses and Dissertations by an authorized administrator of AFIT Scholar. For more information, please contact [richard.mansfield@afit.edu](mailto:richard.mansfield@afit.edu).



**ELECTROLUMINESCENCE STUDIES ON  
LONG WAVELENGTH INDIUM ARSENIDE  
QUANTUM DOT MICROCAVITIES GROWN  
ON GALLIUM ARSENIDE**

THESIS

John C. Ramsey

AFIT/GE/ENG/11-46

**DEPARTMENT OF THE AIR FORCE  
AIR UNIVERSITY**

**AIR FORCE INSTITUTE OF TECHNOLOGY**

---

**Wright-Patterson Air Force Base, Ohio**

APPROVED FOR PUBLIC RELEASE; DISTRIBUTION IS UNLIMITED

The views expressed in this thesis are those of the author and do not reflect the official policy or position of the United States Air Force, Department of Defense, or the United States Government. This material is declared a work of the U.S. Government and is not subject to copyright protection in the United States.

AFIT/GE/ENG/11-46

ELECTROLUMINESCENCE STUDIES ON LONGWAVELENGTH INDIUM  
ARSENIDE QUANTUM DOT MICROCAVITIES GROWN ON GALLIUM  
ARSENIDE

THESIS

Presented to the Faculty

Department of Electrical and Computer Engineering

Graduate School of Engineering and Management

Air Force Institute of Technology

Air University

Air Education and Training Command

In Partial Fulfillment of the Requirements for the  
Degree of Master of Science in Electrical Engineering

John C. Ramsey, B.S.E.E.

December 2011

APPROVED FOR PUBLIC RELEASE; DISTRIBUTION IS UNLIMITED

ELECTROLUMINESCENCE STUDIES ON LONGWAVELENGTH INDIUM  
ARSENIDE QUANTUM DOT MICROCAVITIES GROWN ON GALLIUM  
ARSENIDE

John C. Ramsey, B.S.E.E.

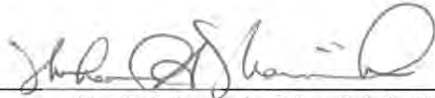
Approved:



Dr. Ronald A. Coutu, Jr. (Advisor)

23 NOV 11

date



Dr. Michael A. Marciniak (Member)

31 Oct 11

date



Dr. William J. Siskamnetz (Member)

20111110

date

### Abstract

A comprehensive study of the electroluminescence of four longwavelength microcavity devices with InAs/GaInAs quantum dot active regions emitting near 1.3  $\mu\text{m}$  was conducted. The four molecular beam epitaxial grown samples with AlAs oxide aperture confinement layers were fabricated, characterized, and optically modeled. Optical power transmission of the samples was modeled using Matlab and compared with actual measured transmission data. Resonant cavity light emitting diodes (RCLEDs) and three 1.3  $\mu\text{m}$  vertical cavity surface emitting laser (VCSEL) samples were fabricated and electro-optically characterized over a range of injection currents and temperatures. An intra-cavity contacted VCSEL photolithographic mask set was designed and created for this study.

Devices achieved continuous wave room temperature lasing at 1.28 $\mu\text{m}$  with an output power of more than 3 mW, a threshold current of 2.3 mA, and a slope efficiency of 10.3 W/A. The characteristic temperature was 49.4 K and the wall plug efficiency was a maximum of over 36%. This was made possible by the optical and current confinement of the Al<sub>2</sub>O<sub>3</sub> apertures that provided a beneficial impact on the device output efficiency. The FWHM of the quantum dot active region was 27 meV with a separation of 62 eV between the peak of the ground state and excited state transitions. The minimum threshold current was observed at a chuck temperature of -10°C, and did not occur at the point where the peak of the gain curve and cavity resonance were matched (10°C). The cavity resonance of the VCSEL was tuned at a wavelength too short for the peak wavelength of the active region gain curve limiting the temperature at which the VCSELs produced lasing to about room temperature.

## **Acknowledgement**

I would like to thank my committee members, Dr. Bill Siskaninetz, Dr. Ronald Coutu, and Dr. Michael Marciniak for their assistance and the extraordinary amount of patience displayed during this effort. I would also like to thank Dr. James Lott for acquiring the materials necessary for this study, and his technical guidance as my initial advisor.

I would especially like to thank Dr. Siskaninetz for supervising and performing a majority of the device fabrication in the AFRL clean room. Finally, I would like to thank Dr. Coutu for his patience and his role as my advisor through the completion of this study.

John C. Ramsey

## Table of Contents

	Page
Abstract .....	iv
Acknowledgments .....	v
List of Figures .....	viii
List of Tables .....	xiv
I. Introduction .....	1
1.1 Motivation.....	1
1.2 Scope.....	2
1.3 Main Results .....	3
1.4 Thesis Organization .....	3
II. Background.....	5
2.1 Microcavity Device Structure .....	5
2.2 Distributed Bragg Reflectors .....	7
2.3 Optical Characteristics of Microcavities.....	17
2.4 Quantum Dots .....	24
2.4.1 Quantum Dot Active Regions .....	25
2.4.2 Quantum Dot Density of States .....	27
2.4.3 Quantum Dot Spectral Characteristics.....	29
2.5 Quantum Dot Laser Characterization and Temperature Effects .....	34
2.6 Transverse VCSEL Cavity Modes .....	39
III. Fabrication and Experimental Methodology .....	41
3.1 Introduction.....	41
3.2 Mask Set Design .....	42
3.3 Device Fabrication .....	45
3.3.1 RCLED (SH118) Fabrication.....	47
3.3.2 VCSEL V17 Fabrication.....	50
3.3.3 VCSEL V17A Fabrication .....	53
3.3.4 VCSEL V19 Fabrication.....	55
3.3.5 Through DBR Contacted VCSEL Fabrication.....	57
3.4 Optical Power Transmission Measurements.....	63
3.5 Electro-Luminescence Measurements .....	64
3.6 Optical Power, Current and Voltage (L-I-V) Measurements .....	65
3.7 Conclusions.....	65



	Page
IV. Results and Analysis .....	66
4.1 Introduction.....	66
4.2 Optical Power Transmission Measurements.....	66
4.3 Electroluminescence of RCLEDs and VCSELs .....	73
4.4 Temperature Effects on Electroluminescence of RCLEDs and VCSELs....	81
4.5 Lasing and Cavity Characteristics of VCSELs .....	87
4.6 Temperature Effects on LIV Curves and VCSEL Threshold Current .....	93
4.7 Summary of Results .....	101
V. Conclusions and Recommendations .....	103
Bibliography.....	105

## List of Figures

Figure	Page
2.1. Structure of a typical RCLED.....	6
2.2. (a) Structure of a through DBR contacted VCSEL and (b) an intra-cavity contacted VCSEL .....	6
2.3. Constructive interference in a (a) top DBR mirror and a (b) bottom DBR mirror .....	8
2.4. Calculated power reflectance, transmittance, and absorptance of a DBR reflector with 29 periods of GaAs and Al <sub>0.9</sub> Ga <sub>0.1</sub> As .....	13
2.5. Indices of refraction of GaAs (a) and Al <sub>0.9</sub> Ga <sub>0.1</sub> As (b) versus wavelength.....	13
2.6. Power reflectance at the design wavelength of a GaAs/Al <sub>0.9</sub> Ga <sub>0.1</sub> As DBR versus the number of periods in the DBR .....	14
2.7. Power reflectance versus wavelength for refractive index differences between the high and low index layers of a DBR (20 periods and $n_L = 2.5$ ) .....	15
2.8. Calculated power reflectance versus wavelength of GaAs/Al <sub>0.9</sub> Ga <sub>0.1</sub> As DBRs with different numbers of periods .....	16
2.9. Power transmission of $2\lambda$ and $6\lambda$ ( $L_c$ ) resonant cavities versus wavelength ( $\lambda_{\text{design}} = 1300$ nm, $R_1 = R_2 = 0.95$ ).....	18
2.10. Power transmission of a $6\lambda$ ( $L_c$ ) resonant cavity versus wavelength for mirrors with various values of reflectance ( $R_1 = R_2 = R$ ) .....	19
2.11. Power transmission of a $6\lambda$ ( $L_c$ ) resonant cavity and the stop band of a typical microcavity DBR versus wavelength.....	20
2.12. Calculated reflectance and transmittance versus wavelength of $6\lambda$ ( $L_c$ ) RCLED with a 12 period DBR ( $\lambda_{\text{design}} = 1300$ nm) .....	21
2.13. Modeled reflectance, transmittance and absorption versus wavelength of $6\lambda$ ( $L_c$ ) through-DBR VCSEL with a 27 period top DBR, a 33 period bottom DBR.....	22

Figure	Page
2.14. Electric field intensity and the refractive index profile verses distance in the $2\lambda$ microcavity VCSEL structure calculated using Matlab routines [Ochoa].....	23
2.15. Illustration of the DBR penetration depth. (a) DBR consisting of two materials of thickness $L_1$ and $L_2$ . (b) Ideal (metallic) reflector displaced by the penetration depth [16] .....	24
2.16. Cut away views of three different modes of epitaxial growth as a function of the coverage, $\theta$ in monolayers (ML): (a) island or Volmer-Weber growth; (b) layer-plus-island, or Stranski-Krastanov growth; (c) layer-by-layer, or Frank-van der Merwe growth [18].....	26
2.17. Active region of diode lasers representing a layer of bulk semiconductor (a), several quantum wells (b), an array of quantum wires (c), and an array of quantum dots (d) and the corresponding density of states [17] .....	29
2.18. Bandgap energies and lattice constants of III-V material systems for various material composition [16] .....	30
2.19. Calculated electronic structure of an InAs pyramidal quantum dot with a base size of 12 nm with a 1.7 ML wetting layer and capped with GaAs unstrained on the left, and GaAs with a uniform biaxial strain on the right [23].....	31
2.20. Theoretical transition energy versus quantum dots size for electron ground state to hole states with the wetting layer transition [23] .....	32
2.21. EL spectrum (at room temperature) of a InAs/InGaAs QD active Region with energy level separation ( $\Delta E$ ) and FWHM ( $\sigma$ ) shown .....	33
2.22. LIV curve of a QD VCSEL used to determine threshold current and slope efficiency.....	35
2.23. Temperature dependences of the EL peak position measured at low current density ( $\Delta$ ), VCSEL lasing wavelength ( $\blacksquare$ ), and gain-peak wavelength ( $\bullet$ ) at threshold currently density of the VCSEL. $T_G^*$ is the temperature at which there is zero cavity-gain detuning [29] .....	38

Figure	Page
3.1. AFIT/AFRL Intracavity contact VCSEL mask with optical drop out and 29 blocks of microcavity devices .....	42
3.2. AFIT/AFRL Intracavity contact VCSEL mask .....	43
3.3. SH118 RCLED device structure .....	48
3.4. Refractive index and reflectance versus etch depth for SH118 RCLED devices.....	49
3.5. Profilometer measurement graph for SH118 RCLED devices .....	50
3.6. V17 VCSEL device structure.....	51
3.7. Refractive index and reflectance versus etch depth for V17 VCSEL devices.....	52
3.8. Refractive index and reflectance versus etch depth for V17A VCSEL devices.....	53
3.9. Profilometer measurement of sample V17A after top mesa (6.3 $\mu\text{m}$ ), top metal contact deposition, and the first middle mesa etch (1.6 $\mu\text{m}$ ) .....	54
3.10. Profilometer measurement of sample V17A after top mesa, top metal contact deposition, and the first and second middle mesa etch.....	55
3.11. V19 VCSEL device structure.....	56
3.12. Refractive index and reflectance versus etch depth for V19 VCSEL devices.....	57
3.13. NSC-336 VCSEL device structure .....	59
3.14. Refractive index and reflectance versus etch depth for NSC-336 VCSEL device.....	60
3.15. Total Profilometer measurement of a completed NSC-336 VCSEL device with bottom metal contacts.....	60
3.16. Do177eB VCSEL device structure .....	61

Figure	Page
3.17. Refractive index and reflectance versus etch depth for Do177eB VCSEL device.....	62
3.18. Optical power transmission measurement setup.....	64
4.1. Optical Power Transmission Measured for Various Samples Studied .....	67
4.2. Measured power transmission of VCSEL V17 compared to modeled data with nominal values and adjusted values (reduced by a factor of 0.9985) for the layer thicknesses.....	68
4.3. Measured power transmission of VCSEL NSC336 compared to the modeled data .....	69
4.4. Measured power transmission of VCSEL DO177 compare to the modeled data .....	70
4.5. Measured power transmission of VCSEL V17 at points across a section of the wafer.....	71
4.6. Measured power transmission of VCSEL NSC336 at four points across the wafer surface .....	72
4.7. Measured power transmission of VCSEL DO177 at various points on the wafer showing the variability in layer thickness .....	73
4.8. Electroluminescence of a 50um RCLED (SH118) versus drive current showing the rise of excited state transitions and red shift as the current increases .....	74
4.9. FWHM of the EL spectrum versus current of a 50um RCLED (SH118) at room temperature and the photon energy at the low and high ends of the FWHM versus drive current .....	75
4.10. Electroluminescence of a 17um RCLED (SH118) at various drive currents showing the rise of excited state transitions and red shift as the current increases.....	76
4.11. Output of a 25 $\mu\text{m}$ V17 VCSEL prior to oxidation of the oxide aperture at drive currents of 5 mA and 15 mA, and after 80 minutes of oxidation at a current of 5 mA.....	77

Figure	Page
4.12. EL of VCSEL V17 with a 25 $\mu\text{m}$ diameter versus drive current.....	78
4.13. Output of a square shaped VCSEL NSC336 with a diameter of 35 $\mu\text{m}$ prior to oxidation of the oxide aperture at drive currents of 5 mA and 15 mA, and after oxidation at 5 mA .....	79
4.14. EL output of a square shaped NSC336 VCSEL versus drive current.....	80
4.15. Output of a 35 $\mu\text{m}$ VCSEL NSC336 measured with an optical spectrum analyzer at 0.1 nm resolution to measure the lateral modes of the cavity compared with the output measured with 1 nm bandwidth resolution.....	81
4.16. Output of a SH118 RCLED at various chuck temperatures .....	82
4.17. Peak energy levels of the ground state (GS) and excited state (ES) of the QD active region of a 50 $\mu\text{m}$ RCLED (SH118) versus chuck temperature .....	84
4.18. FWHM of the QD active region of a 50 $\mu\text{m}$ diameter RCLED (SH118) in meV and the high and low end points at half maximum versus the device chuck temperature .....	84
4.19. Effect of temperature on the cavity resonant peak of circular VCSEL (V17) with a diameter of 20 $\mu\text{m}$ ( $6\lambda$ cavity).....	85
4.20. Shift in the gain curve and cavity resonant wavelength of VCSEL V17 verses the device chuck temperature.....	86
4.21. Output of a DO177 VCSEL at drive currents of 250 $\mu\text{A}$ , 5 mA and 10 mA prior to oxidation and after oxidation of the oxide aperture .....	87
4.22. Output of a 15 $\mu\text{m}$ diameter DO177 VCSEL at 4 mA compared to the optical transmission of the wafer .....	88
4.23. LIV curve of a 15 $\mu\text{m}$ DO177 VCSEL at room temperature showing very weak lasing activity .....	89
4.24. Output of a 50 $\mu\text{m}$ DO177 VCSEL after 20 minutes of oxidation of the oxide aperture .....	90

Figure	Page
4.25. Output of a 25 $\mu\text{m}$ DO177 VCSEL at room temperature (25°C) with a threshold current of 2.65 mA .....	91
4.26. LIV of a 25 $\mu\text{m}$ DO177 VCSEL at a chuck temperature of 25°C.....	92
4.27. LIV of a 25 $\mu\text{m}$ DO177 VCSEL at a chuck temperature of 21°C (room temperature) with $I_{\text{th}}$ of 2.3 mA and slope efficiency of 10.3 W/A .....	92
4.28. LIV plots of a 25 $\mu\text{m}$ DO177 VCSEL over a range of chuck temperatures (T).....	93
4.29. LIV plot of a 25 $\mu\text{m}$ DO177 VCSEL at a chuck temperature of -30°C with markers where the output spectrum was measured .....	94
4.30. Multimode output spectrum of a 25 $\mu\text{m}$ DO177 VCSEL at a chuck temperature of -30°C at various drive currents.....	95
4.31. LIV plots of a 25 $\mu\text{m}$ DO177 VCSEL over various chuck temperatures .....	96
4.32. LIV plots of a 25 $\mu\text{m}$ DO177 VCSEL over various chuck temperatures at and around the threshold current level .....	97
4.33. Threshold current and slope efficiency of a 25 $\mu\text{m}$ DO177 VCSEL over various chuck temperatures.....	98
4.34. Characteristic temperature of a 25 $\mu\text{m}$ DO177 VCSEL over various chuck temperatures .....	99
4.35. Output of a 15 $\mu\text{m}$ DO177 VCSEL at $I_d = 4$ mA over various chuck temperatures in a log scale .....	100
4.36. Cavity resonance wavelength of a 15 $\mu\text{m}$ DO177 VCSEL at $I_d = 4$ mA versus chuck temperature .....	101

## List of Tables

Table	Page
3.1. Summary of Micro-cavity Device Fabrication and Experimentation .....	41
3.2. Reactive Ion Etch Data .....	47
3.3. Oxidation Furnace Data .....	47
3.4. Reactive Ion Etch Data for Patterning and Removing Si <sub>3</sub> N <sub>4</sub> Masks .....	58



# ELECTROLUMINESCENCE STUDIES ON LONGWAVELENGTH INDIUM ARSENIDE QUANTUM DOT MICROCAVITIES GROWN ON GALLIUM ARSENIDE

## I. Introduction

Quantum dots offer the potential for enhancing the performance of devices converting electrons to photons and vice versa, and the number of applications continues to grow as research uncovers new possibilities. One such application, the long wavelength semiconductor laser, is important to telecommunication, infrared imaging, and remote gas sensing. In addition to this, vertical cavity surface emitting lasers (VCSELs) offer many advantages over alternative types of lasers including wavelength tunable cavities, low operating current and voltage, single longitudinal mode cavities, direct high speed modulation, and efficient optical coupling. VCSELs are also more compact, and have the ability to be easily manufactured into one and two dimensional arrays of lasers for high speed parallel fiber optic (FO) links. Research in quantum dots has demonstrated that quantum dots have the potential to provide tremendous benefits to applications such as photovoltaic cells, optical/infrared detectors, optical storage devices, lasers, and other optical sources. Despite these advantages, much more research is required to develop consistent and reliable methods of producing a precisely and uniformly sized distribution of quantum dots necessary for these applications.

### 1.1 Motivation

Although VCSELs have been in research since 1977, fabricating quantum dots (QDs) to produce the desired optical properties for practical devices still presents a

challenge. Developing quantum dot VCSEL active regions is hampered by difficulties in modeling quantum dots, and the time consuming experimental trial and error required to develop fabrication techniques necessary for creating the desired size, shape and uniformity of quantum dot ensembles. Although QD VCSELs have many benefits previously mentioned, they still have issues with light and current confinement in the active region, high power operation, multiple transverse modes, and temperature sensitivity. Developing an efficient, high power, single mode quantum dot VCSEL, and other QD microcavity devices along with a reproducible quantum dot active region will enable many applications such as high speed multi-channel fiber optic communication links using VCSEL arrays [1, 2], medical imaging using super luminescent diodes [3], and tunable lasers capable of remotely sensing gases and biological agents [4, 5]. In addition to these microcavity device applications, developing quantum dot technology has the potential to increase the efficiency of solar cells [6, 7, 8], vastly improve photo detector sensitivity [9], and provide optical memory storage densities predicted to be terabits per square inch [10, 11]. However, the technology used to make quantum dot materials must be developed further through experimentation. Growing self-assembled quantum dots and characterizing the dots in microcavity devices can help to develop ways of consistently growing a more closely sized ensemble of quantum dots that is key to enabling many applications previously mentioned.

## 1.2 Scope

This study includes the fabrication, characterization and optical modeling of microcavity devices with InAs quantum dot active regions emitting light at a wavelength near 1.3  $\mu\text{m}$ . Methods of fabrication were developed for a class 100 clean room. Optical properties of the devices fabricated were modeled using Matlab and compared with measured results. Characterization of the microcavity devices included analysis of the

effects of temperature, injection current and device structure on the optical output. The results were analyzed in order to provide feedback for future device fabrication and wafer growth. However, new wafers were not grown using the analysis results during this study.

### **1.3 Main Results**

Vertical cavity surface emitting lasers with aluminum oxide InAs quantum dot active regions emitting at  $1.28\mu\text{m}$  were fabricated and characterized. The VCSELs demonstrated continuous wave lasing at room temperature at power levels above 3 mW with a threshold current of 2.3mA and slope efficiency of 10.3 mW/mA. The optical characteristics of GaAs/InGaAs VCSEL structures were characterized and modeled in Matlab to enable the development of more efficient device structures that are better matched to the output characteristic of quantum dot active regions. InAs quantum dot active regions emitting near  $1.3\mu\text{m}$  and the effects of current and temperature were characterized enabling the development of more efficient QD microcavity devices. Fabrication methods were developed for these devices that enable the fabrication of large 2D arrays of VCSEL devices for applications in high speed optical communications.

### **1.4 Thesis Organization**

Chapter II contains background information on distributed Bragg reflectors (DBRs), multilayer Fabry-Perot etalons, quantum dot laser gain layers, self-assembled quantum dot growth and micro-cavity devices. First, a brief description of the basic structure of microcavity devices is presented. Second, the optical properties of DBRs and how to model those properties is presented. Next, the optical properties of microcavity devices are described by relating them to a Fabry-Perot etalon. Then, a description of quantum dot fabrication and output characteristics is given. In addition to describing

quantum dot gain regions, oxide aperture layers and their benefits are discussed. Finally, chapter II describes the methods used to characterize semiconductor laser devices in this study.

Chapter III describes the fabrication process used to create the micro-cavity devices studied. Material growth methods and processes are described. The actual fabrication process is discussed including the device mask set and mask set design, oxidation of current apertures, equipment used and methods. Lastly, experimental setups are described for obtaining LIV data, electro-luminescence data and optical transmission data.

In Chapter IV, the results of the experiments are presented, analyzed and compared with luminescence data. Light emitting diode (LED) and laser device outputs are characterized.

Chapter V summarizes results, states conclusions, and makes recommendations for further study.

## II. Background

Long wavelength InAs quantum dot microcavity devices are composed of complex semiconductor material structures that precisely balance optical, electrical and thermal properties. Wavelength selective and highly reflective laser cavity mirrors are necessary to amplify the light generated by the extremely thin gain region of the cavity. The quantum dot active region in the devices must emit light strongly at the resonant wavelength of the optical cavity. The structure of the microcavity device must promote both optical and electrical current confinement to produce light efficiently and only at the desired wavelength. At the same time, the materials must be thermally conductive to transfer heat from the cavity region. Excess heat shifts the QD gain peak away from the cavity resonance, increases losses in the cavity, and reduces the reliability and efficiency of the devices. In the following paragraphs, the physics and techniques used to design and fabricate microcavity devices are described.

### 2.1 Microcavity Device Structure

Vertical cavity surface emitting lasers (VCSELs) and resonant cavity light emitting diodes (RCLEDs) are composed of an active region sandwiched between two reflectors and are composed of semiconductor layers grown vertically on a standard GaAs wafer. An RCLED has a top reflector that is merely composed of the GaAs-to-air boundary and has a typical reflectance of about 0.3 that is relatively constant across the range of wavelengths emitted by the device. This provides some resonance and enhances the optical output of the active region without distorting the actual light emitted by the active region. The structure of an RCLED is shown in Figure 2.1 and consists of a GaAs cavity with AlAs oxide layers, an active region of InAs quantum dots, and a bottom

reflector called a Distributed Bragg Reflector (DBR). Metal contacts are typically deposited on the top of the cavity and on the backside of the wafer.

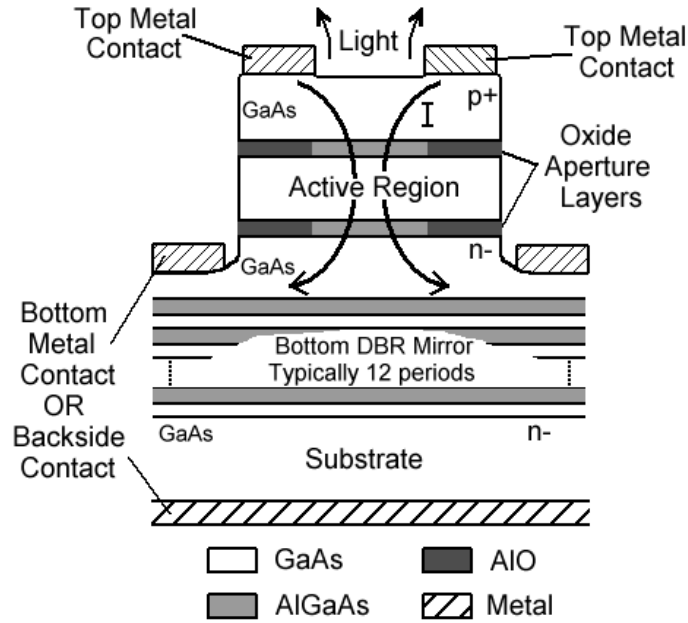


Figure 2.1: Structure of a typical RCLED

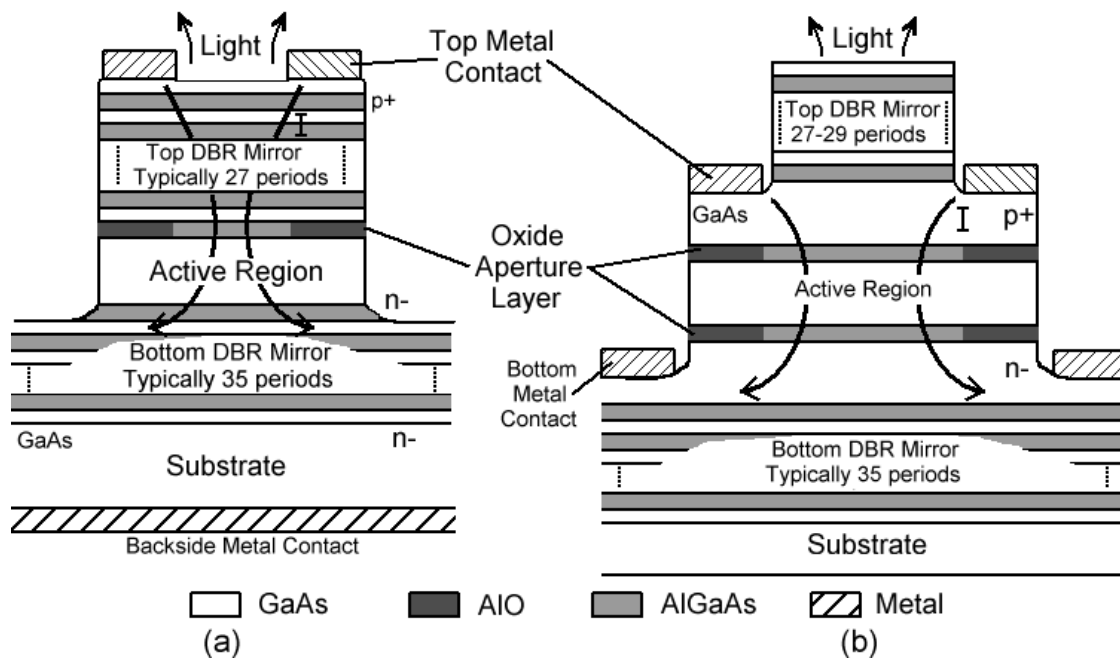


Figure 2.2: (a) Structure of a through DBR contacted VCSEL and (b) an intra-cavity contacted VCSEL

A VCSEL is similar to an RCLED but VCSELs have DBR mirrors above and below the cavity region. The metal contacts on VCSELs can either be on top of the top DBR and on the backside of the wafer in the case of “Through DBR” contacts or deposited on a mesa etched into the cavity in the case of “Intra-cavity” contacted VCSELs. Figure 2.2 shows the structure of both through DBR and intracavity contacted VCSELs. The etched mesa design provides both current and optical confinement within the microcavity of the device. The AlAs layers within the microcavity are easily oxidized to a non-conductive aluminum oxide ( $\text{Al}_2\text{O}_3$ ) with the application of heat and water vapor. These “Oxide” layers are generally located at anti-nodes in the electric field, and provide additional current and optical confinement.

## 2.2 Distributed Bragg Reflectors

Distributed Bragg Reflectors (DBRs) are used in vertically emitting microcavity devices because highly reflective mirrors are required to amplify light from the extremely thin optical gain regions. DBRs work on the principle of constructive interference of lightwaves reflecting off the interfaces between dielectric material layers of specific composition and thickness. Another name for a DBR is a quarter wave stack because the alternating layers of material with a high index of refraction and a low index of refraction are each a quarter of a wavelength thick. The stacked layers are arranged in alternating high and low indices of refraction, so reflections at consecutive boundaries alternate between internal and external. There is a  $\pi$  ( $180^\circ$ ) phase shift for TE waves externally reflected and no phase shift for internally reflected TE waves [12]. Figure 2.3 shows how constructive interference occurs in two different quarter wave stacks representing the top and bottom mirrors of an optical microcavity. Mathematical treatment of DBRs begins by considering the boundary conditions at each interface where the Fresnel Equations describe the relationship between the electric fields of the light on both sides of the

interface. At normal incidence the Fresnel Equations for the reflection and transmission coefficients are given by [13]

$$r_x = \frac{n_1 - n_2}{n_1 + n_2} \quad (2.1)$$

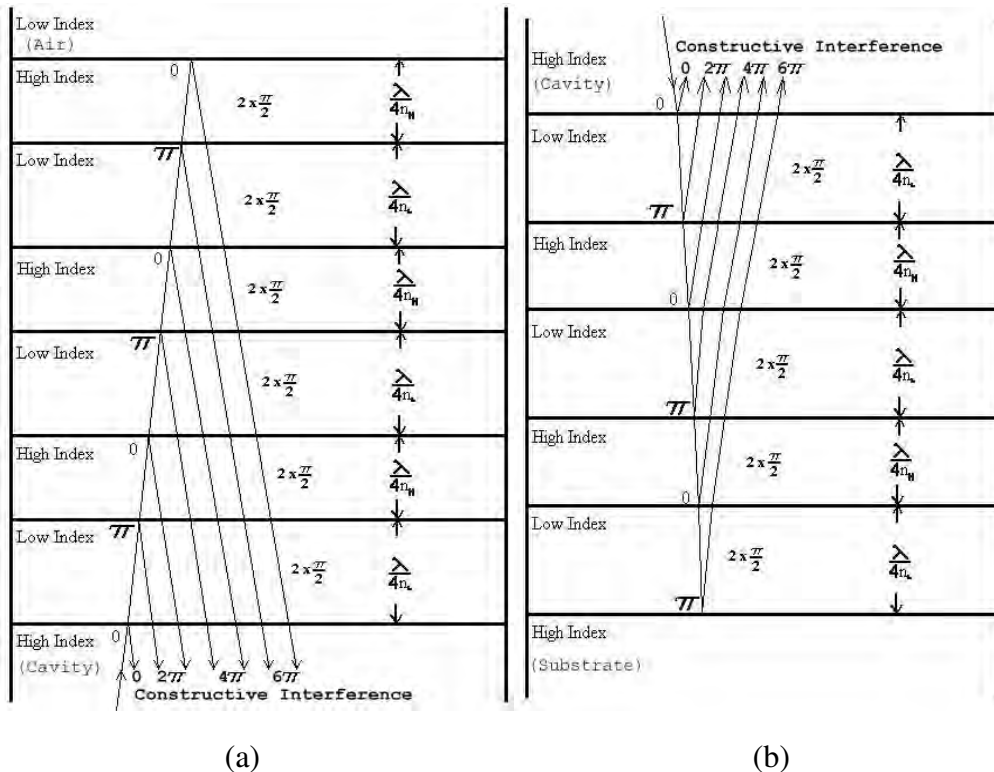
$$t_x = 1 + r_x \quad (2.2)$$

for TE polarization and

$$r_y = \frac{n_2 - n_1}{n_2 + n_1} \quad (2.3)$$

$$t_y = \frac{n_1}{n_2} (1 + r_y) \quad (2.4)$$

for TM polarization. Quick analysis of these equations confirms that there is a 180 degree phase shift in the reflection coefficient between the case of external reflection ( $n_1 < n_2$ ) and internal reflection ( $n_1 > n_2$ ).



(a) (b)  
Figure 2.3: Constructive interference in a (a) top DBR mirror and a (b) bottom DBR mirror.



Characteristic matrices can be created from the Fresnel Equations that relates the fields at two adjacent boundaries. MacLeod [14] has shown using Maxwell's equations that the field (E-Field, and H-field) at one boundary ( $E_{01}$ ,  $H_{01}$ ) is related to the field at the second boundary ( $E_{12}$ ,  $H_{12}$ ) by [14]

$$\begin{bmatrix} E_{01} \\ H_{01} \end{bmatrix} = \begin{bmatrix} \cos(\delta) & \frac{i \sin(\delta)}{\eta_1} \\ i \eta_1 \sin(\delta) & \cos(\delta) \end{bmatrix} \begin{bmatrix} E_{12} \\ H_{12} \end{bmatrix} \quad (2.5)$$

where  $E_{01}$  and  $H_{01}$  represent the field at the first boundary between the incident media and the dielectric layer, and  $E_{12}$  and  $H_{12}$  represent the field at the second boundary (between the dielectric layer and substrate or next material layer). The variable,  $\eta_1$ , is the optical admittance of the dielectric layer and is given by

$$\eta_1 = \frac{H_1}{E_1} = n_1 Y_0 \cos(\theta) \quad \text{for TE} \quad (2.6)$$

$$\eta_1 = \frac{H_1}{E_1} = \frac{n_1 Y_0}{\cos(\theta)} \quad \text{for TM} \quad (2.7)$$

where  $Y_0$ , the admittance of free space is

$$Y_0 = \sqrt{\frac{\mu_0}{\epsilon_0}} \approx \frac{1}{377} \quad \text{Siemens} \quad (2.8)$$

and  $\theta$  is the angle of incidence. The phase shift experienced by the light traveling through

the incident dielectric layer,  $\delta$  is given by

$$\delta = \frac{2\pi n_1 d_1 \cos(\theta)}{\lambda} \quad \text{radians} \quad (2.9)$$

where  $d_1$  is the thickness of the dielectric layer,  $\theta$  is the angle between the surface normal and the direction of propagation, and  $\lambda$  is the wavelength of light in a vacuum. By defining the input optical admittance of the dielectric layer structure as

$$Y = \frac{H_{01}}{E_{01}} \quad (2.10)$$

we can rewrite Equation (2.5) as

$$E_{01} \begin{bmatrix} 1 \\ Y \end{bmatrix} = \begin{bmatrix} \cos(\delta) & \frac{i \sin(\delta)}{\eta_1} \\ i \eta_1 \sin(\delta) & \cos(\delta) \end{bmatrix} \begin{bmatrix} 1 \\ \eta_2 \end{bmatrix} E_{12} \quad (2.11)$$

which gives

$$Y = \frac{\eta_2 \cos(\delta) + i \eta_1 \sin(\delta)}{\cos(\delta) + \frac{i \eta_2 \sin(\delta)}{\eta_1}} \quad (2.12)$$

To determine the reflectance or transmittance of a dielectric structure, it is useful to calculate a characteristic matrix that describes the optical admittance (Y). For a single interface, the characteristic matrix is defined as

$$\begin{bmatrix} B \\ C \end{bmatrix} = \begin{bmatrix} \cos(\delta) & \frac{i \sin(\delta)}{\eta_1} \\ i\eta_1 \sin(\delta) & \cos(\delta) \end{bmatrix} \begin{bmatrix} 1 \\ \eta_2 \end{bmatrix} \quad (2.13)$$

where it is easy to see that  $Y = C/B$ . Equation (2.13) can be expanded to determine the characteristic matrix of a stack of multiple dielectric layers and written as

$$\begin{bmatrix} B \\ C \end{bmatrix} = \left( \prod_{r=1}^q \begin{bmatrix} \cos(\delta_r) & \frac{i \sin(\delta_r)}{\eta_r} \\ i\eta_r \sin(\delta_r) & \cos(\delta_r) \end{bmatrix} \right) \begin{bmatrix} 1 \\ \eta_s \end{bmatrix} \quad (2.14)$$

where  $q$  is the number of layers,  $\delta_r$  is the phase shift in each layer,  $\eta_r$  is the optical admittance of each layer, and  $\eta_s$  is the optical admittance of the exit medium (substrate). Since the order of matrix multiplication is important, equation (2.14) can be expressed as

$$\begin{bmatrix} B \\ C \end{bmatrix} = [M_1][M_2] \dots [M_q] \begin{bmatrix} 1 \\ \eta_s \end{bmatrix} \quad (2.15)$$

where  $M_1$  is the characteristic matrix of the first layer,  $M_2$  is the characteristic matrix of the second layer and so on. Thus, the multiplication must start with the characteristic matrix of the first layer and continue in sequence to the bottom or last layer of the DBR stack. Once the BC matrix is determined, reflectance, transmittance and absorption can

be calculated using the Fresnel equations and  $Y = C/B$ . As long as  $\eta_o$ , the incident medium admittance, is real, the equations for reflectance, transmittance and absorption are given by

$$R = \left( \frac{\eta_o B - C}{\eta_o B + C} \right) \left( \frac{\eta_o B - C}{\eta_o B + C} \right)^* \quad (2.16)$$

$$T = \frac{4 \eta_o \operatorname{Re}(\eta_s)}{(\eta_o B + C)(\eta_o B + C)^*} \quad (2.17)$$

$$A = \frac{4 \eta_o \operatorname{Re}(B C^* - \eta_s)}{(\eta_o B + C)(\eta_o B + C)^*} \quad (2.18)$$

These three quantities are connected by the equation

$$1 = R + T + A \quad (2.19)$$

The calculated reflectance, transmittance and absorptance of a 29 period (58 layer) distributed Bragg reflector with GaAs/Al<sub>0.9</sub>Ga<sub>0.1</sub>As quarter wave layers is shown in Figure 2.4. At the design wavelength of 1300 nanometers, the reflectance is 99.99 percent. The reflectance of the DBR is highly wavelength dependent because the layer thicknesses are fixed to an optical length equal to a quarter of the design wavelength. Additionally, the material indices of refraction vary as a function of wavelength, so the optical length of the layers varies with wavelength. The calculated index of refraction of GaAs and AlGaAs versus wavelength is shown in Figure 2.5. The values in Figure 2.5 were calculated by a Matlab routine using equations in a paper by Guden and Piprek [15]. Other factors affecting the reflectance of DBRs include the

number of periods (1/4 wave layer pairs) in the DBR (Figure 2.6), and the index of refraction contrast between the two different layers (Figure 2.7). The top DBR is

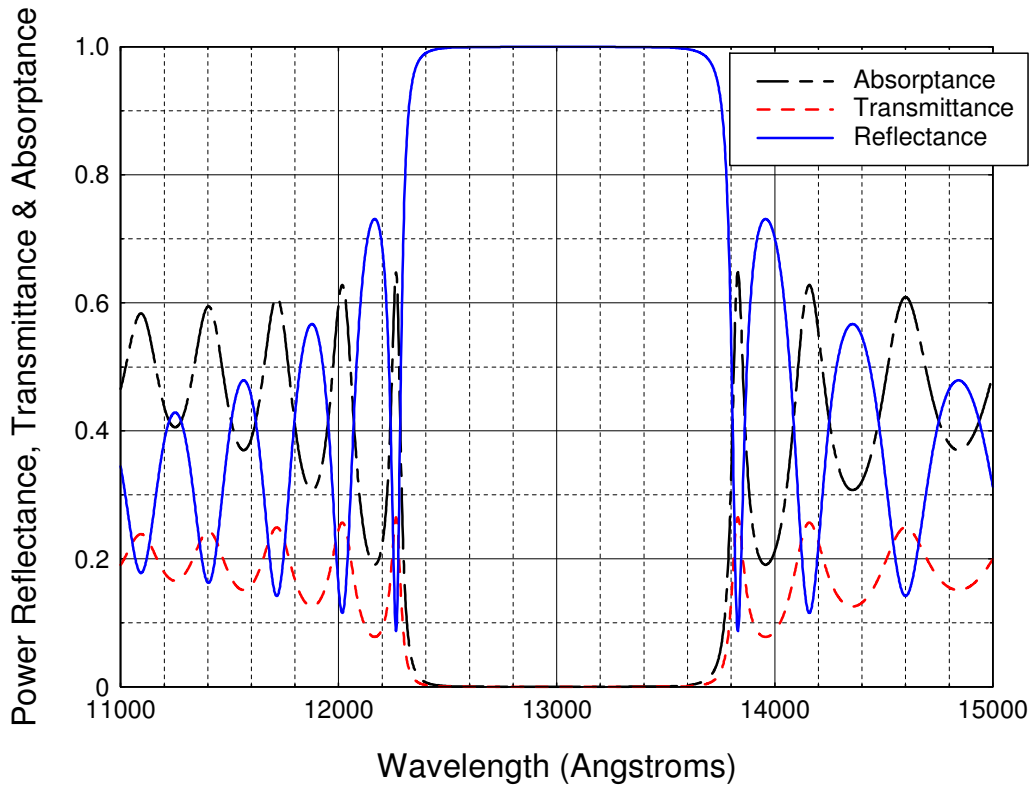


Figure 2.4: Calculated power reflectance, transmittance, and absorptance of a DBR reflector with 29 periods of GaAs and  $\text{Al}_{0.9}\text{Ga}_{0.1}\text{As}$

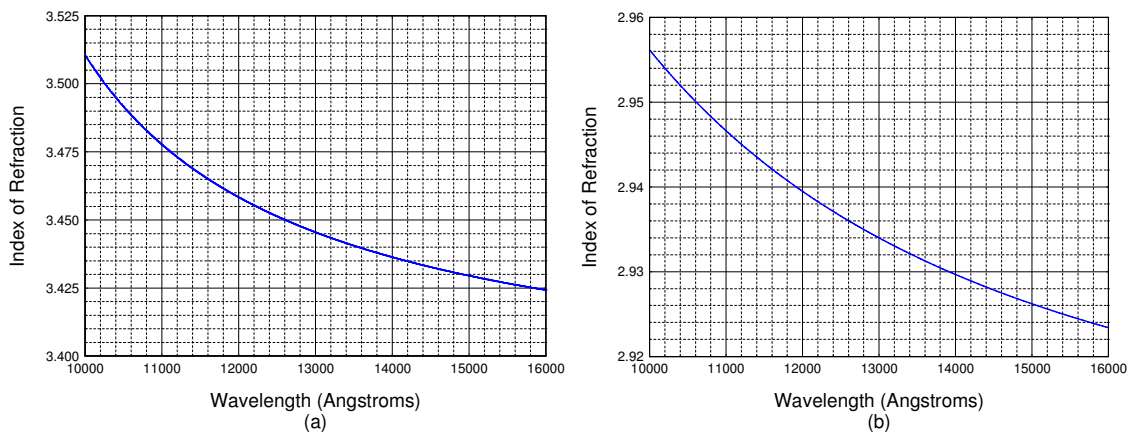


Figure 2.5: Indices of refraction of GaAs (a) and  $\text{Al}_{0.9}\text{Ga}_{0.1}\text{As}$  (b) versus wavelength

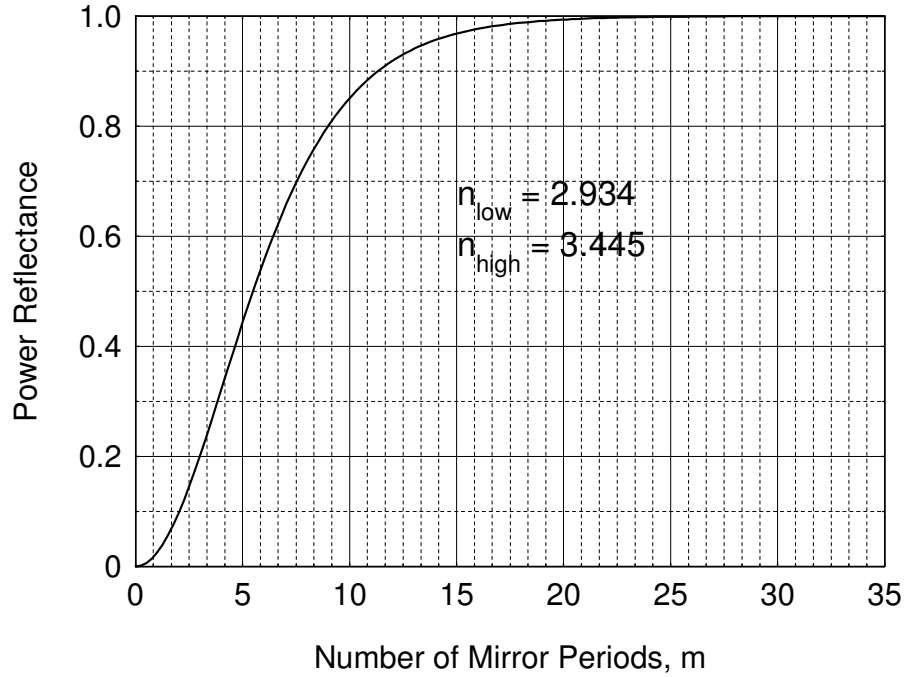


Figure 2.6: Power reflectance at the design wavelength of a GaAs/Al<sub>0.9</sub>Ga<sub>0.1</sub>As DBR versus the number of periods in the DBR.

typically the output mirror of the laser and therefore has a fewer number of DBR periods and a lower reflectance. The desired reflectance for both DBRs can be achieved by selecting the appropriate number of periods and the appropriate materials using the simple equation [16]:

$$R = \left( \frac{1 - (n_L / n_H)^{2m}}{1 + (n_L / n_H)^{2m}} \right)^2 \quad (2.20)$$

where  $n_L$  and  $n_H$  are the refractive indices of the low and high DBR layers respectively and  $m$  is the number of DBR periods. However, there is a tradeoff to the number of periods and the materials because of the electrical properties of DBRs. The boundaries

and subsequent abrupt changes in material band gaps create electrical resistance in DBR mirrors. To reduce the electrical resistance, the boundaries in DBRs can be graded to produce a more gradual change in the material. This greatly improves the conductivity, but reduces the reflectance slightly. Doping the DBRs can also improve conductivity, but the dopants cause optical losses increasing absorptance. These are the main reasons for choosing an intra-cavity contacted VCSEL. In an intra-cavity contacted device, the DBRs can be undoped, ungraded, and therefore more reflective with little optical loss.

Another way to increase the reflectance and decrease the electrical resistance of the DBRs is to increase the refractive index contrast between the two materials to reduce the number of DBR periods required to achieve the desired reflectance. Increasing the difference between the low and high layer refractive index increases both the peak reflectance and the bandwidth of the high reflectance value (stop band) of the DBR. This can be seen in Figure 2.7. However, increasing the index contrast does not have a large effect on the abruptness of the stop band.

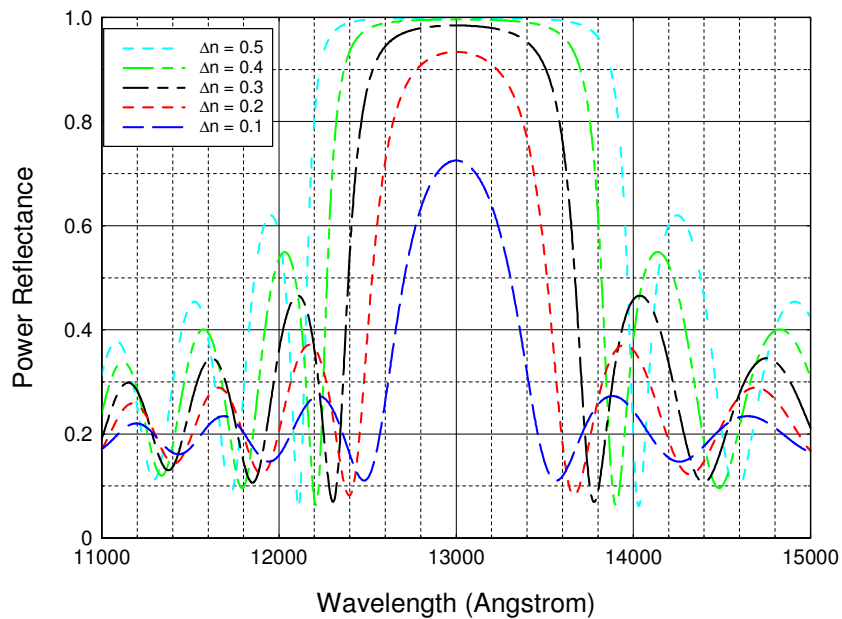


Figure 2.7: Power reflectance versus wavelength for refractive index differences between the high and low index layers of a DBR (20 periods and  $n_L = 2.5$ )

The high reflectance of DBRs only occurs over a relatively small band of wavelengths centered about the design wavelength. As the number of DBR periods increases, not only does the peak reflectance increase, but the band of high reflectance also becomes more abrupt and narrower. Figure 2.8 shows the reflectance of DBRs with varying number of periods versus wavelength. This characteristic of DBRs is one factor that limits the possible laser wavelengths or longitudinal modes of a VCSEL.

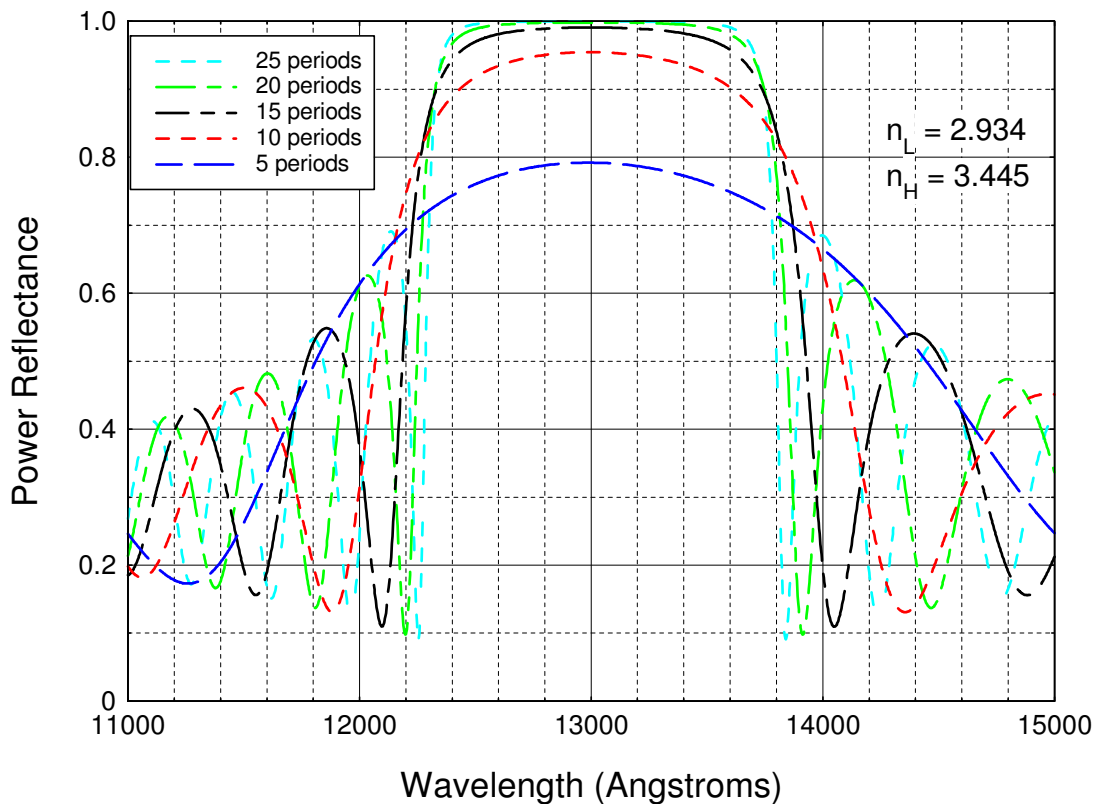


Figure 2.8: Calculated power reflectance versus wavelength of GaAs/Al<sub>0.9</sub>Ga<sub>0.1</sub>As DBRs with different numbers of periods



### 2.3 Optical Characteristics of Microcavities

Another factor limiting the number of longitudinal modes supported by VCSELs is the extremely small cavity length in relation to other lasers. The optical cavity is a fundamental part of a laser and in its simplest form consists of a cavity between two planar mirrors. While most lasers have cavity lengths on the order of hundreds or even thousands of wavelengths, VCSELs and other microcavity devices typically have cavity lengths of two to six wavelengths of the output light. This results in optical properties similar to Fabry-Perot (FB) etalons and resonance that supports few if not only one longitudinal mode. Thus, I can begin to describe the characteristics of a microcavity by describing the optical properties of a FP etalon. Given a FP etalon consisting of two mirrors with a reflectance of  $R_1$  and  $R_2$  separated by a distance  $L_c$ , the transmission spectrum will have peaks that correspond to the resonant wavelengths of the etalon cavity. It can be shown that the reflectance,  $R$ , and transmission,  $T$ , can be described by [12]

$$R = \frac{4\sqrt{R_1R_2}}{\left(1-\sqrt{R_1R_2}\right)^2} \sin^2\left(\frac{\delta}{2}\right)}{1 + \frac{4\sqrt{R_1R_2}}{\left(1-\sqrt{R_1R_2}\right)^2} \sin^2\left(\frac{\delta}{2}\right)} \quad (2.21)$$

$$T = \frac{1}{1 + \frac{4\sqrt{R_1R_2}}{\left(1-\sqrt{R_1R_2}\right)^2} \sin^2\left(\frac{\delta}{2}\right)} \quad (2.22)$$

Both equations assume there is no loss in the cavity. The variable,  $\delta$ , is the round trip phase shift of light through the cavity and is described by [12]

$$\frac{\delta}{2} = \left( \frac{2\pi n L_c}{\lambda} \right) \cos(\theta_i) \quad (2.23)$$

where the wavelength of interest is  $\lambda$ ,  $n$  is the refractive index of the cavity material,  $\theta_i$  is the angle of incidence, and  $L_c$  is the cavity length.

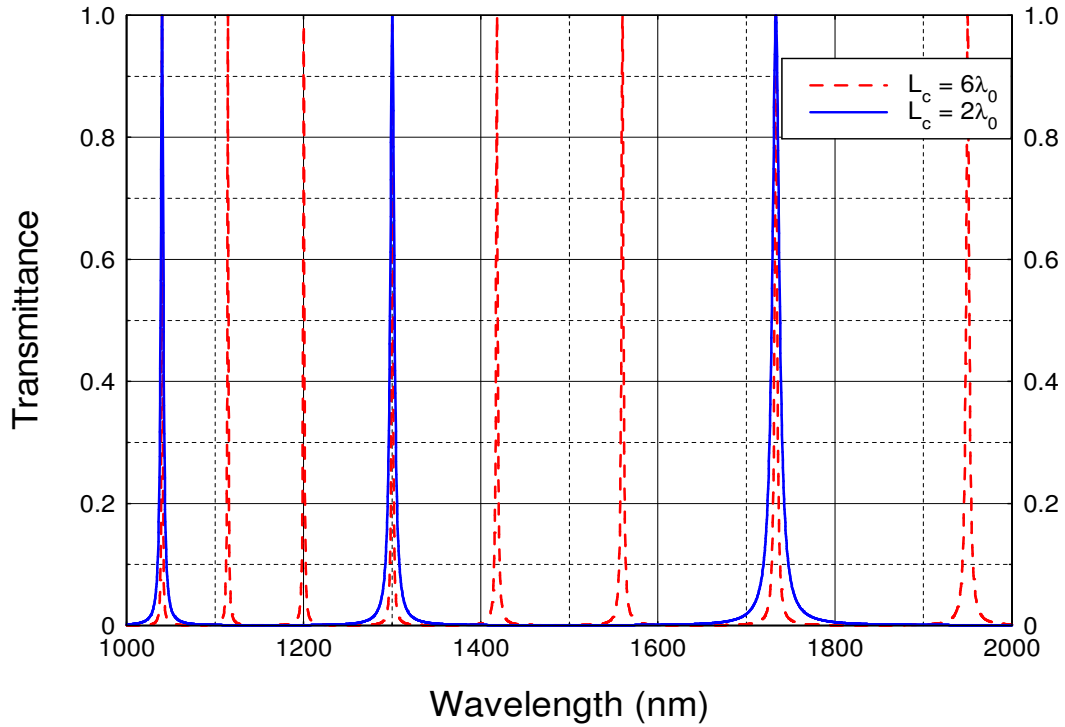


Figure 2.9: Power transmission of  $2\lambda$  and  $6\lambda$  ( $L_c$ ) resonant cavities versus wavelength ( $\lambda_{\text{design}} = 1300$  nm,  $R_1 = R_2 = 0.95$ )

The reflectance of the mirrors has significant effect on the transmission of the cavity as is shown in Figure 2.10. Increasing the reflectance narrows the peaks of the transmission spectrum of cavity. The property governed by mirror reflectance and cavity

length is called the cavity finesse, and is defined as the ratio of transmittance peak separation to the transmittance full-width half-maximum (FWHM) or by [16]

$$F = \frac{\text{Peak separation}}{\text{Peak width}} = \frac{\pi}{1 - \sqrt{R_1 R_2}} \quad (2.24)$$

As the value of  $R_1$  and  $R_2$  approach 1, the finesse gets very large. VCSELs have very large finesse because the peak separation is large (due to the small cavity length) and the DBR mirrors have very high values of reflectance. However, the value of reflectance is only high over a limited range of wavelengths called the stop band. Figure 2.11 shows how in a typical VCSEL the DBR stop band and the cavity transmittance overlap to

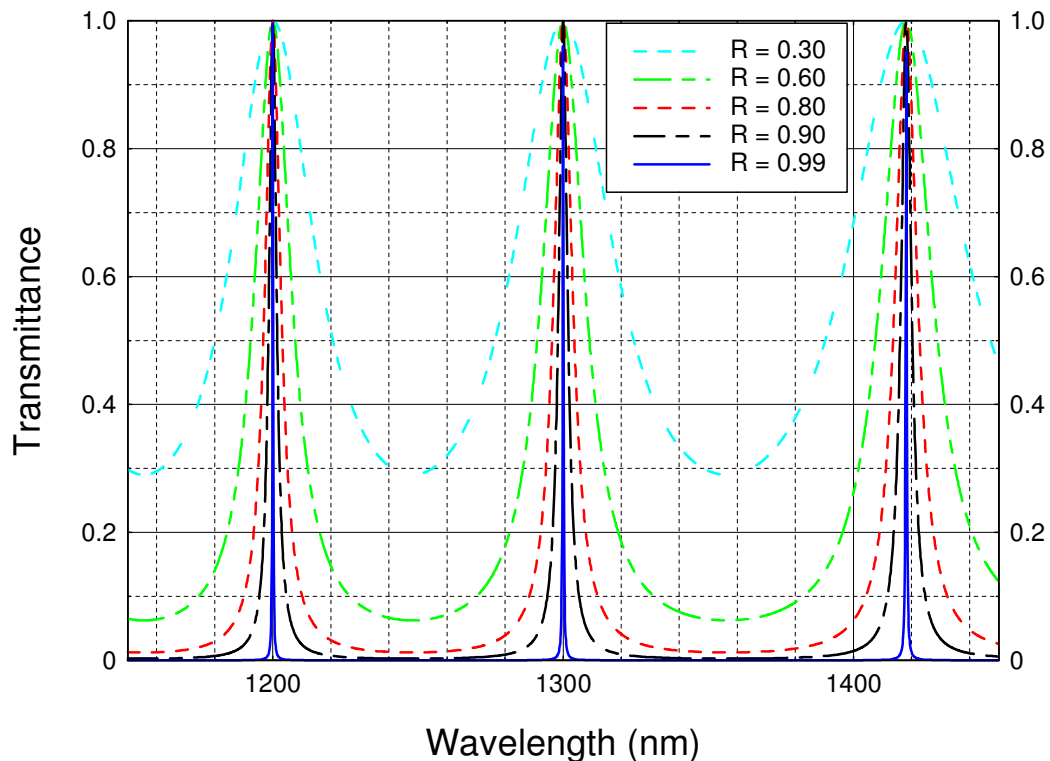


Figure 2.10: Power transmission of a  $6\lambda$  ( $L_c$ ) resonant cavity versus wavelength for mirrors with various values of reflectance ( $R_1 = R_2 = R$ )

support only one of the peaks and thus only one longitudinal cavity mode. Combining the spectral characteristics of the DBR mirrors and the microcavity creates results in the characteristics shown in Figure 2.12, for an RCLED and Figure 2.13 for a VCSEL. The RCLED has a much broader Fabry-Perot dip in the reflectance of the cavity due to the relatively low reflectance of the top mirror ( $R \approx 0.3$ ). The Absorptance of the RCLED is negligible because most of the optical loss is in the interfaces of the DBR layers and this model doesn't take into account impurities in the material or dopants.

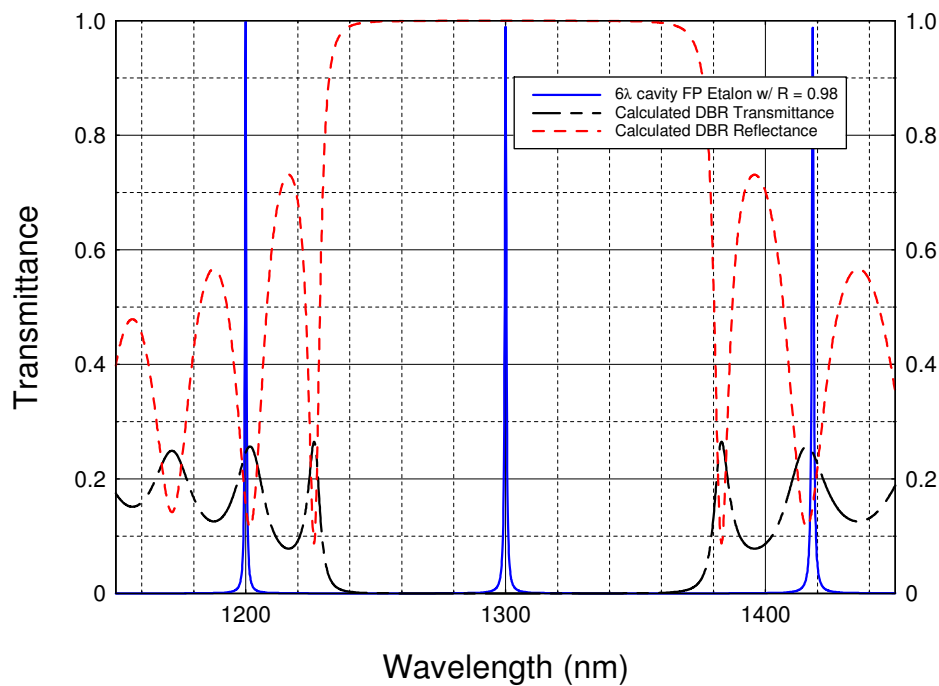


Figure 2.11: Power transmission of a  $6\lambda$  ( $L_c$ ) resonant cavity and the stop band of a typical microcavity DBR versus wavelength

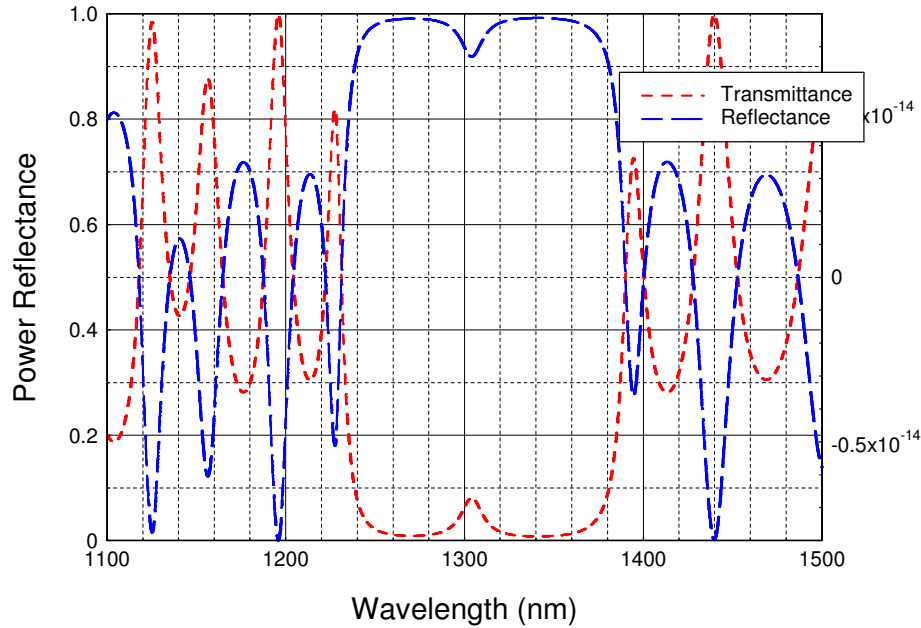


Figure 2.12: Calculated reflectance and transmittance versus wavelength of  $6\lambda$  ( $L_c$ ) RCLED with a 12 period DBR ( $\lambda_{\text{design}} = 1300$  nm)

The VCSEL has many more boundaries and a significant amount of absorption seen in Figure 2.13. In addition to the higher absorption, the Fabry-Perot dip is much sharper because the reflectance of the cavity mirrors is much higher. At the wavelength that corresponds to this dip in the reflectance of the VCSEL structure, an electric field forms from the standing wave pattern in the cavity. This electric field distribution must be taken into account when selecting the locations of quantum dot layers within the cavity. It is most efficient to place quantum dot layers at the anti-nodes (peaks) in the electric field intensity and will maximize the amount of gain that can be achieved from these layers. Figure 2.14 shows the electric field distribution and the resonant wavelength (FP wavelength) of the cavity and the corresponding locations of quantum dot layers.

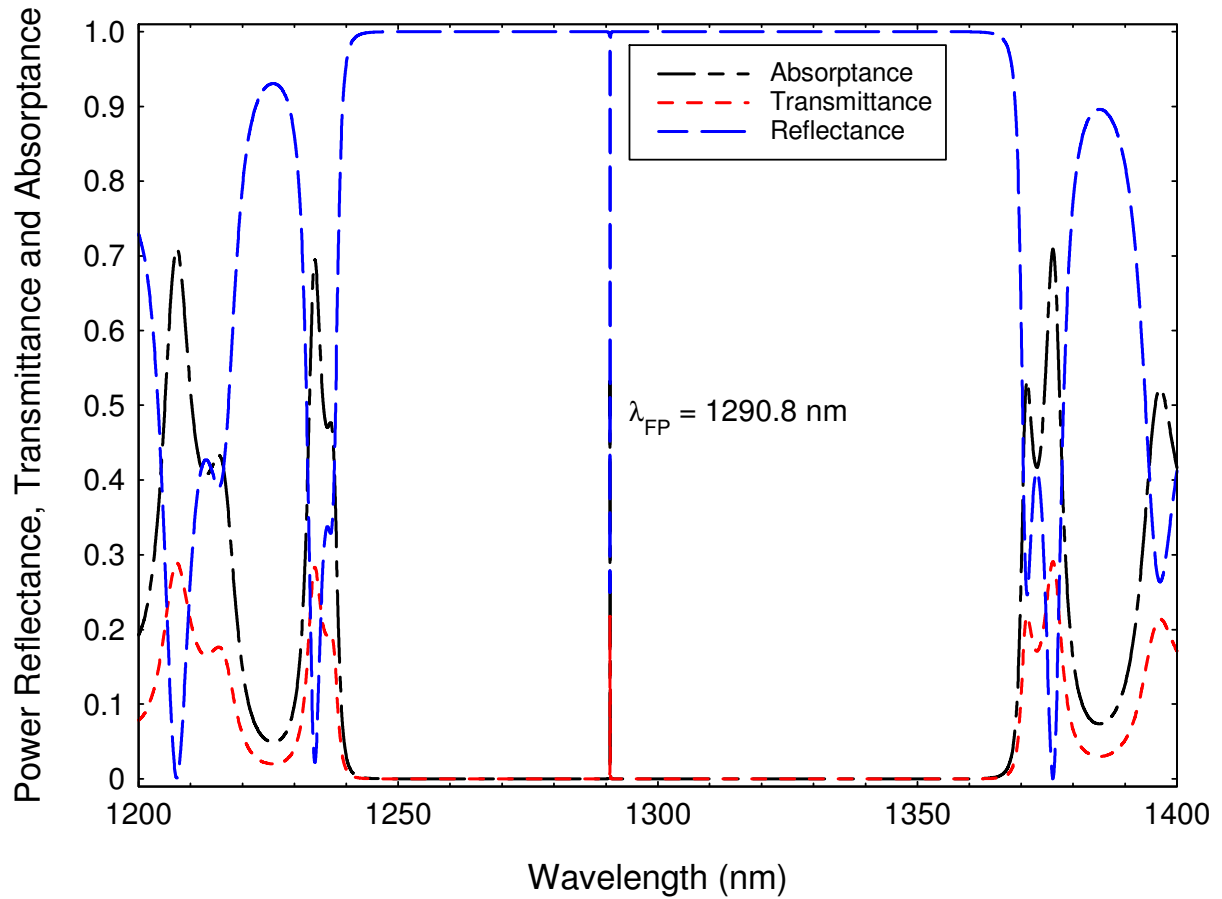


Figure 2.13: Modeled reflectance, transmittance and absorption versus wavelength of  $6\lambda$  ( $L_c$ ) through-DBR VCSEL with a 27 period top DBR, a 33 period bottom DBR

Aligning the quantum dot gain layers with the peaks in the standing wave electric field intensity maximizes the gain of the device by promoting stimulated emission of the quantum dots and discouraging absorption of photons and other loss mechanisms in the cavity. As can be seen in Figure 2.14, the electric field extends beyond the actual cavity and penetrates into each DBR. This phenomenon increases the effective length of the optical microcavity. The effective length of the cavity is then the sum of the physical

cavity length and the penetration depths of each DBR mirror. The penetration depth of a DBR mirror ( $L_{pen}$ ) can be described by [16]

$$L_{pen} = \frac{1}{2} \cdot m_{eff} (L_1 + L_2) \quad (2.25)$$

Where  $m_{eff}$  is the effective number of DBR layered pairs (high and low index) seen by the wave electric field or when there are a large number of layered pairs described by

$$m_{eff} \approx \frac{1}{2} \frac{n_1 + n_2}{n_1 - n_2} \quad (2.24)$$

The DBR penetration depth is illustrated in Figure 2.15.

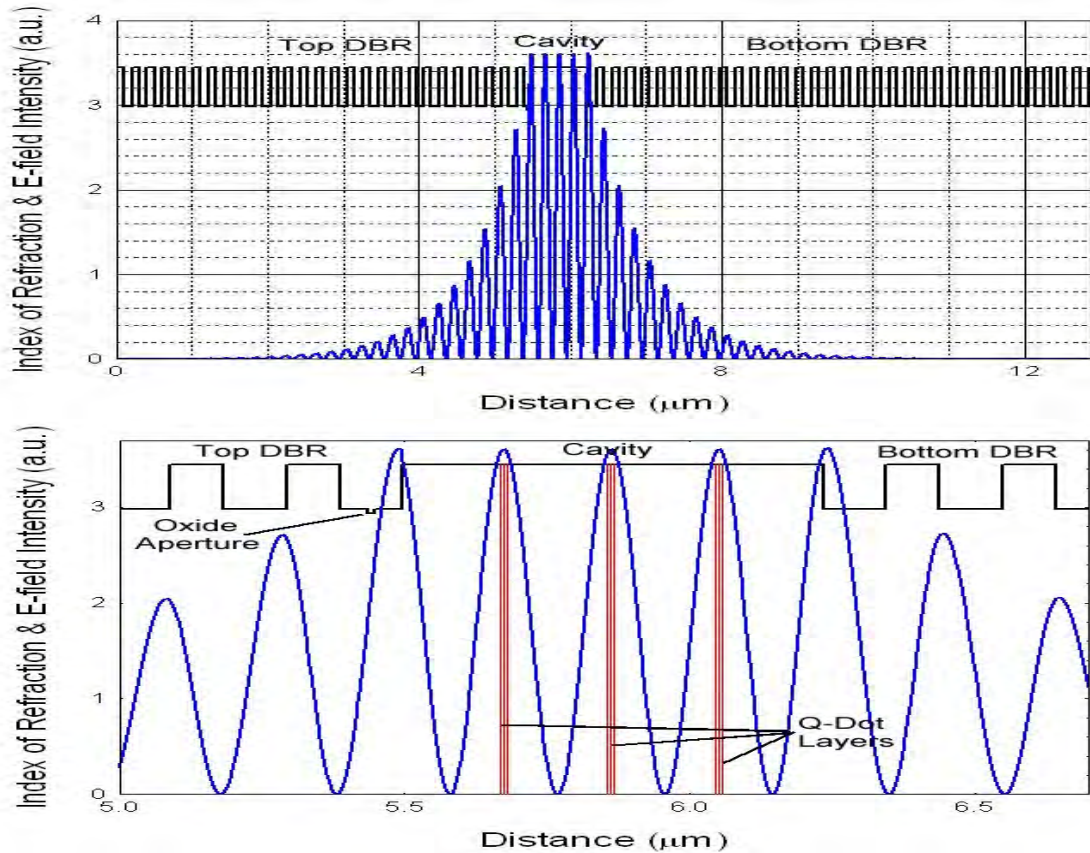


Figure 2.14: Electric field intensity and the refractive index profile versus distance in the  $2\lambda$  microcavity VCSEL structure calculated using Matlab routines [Ochoa]

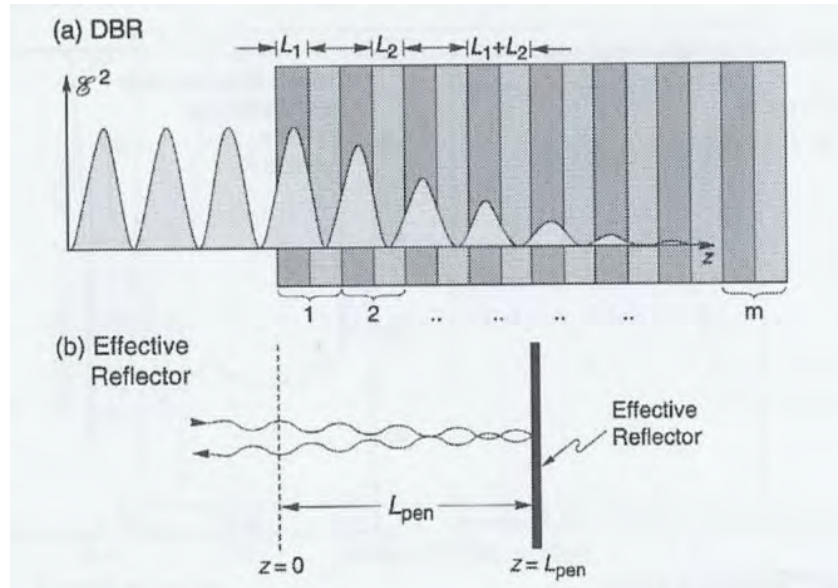


Figure 2.15: Illustration of the DBR penetration depth. (a) DBR consisting of two materials of thickness  $L_1$  and  $L_2$ . (b) Ideal (metallic) reflector displaced by the penetration depth [16]

## 2.4 Quantum Dots

**2.4.1 Quantum Dot Active Regions.** The quantum dot laser was proposed by R.Dingle and C.H. Henry(1976) and later Y. Arakawa and H. Sakaki(1982) made further developments in QD lasers with the intent to lower the threshold current and create a laser insensitive to temperature [17]. Quantum dot energy density of states (DOS) is represented by a set of delta functions. The threshold current density is not dependent on temperature because there is an absence of higher energy states available to fill via thermal excitation [17]. This early work sought to modify quantum well DOS to be more like QD DOS with the application of a magnetic field. Further work by Goldstein et al(1985) formed InAs clusters in a GaAs matrix [17] to create an artificial QD array inside the active region of a laser. The most successful methods of achieving QD active regions for 1.3  $\mu\text{m}$  wavelength QD lasers is the spontaneous formation of QDs using strained layer epitaxy.



One very popular method of epitaxial growth of microcavity devices is molecular beam epitaxy in which solid elements are vaporized and combined in a vacuum chamber to be deposited on a semiconductor wafer at a specific rate dependant on temperature (source and wafer) and pressure. The three primary modes of epitaxial growth are 2D layer growth, 3D island growth or a combination of both. These types of growth depend on the chemical potentials of the first few deposited layers [18]. When the adatom to adatom interaction is stronger than the adatom to surface interaction, 3D island growth occurs. When 3D island growth occurs exclusively the growth mode is called, Volmer-Weber growth [18]. When the adatom to surface interaction is stronger, 2D layer growth takes place exclusively and the growth mode is referred to as Frank-van der Merwe growth [18]. Lastly, when growth is initially 2D, but at some critical mono-layer thickness the adatom to adatom interaction becomes greater than that between the adatom to surface, and growth switches to 3D island growth type. This mode is referred to as Stranski-Krastanov (SK) growth mode [18]. Using this growth mode, quantum dots can be grown into the active regions of microcavity devices and by varying the growth conditions (growth rate, growth temperature and ratios of elements), the emission wavelength of the quantum dots can be set to anywhere from 1  $\mu\text{m}$  to 1.7  $\mu\text{m}$ . Several methods of tuning InAs QDs have been investigated to achieve specific output wavelengths. One method is to embed the QDs in a layer of  $\text{In}_x\text{Ga}_{1-x}\text{As}$ . This will red shift the output of the QDs by increasing the dot height [19] and requires some trial and error to find the appropriate concentrations of Indium, Gallium and Arsenide for the capping layer. The higher the indium concentration the more the output of the QDs is shifted to longer wavelengths [19]. Varying the material composition of the capping layer can have a profound effect on the electronic structure of QDs as capping InAs QDs in InP has also been studied to achieve emission wavelengths above 1.6 $\mu\text{m}$  [20]. Rapid thermal annealing has also been used to adjust the output of QD active regions [21]. A

blue shift and spectral narrowing in QD emissions has been demonstrated by annealing and in greater effects by increasing the temperature of the annealing process [21].

Another method is to simply grow larger dots by slowing the growth rate down and has the advantage of using less indium [19]. Figure 2.16 shows cross sectional views of the three primary modes of thin film growth as the number of layers increases.

As was discussed in section 2.3, the quantum dots are grown such that they are aligned with anti-nodes in the electric field intensity that results from the standing wave in the microcavity. In addition to this, the QDs are typically vertically stacked to improve the effective gain of the active region by avoiding gain saturation that occurs due to the finite number of states in the quantum dot array [19]. Capping the QDs with a layer of InGaAs creates a potential well or quantum well and is referred to as Dot in a Well or DWELL. This potential well helps collect carriers and decreases nonradiative recombination in the active region.

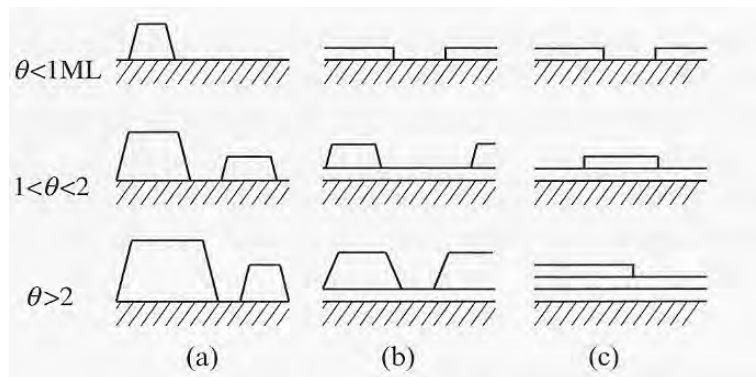


Figure 2.16: Cut away views of three different modes of epitaxial growth as a function of the coverage,  $\theta$  in monolayers (ML): (a) island or Volmer-Weber growth; (b) layer-plus-island, or Stranski-Krastanov growth; (c) layer-by-layer, or Frank-van der Merwe growth [18]

2.4.2 *Quantum Dot Density of States.* Using Schrodinger's wave equation and the infinitely deep quantum well model, we can model the density of allowed electron energy states in bulk semiconductor material, a semiconductor quantum well, a quantum wire and quantum dots. The density of states for bulk semiconductor material or electrons that are not confined in three dimensional space is [17]:

$$\rho^{3D}(E) = \frac{8\pi \sqrt{2}}{h^3} m^{*3/2} \cdot E^{1/2} \quad (2.25)$$

where  $m^*$  is the effective mass of electrons,  $h$  is Planck's Constant, and  $E$  is the difference in electron energy and the conduction band energy ( $E - E_c$ ) with  $E > E_c$ . When the thickness of a semiconductor active layer is comparable to the DeBroglie wavelength, quantum size effects occur and a potential energy well is created that confines particles to a 2D plane. This is referred to as a quantum well, and the density of states at any particular energy,  $E$ , is the sum of all bands below that energy and given by [17]

$$\rho^{2D}(E) = \sum_{i=1}^n \frac{4\pi m^*}{h^2} \cdot \Theta(E - E_i) \quad (2.26)$$

where  $\Theta$  is the unit step function, and  $E_i$  are the allowable energy states in the quantum well. Further confining carriers to all but one dimension, as is the case in quantum wires,

leads to a DOS that is proportional to  $E^{-1/2}$  at discrete energy levels. The density of states for an active region with an  $n$  by  $m$  array of quantum wires is given by [17]

$$\rho^{1D}(E) = \sum_n \sum_m \sqrt{\frac{2\pi m^*}{h^2}} \cdot \frac{1}{\sqrt{E - E_{n,m}}} \cdot \Theta(E - E_{n,m}) \quad (2.27)$$

When the carriers are confined in all three dimensions of space as with a quantum dot, the DOS becomes a delta function at an energy level determined mainly by the physical dimensions and shape of the quantum dot. The equation for the density of states of an array of quantum dots is given by [17]

$$\rho^{0D}(E) = \sum_n \sum_m \sum_l 2 \cdot \delta(E - E_{n,m,l}) \quad (2.28)$$

where  $\delta(E - E_{n,m,l})$  is the delta-function of a specific dot in the array. The density of states for bulk material, quantum wells, wires and dots is summarized in Figure 2.17. Ideally the density of states for a quantum dot is a single delta function. Realistically, there is actually some dimensionality to quantum dots that causes some degree of variance from an ideal delta function and multiple allowed energy states can exist. Furthermore, for an ensemble of QDs that have some degree of variability in size and shape, the DOS is inhomogenously broadened. The variability in dot size broadens the output spectrum of a quantum dot active region. Differences in the shape of the individual quantum dots also cause differences in allowed energy states and therefore broaden the output spectrum. Thus the width of the luminescence of the quantum dot active region is an indication of the variability in quantum dot size and shape [22].

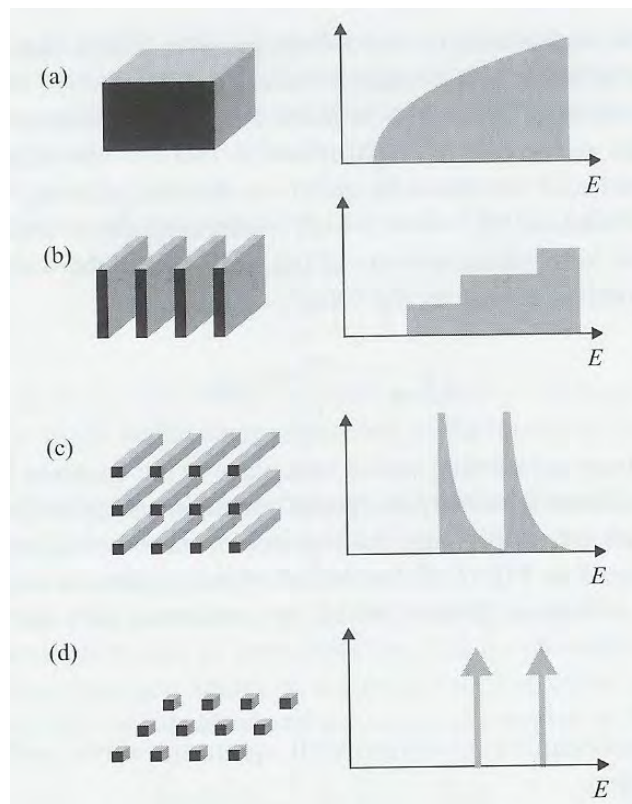


Figure 2.17: Active region of diode lasers representing a layer of bulk semiconductor (a), several quantum wells (b), an array of quantum wires (c), and an array of quantum dots (d) and the corresponding density of states [17]

*2.4.3 Quantum Dot Spectral Characteristics.* In addition to the size and shape of a quantum dot, the strain distribution of individual dots can affect the electronic structure (allowed energy states) of a quantum dot active region. QD electronic structure starts with the composition of the dot material, but then both the 3D confinement and the material strain restrict the allowed energy states to ideally create only one energy transition that is higher than that of the material bandgap. Figure 2.18 shows a diagram that is used to engineer specific bandgap energies by mixing the composition of

semiconductor material systems. The differences in lattice constants are also important in selecting materials for the formation of quantum dots as the lattice mismatch is essential to the formation of the islands. The electronic levels for an InAs pyramidal QD with a base size of 12 nm capped with GaAs with a 1.7 mono-layer (ML) wetting layer of GaAs have been calculated by solving the three dimensional effective mass single particle Schrodinger equation and are shown in Figure 2.19 [23].

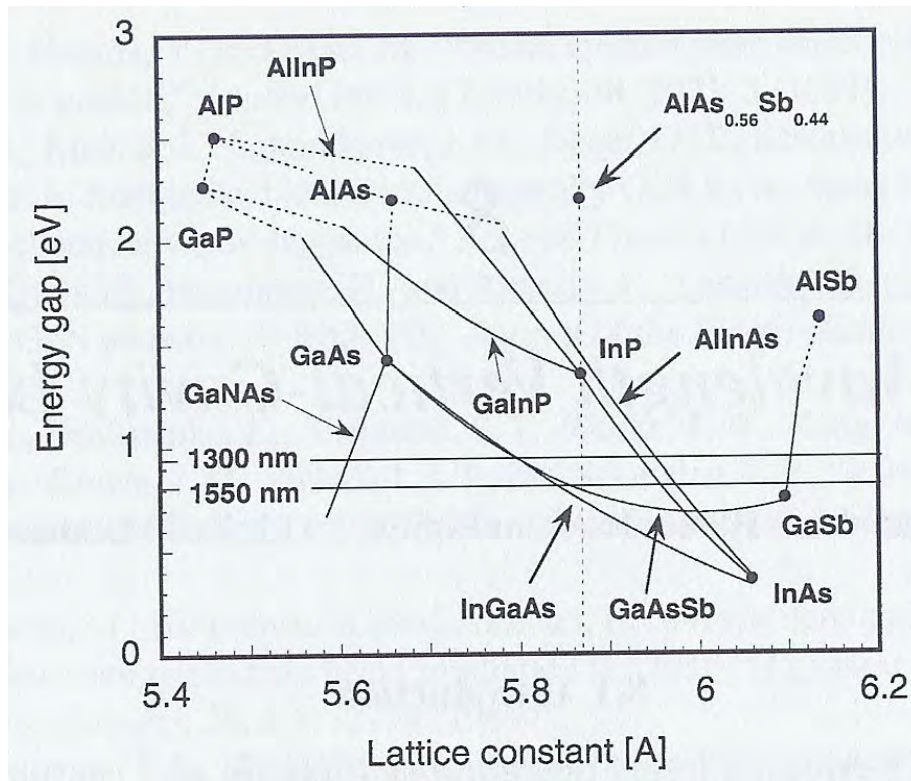


Figure 2.18: Bandgap energies and lattice constants of III-V material systems for various material composition [16]

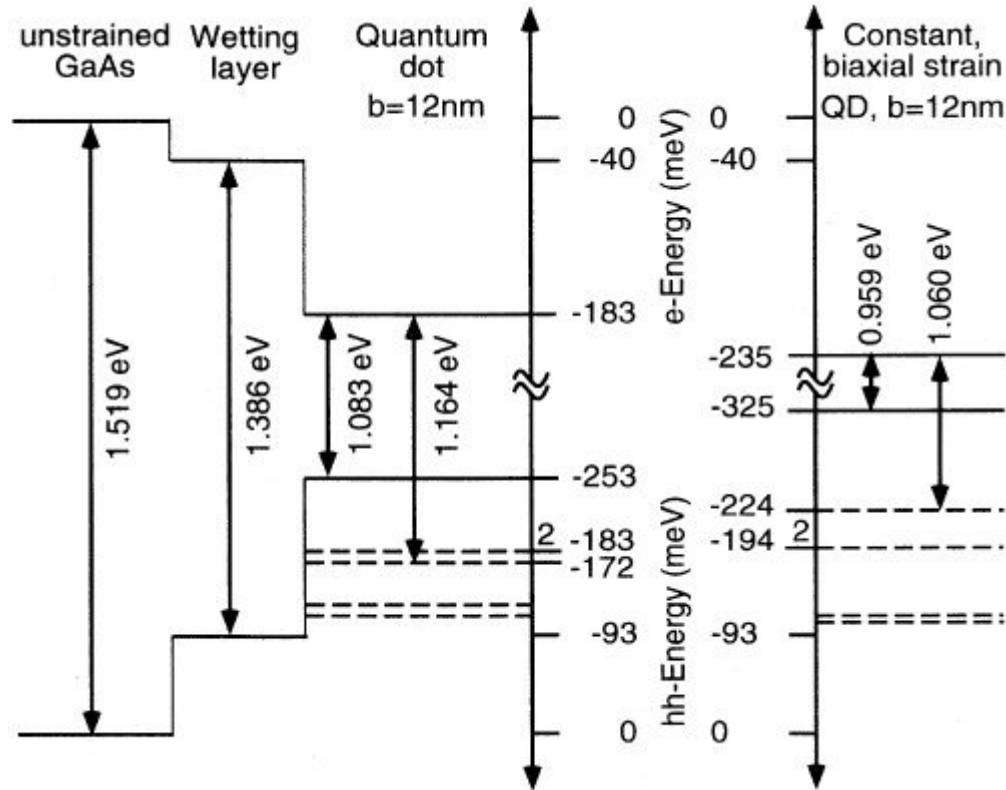


Figure 2.19: Calculated electronic structure of an InAs pyramidal quantum dot with a base size of 12 nm with a 1.7 ML wetting layer and capped with GaAs unstrained on the left, and GaAs with a uniform biaxial strain on the right [23]

Pyramidal QD's with base sizes in the range of 6 to 20 nm only have one allowed electron energy level. Below about 6 nm base width, no electron energy levels are allowed, and the heavy-hole energy levels merge with the WL energy level. The variation of these energy levels with varying QD size has been calculated [23] by solving the effective mass single particle Schrodinger equation and is shown in Figure 2.20 for various sized pyramidal dots. Over a limited range of sizes the transition energy between the electron QD ground state and the hole ground state is generally linear. Thus, it's typical that the gain curve of the QD active region takes on the Gaussian distribution of the sizes of QD ensemble in the active region. The electroluminescence (EL) of QD devices will resemble a Gaussian distribution as well, including the EL of the higher order transitions and the wetting layer. Figure 2.21 shows a plot of the EL of a QD active

region showing peaks for the ground state, excited state, and wetting layer transitions for quantum dots with a base size of 6 to 16 nm. The height of a QD has a greater effect on setting the ground state emission wavelength, while lateral size has greater importance in setting the energy difference between the ground state and first excited radiative transition [24]. Initially the EL is dominated by the electron ground state to hole ground state transition, but as carriers are increased and excited energy bands fill, additional peaks emerge.

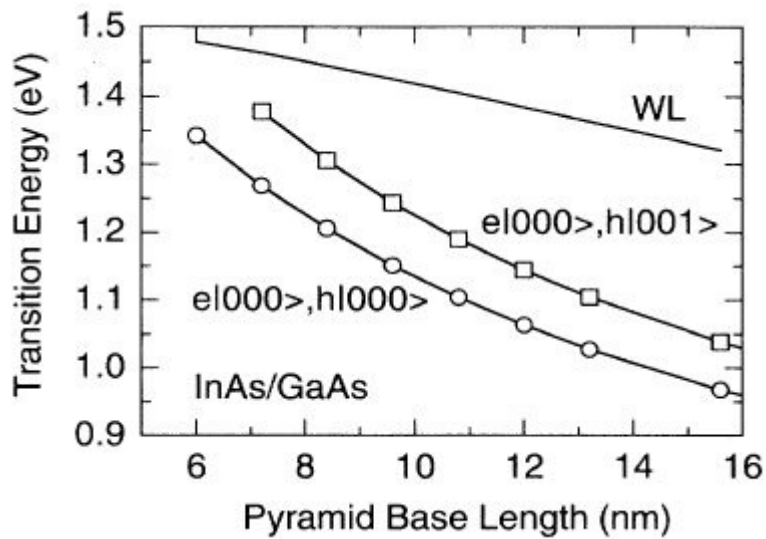


Figure 2.20: Theoretical transition energy versus quantum dots size for electron ground state to hole states with the wetting layer transition [23]



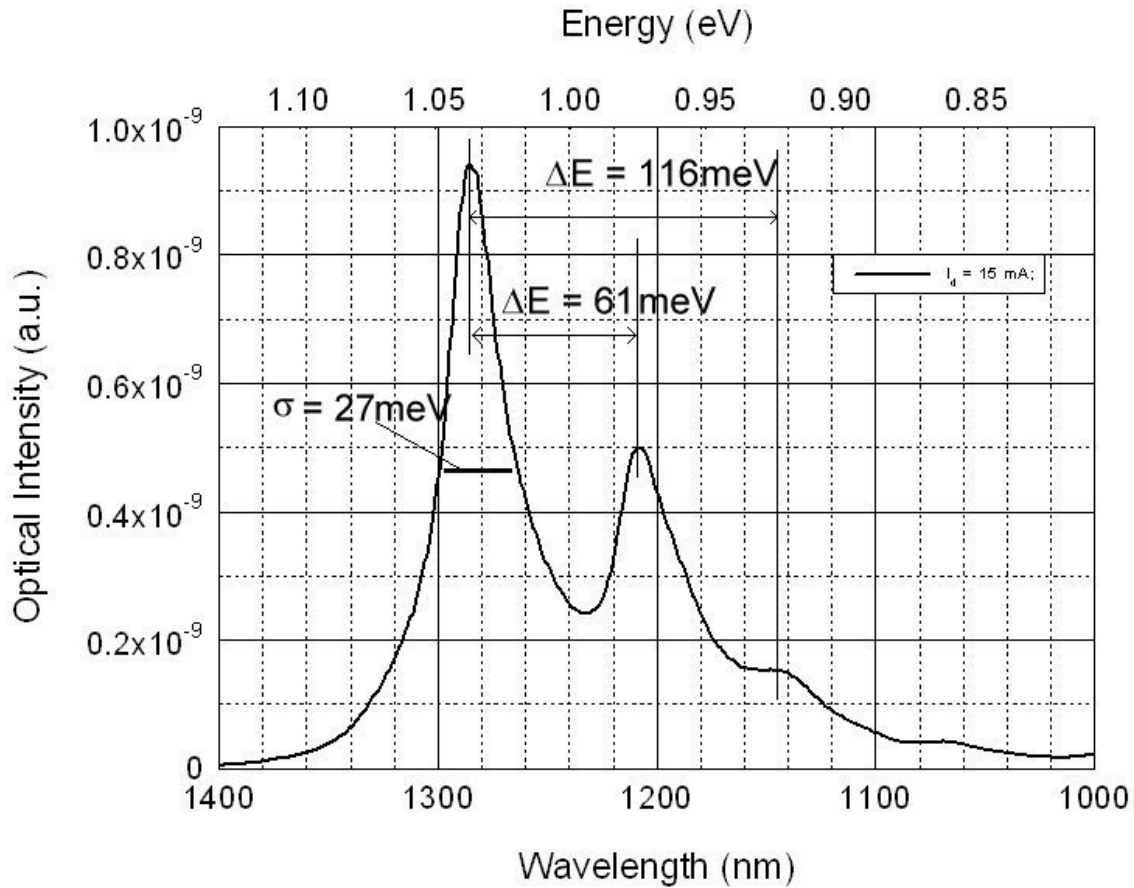


Figure 2.21: EL spectrum (at room temperature) of a InAs/InGaAs QD active Region with energy level separation ( $\Delta E$ ) and FWHM ( $\sigma$ ) shown

The presence of multiple hole energy levels can also lead to thermal broadening in an ensemble of quantum dots reducing the efficiency of the device. The WL transition also increases as increased temperature and current fills the available QD energy levels reducing efficiency further. Analyzing the energy levels of these peaks and how many peaks are present and the separation between these peaks enables one to determine the size and uniformity of the quantum dots in an active region [25]. A large energy separation between the ground state and first excited energy state is desired, as is a narrow FWHM of the ground state transition to maximize the gain and efficiency of the device.

## 2.5 Quantum Dot Laser Characterization and Temperature Effects

Semiconductor lasers can generally be characterized electrically, spatially, spectrally, optically and dynamically. Electrical characteristics include or involve measuring the optical power and drive current over a range of applied voltages. The data is typically presented on an LIV curve with drive current on the horizontal axis, and voltage and optical power are plotted on separate vertical axes. An example of an LIV curve is shown in Figure 2.22. Analyzing the data on an LIV curve can involve derivative analysis and be used to determine the threshold current of a laser. The threshold current is the point at which the gain in the laser cavity is equal to the losses. Threshold current is also the point where the rate of change in output power per change in input current is maximum, and marks when stimulated emission becomes greater than spontaneous emission. LIV data can be measured and analyzed for a range of operating temperatures to further characterize the laser and study the effects of temperature on laser performance. The characteristic temperature ( $T_0$ ) empirically describes how a laser's threshold current changes with changes in temperature and is defined in the following equation [26]

$$T_0(T) = \frac{T - T_{ref}}{\ln \left( \frac{I_{th}(T)}{I_{th}(T_{ref})} \right)} \quad (2.29)$$

where  $T$  and  $T_{ref}$  are two different temperatures typically closely spaced where the threshold current ( $I_{th}$ ) has been experimentally determined. A large value of  $T_0$  is desired since this would result in a constant threshold current over a range of temperatures. Theoretically, if all the carriers were to be injected into quantum dots, the characteristic temperature of a quantum dot laser would be infinitely large. However, non-ideal effects

on the gain curve and shifts in the cavity resonance lead to changes in the threshold current over temperature. There have been a large number of studies on the effect of temperature on the threshold current of QD lasers looking for ways to stabilize the laser characteristics over a greater temperature range [27, 28, 29].

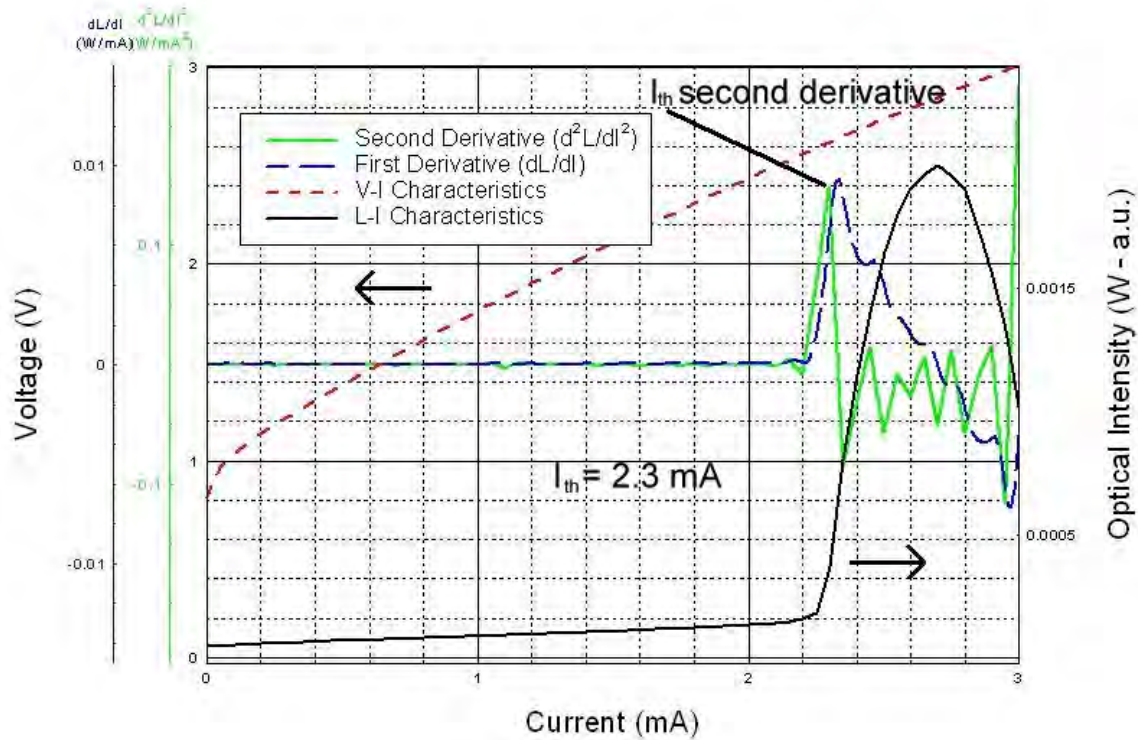


Figure 2.22: LIV curve of a QD VCSEL used to determine threshold current and slope efficiency

For VCSELs the main driver for the temperature dependency of the threshold current level is how the gain curve of the quantum dot region and the cavity resonant wavelength match up over temperature [29]. The gain curve peak of a quantum dot active region will shift to longer wavelengths as temperature increases at a rate greater than the rate the cavity mode wavelength shifts. Although it is commonly thought that the minimum threshold current is at the temperature when the peak gain and lasing

wavelength match, experimental results have shown that the minimum threshold can occur at a temperature at which the cavity and gain are detuned [29]. The gain curve of a quantum dot active region is affected as a whole by bandgap reduction from increased temperature, but other factors affect the gain as well. Numerous studies have examined the effects of temperature on the PL spectrum of quantum dots and have come to the conclusion that with an increase in temperature, the emission energy is red shifted, the PL FWHM decreases up to a certain temperature then increases, and the PL intensity shows little change up to a certain temperature and then decreases considerably [22].

While the gain curve red shifts and is reduced in amplitude by increased temperature, the cavity resonance shifts towards longer wavelengths due to changes in the refractive index and physical length of the cavity. The laser cavity is typically only the length of one to six times the lasing wavelength in the cavity. The lasing wavelength can be expressed as

$$\lambda_R = \frac{n_{spacer} h_{spacer}}{x} \quad (2.30)$$

where  $n_{spacer}$  is the effective index of the cavity,  $h_{spacer}$  is the corresponding physical thickness and  $x$  is the number of wavelengths of the cavity (i.e.  $2\lambda$ ,  $3\lambda$ , etc.). The lasing

wavelength depends on changes to the index and physical length versus temperature and can be expressed as [26]

$$\frac{\partial \lambda}{\partial T} = \frac{\lambda_R}{n_g} \left[ \left. \frac{\partial n_{spacer}}{\partial T} \right|_{\lambda} + n_{spacer} \left. \frac{\partial h_{spacer}}{\partial T} \right|_{\lambda} \right] \quad (2.31)$$

where  $n_g$  is the group refractive index of the spacer layer expressed as [26]

$$n_g = n_{spacer} - \lambda_R \left. \frac{\partial n}{\partial \lambda} \right|_T \quad (2.32)$$

Figure 2.23 shows the temperature dependencies of the electroluminescence (EL) peak, the gain peak at threshold current, and the lasing wavelength of an InGaAs QD VCSEL [29]. The peak of the gain curve changes due to temperature at a greater rate than the lasing wavelength. Hence, the VCSELs are usually optimally designed with the cavity resonant wavelength several nanometers longer than the anticipated peak gain curve wavelength at ambient temperature. This allows the gain curve and cavity to tune in at operating temperatures for best performance.

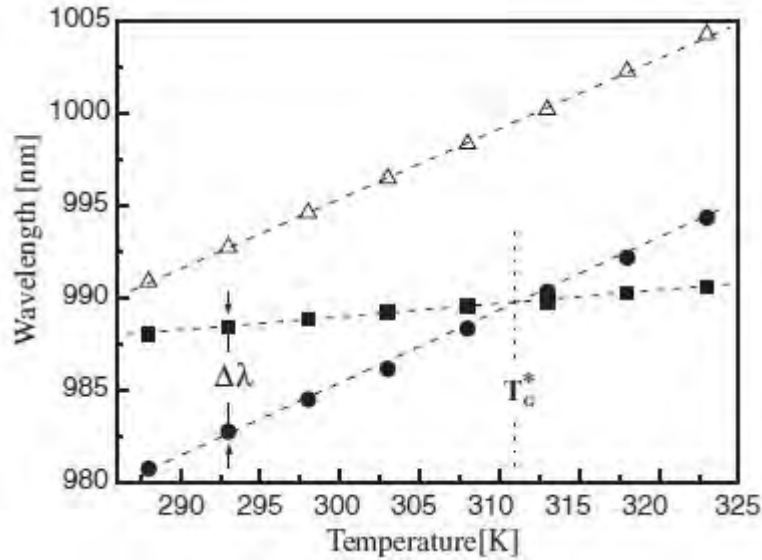


Figure 2.23: Temperature dependences of the EL peak position measured at low current density ( $\Delta$ ), VCSEL lasing wavelength ( $\blacksquare$ ), and gain-peak wavelength ( $\bullet$ ) at threshold currently density of the VCSEL.  $T_G^*$  is the temperature at which there is zero cavity-gain detuning [29]

Beyond detuning of the laser wavelength and gain curve peak, it has been suggested that there may be several factors contributing to the temperature sensitivity of quantum dot laser threshold current [30] including thermally induced spread of carriers among the inhomogeneous distribution of dot energy states, Auger recombination within the dots, carriers being thermally excited into the wetting layer, and other nonradiative recombination in the deeper dot energy states. One study explained these effects with processes called thermal coupling and photon coupling [31]. Thermal coupling is the monotonic non-ideal process where carriers in the excited states of quantum dots are thermally excited over the finite potential barrier to wetting layer states or confinement layer states. It causes red shift, spectral narrowing and intensity increase with increased temperature. Photon coupling occurs at or above threshold current, and involves photon absorption back into the QD ground states or the excited states of larger QDs. The photon coupling mechanism (PCM) can increase or decrease with temperature. Therefore PCM can cause spectral intensity decrease and wavelength red shift with increased

photon coupling or vice versa as temperature increases. PCM can explain reports of decreases in nonradiative Auger recombination and negative characteristic temperatures reported in studies of devices that use p-doping to reduce the temperature sensitivity of the threshold current [32, 33]. Auger recombination is where an electron absorbs the energy of an electron-hole recombination and is ejected from a QD energy level instead of a photon being released. Auger recombination has been found to be the dominant form of nonradiative recombination in 1.3 $\mu\text{m}$  QD VCSELs and has been found to decrease with temperature [34].

The slope of the L/I curve (optical intensity vs. input current) after threshold is referred to as the slope efficiency, and has been shown to be a function of junction temperature [34]. The slope efficiency decreases slowly as temperature increases then drops off sharply at a given temperature usually coinciding with point of thermal roll off as thermal non-radiative recombination increase [35]. The slope efficiency is an indication of the level of net gain (gain minus losses) in the cavity and how many QDs are involved in lasing. The slope efficiency can be examined to assess the density and uniformity of the QD ensemble within a VCSEL active region, assess the extent of non-radiative losses in the device and possibly provide insight into how to optimize devices.

## 2.6 Transverse VCSEL Modes

Although VCSEL cavity lengths are short enough to allow only one longitudinal mode, lateral or transverse modes have presented a challenge to oxide confined QD VCSELs causing non linear intensity versus drive current, and shifts in the lasing wavelength. VCSELs with small oxide aperture diameters of 4  $\mu\text{m}$  or less operate in a single fundamental transverse mode, but small apertures can reduce output power and device lifetime, and cause high electrical resistance. Therefore much research has been conducted to develop ways to create single mode VCSEL laser by suppressing the higher

order transverse modes in larger diameter devices [36]. Some methods researched involve modifying the VCSEL surface to induce losses in the higher order modes or promoting the fundamental mode by etching or modifying the surface of the top DBR [37, 38, 39]. However, these methods can create devices with high threshold currents. The transverse modes in VCSEL cavities are believed to be the result of non-uniform current injection into the active region and higher carrier densities around the edges of the active region especially as the device diameter increases [40]. This is a problem in through DBR contacted VCSELS, but mainly a problem in intracavity contacted VCSELS because the current is confined to the exterior of the device through a narrow path to the active region. Top DBR contacted VCSELS have a more direct current path, however, an asymmetric selectively oxidized confinement layer can also cause non-uniform current distributions through the active region.



### III. Fabrication and Experimental Methodology

#### 3.1 Introduction

This study characterized vertical cavity surface emitting lasers and involved developing a fabrication process, fabricating optical microcavity devices, characterizing devices and optical properties, and to some extent device design. A summary of the fabrication and the tests performed on each sample is shown in Table 3.1. A mask set was designed and fabricated specifically for this study that allowed precision fabrication of intra-cavity contacted VCSELs and measurement of optical transmission, electroluminescence and electrical characteristics (current vs. voltage). Five different optical micro-cavity devices were fabricated, an RCLED designated SH118, an intra-cavity contacted, dielectric DBR VCSEL designated V17, an intra-cavity, oxide DBR VCSEL (V19), and two through DBR contacted VCSELs (NSC-336 and DO177e). All the devices were grown on GaAs wafers using solid source molecular beam epitaxy (MBE). The RCLED (SH118) devices were fabricated using a VCSEL mask set made by AFRL/Rydd. The V17 VCSEL devices were fabricated using an AFIT mask set designed by Captain Jeremy Raley while he attended AFIT. All other devices used the mask set that was designed and fabricated as part of this study. Tests conducted during

Table 3.1: Summary of Micro-cavity Device Fabrication and Experimentation

Micro-Cavity Device		Cavity Size	Oxide Apertures	Results of Device Fabrication/Experiments		
Designation	Type			Electroluminescence?	Lasing?	Optical Transmission?
SH118	Intra-cavity Contact	$6\lambda$	2	Yes	N/A	No
V17	Intra-cavity Contact	$6\lambda$	2	Yes	No	Yes
V19	Intra-cavity Contact	$6\lambda$	2	No	No	Yes
NSC336	Through DBR Contact	$2\lambda$	1	Yes	No	Yes
Do177e	Through DBR Contact	$2\lambda$	1	Yes	Yes	Yes

this study included optical cavity transmission measurements versus wavelength, electroluminescence, electrical characteristics (voltage vs. current), and optical intensity and current versus voltage applied.

### 3.2 Mask Set Design

Three mask sets were used for this study, an AFRL VCSEL mask set, an AFIT VCSEL mask set and the mask set designed specifically for this study (see Figure 3.1).

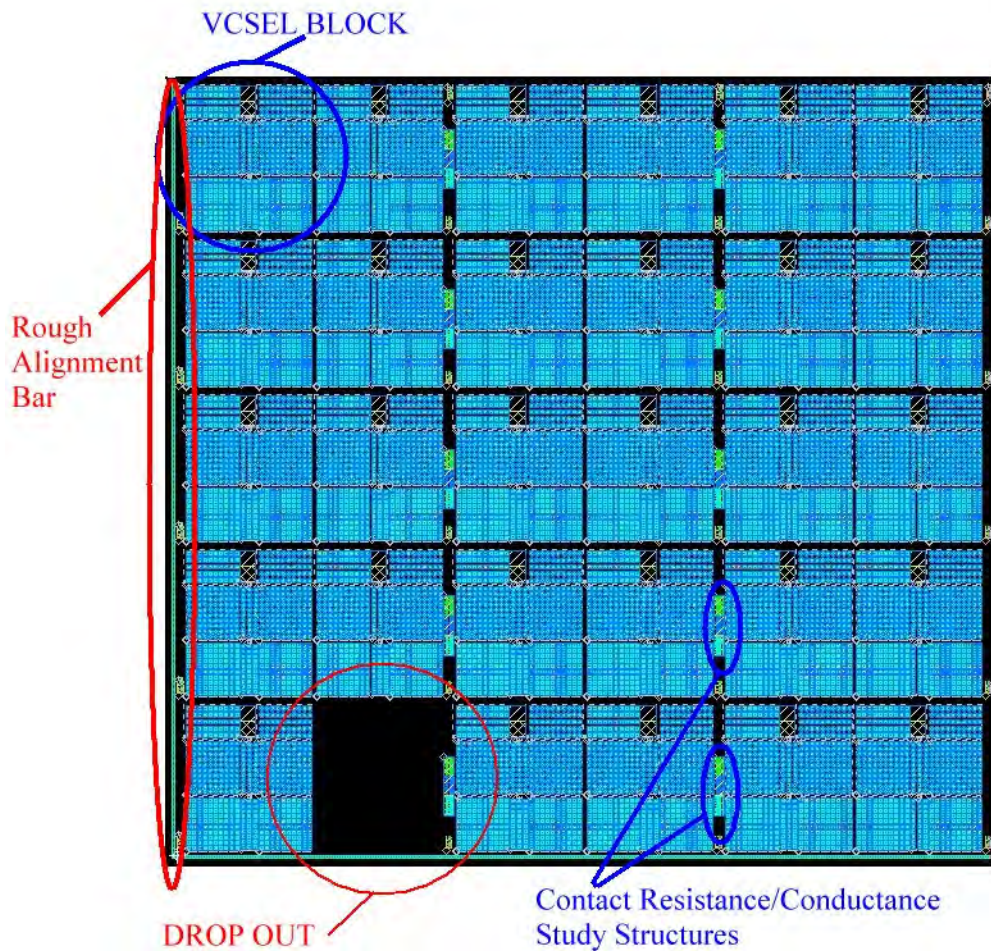


Figure 3.1: AFIT/AFRL Intracavity contact VCSEL mask with optical drop out and 29 blocks of microcavity devices

This mask set was designed using LASI (Layout Software for Individuals) version 6. Although the mask set was designed for intra-cavity contacted VCSELs, it can be used for top DBR or “Through DBR” contacted VCSELs. The mask set (shown in figure 3.1) is made up of one 0.48 x 0.56 mm “Drop out” for reflectance monitoring during the mesa etches and 29 identical blocks of structures and devices (shown in figure 3.2). Among other structures, each block contains optical transmission windows spaced periodically,

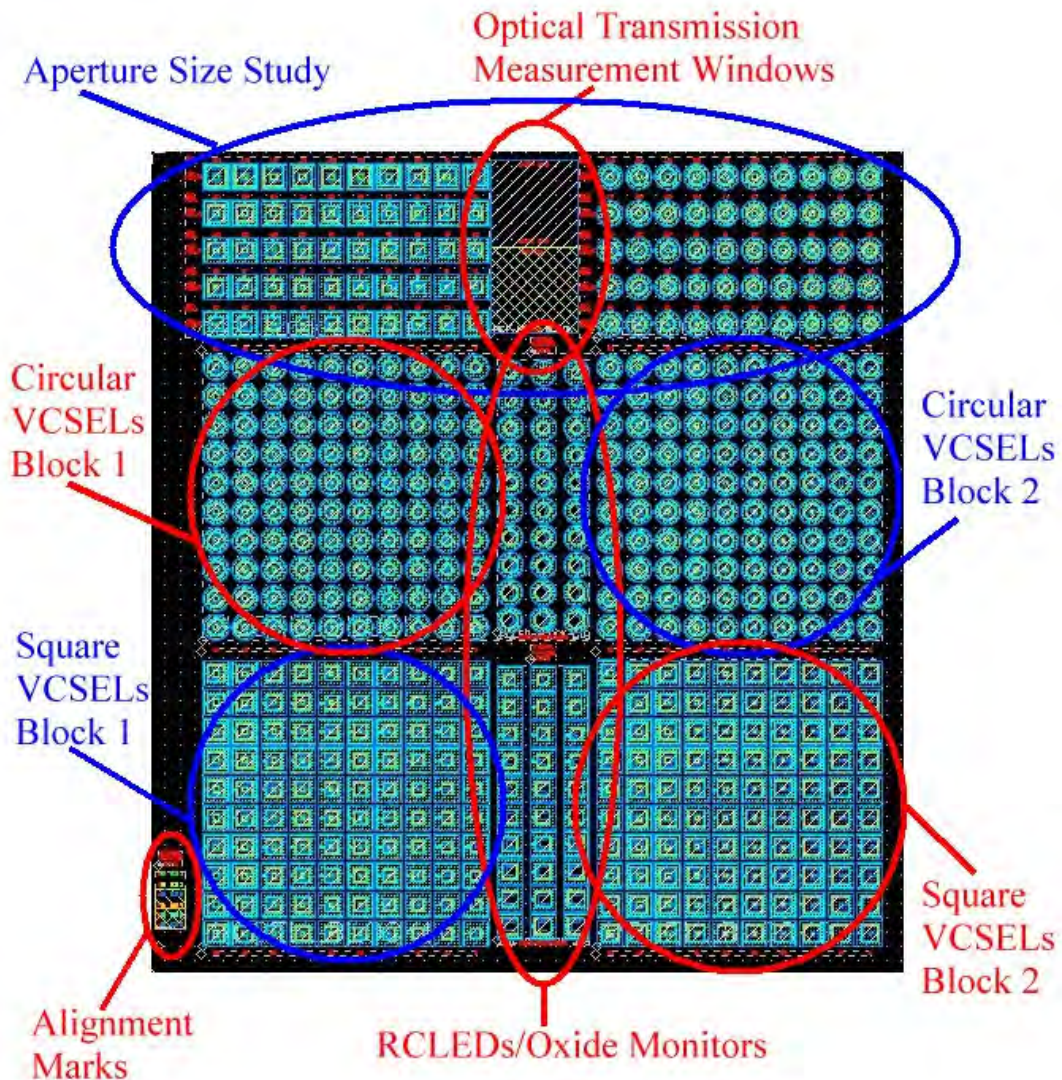


Figure 3.2: AFIT/AFRL Intracavity contact VCSEL mask

so that power transmission can be measured across the entire radius of the wafer. This is useful for analyzing the uniformity of the wafer and device layers. If the semiconductor layers aren't of uniform thickness, multiple transmission windows enable one to compare the optical transmission with the device electroluminescence because there's always a window in close proximity to a VCSEL device.

The VCSEL devices have two basic geometries, circular and square. Devices with both these geometries are present with variety of top DBR and contact (middle) mesa diameters. The top DBR mirrors have diameters from 5  $\mu\text{m}$  to 50  $\mu\text{m}$  in 5  $\mu\text{m}$  increments (i.e. 5, 10, 15, 20, ..., 50). The contact mesas (middle mesas) have diameters 50  $\mu\text{m}$  larger than the top DBR on half the devices (both squares and circles), and the other half of the devices all have contact mesas with a diameter of 110  $\mu\text{m}$ . During device oxidation, the varied middle mesa diameters allow the oxide apertures in all sized devices to close off an equal distance from the outer edge of the top DBR. The effective VCSEL apertures will vary among devices with different sized top DBR diameters. In the VCSELs with the same sized contact mesa, but different top DBRs, the effective aperture of the VCSEL will be the same with every sized top DBR mirrors. These devices will all get pinched off at the same time, so larger mirrored devices can be made without closing off smaller diameter devices and reducing device yield.

In each of the 29 device blocks, there are an additional 100 VCSEL devices immediately adjacent to the optical transmission windows. Square VCSELs are on the left side and circular VCSELs are on the right side. These VCSELs have top DBR diameters of 30  $\mu\text{m}$  to 50  $\mu\text{m}$  in 5  $\mu\text{m}$  increments. The contact mesa diameters of these devices range from 46  $\mu\text{m}$  to 64  $\mu\text{m}$  larger than the top DBR diameters in 2  $\mu\text{m}$  increments (i.e. 46,48,50,52, ...,64). This allows VCSELs with the same sized top DBR to be fabricated with ten different effective aperture sizes to facilitate optimization of device aperture size.

The RCLEDs are directly below the transmission windows. These devices are only fabricated when intracavity contacted VCSELs are made. They require at least the middle mesa etch and the middle mesa contact metal processes in order to function. If through DBR contacted VCSELs are fabricated then there's no middle mesa etch or middle contact metal, so the RCLED devices are not formed. The structure of the RCLEDs is the same as the intracavity contacted VCSELs except the RCLEDs don't have the top DBR mirror. The microcavity still has a significant resonance in the cavity because the GaAs/Air interface has a reflectance of about 0.3, but a broader spectrum of light is emitted because this reflectance is not as wavelength dependent as a DBR. This permits a better study of the luminescent properties of the material. The top metal contacts only cover a portion of the top of the device, so that the oxide layer can be clearly seen in order to monitor the progress of the oxidation.

The mask set consists of seven separate mask plates. These are labeled as "Alignment," "Top Metal," "Top Mesa," "Middle Metal," "Middle Mesa," "Bottom Metal" and "Bottom Mesa." The "Alignment" mask is a light-filled (dark field) mask that contains all the alignment marks and the device and structure labels. Similar to the "Alignment" mask, all of the metal masks, "Top Metal," "Middle Metal" and "Bottom Metal" are dark field masks and contain the patterns for the top contacts, middle contacts (top contacts for intra-cavity contact VCSELs) and bottom contacts respectively. All the mesa masks are light field masks, and contain patterns for the top, middle and bottom mesas as well as the optical transmission windows.

### **3.3 Device Fabrication**

Five different micro cavity devices were fabricated during the course of this study including an RCLED, an intra-cavity contacted VCSEL with an oxide top DBR mirror , an intra-cavity contacted VCSEL with undoped semiconductor DBR mirrors and two

through DBR contacted VCSELs. All the device fabrication processes used the same metal contact process and reactive ion etching process but the photolithography process evolved as the study proceeded.

All the microcavity devices involved in this study have a *pn* semiconductor junction and required both a *p*-type and an *n*-type metallization process common to all devices. The *p*-type metallization process was used for the top contacts and consisted of a 300 Å layer of titanium (Ti), followed by 500 Å of platinum (Pt) and 3500 Å of gold (Au). The *n*-type metal contacts consisted of 50 Å of nickel (Ni), 170 Å of germanium, 330 Å of gold, 150 Å of nickel, followed by a final layer of 3000 Å of gold. Immediately prior to the metallization process, the samples were dipped in a solution of BOE:DIW (1:10) for 20 seconds to remove any oxidation and impurities on the semiconductor surface. The samples were all metalized in an electron beam evaporative metallization unit.

All the microcavity devices fabricated in this study required a dry etch process called a reactive ion etch (RIE) to form the mesa structures. Although the etch times varied, the other etching process parameters were the same for all the devices and are listed in Table 3.2. An additional, dual chamber RIE was used in processing the DO-177e VCSEL sample for the fluorine etch used for etching and removing the Si<sub>3</sub>N<sub>4</sub> mask used for the mesa etch. Information on this process is included later in the DO-177e processing section. Table 3.3 provides a summary of the oxidation furnace processing of the various samples.

Table 3.2: Reactive Ion Etch Data

Date	Sample	DC Bias (Volts)	Etch Depth (Microns)	Etch Time (seconds)	Etch Rate (microns/sec)	Photoresist Mask
9/17/2003	SH118	178	2.1	120	0.018	pmgi/sf11
10/20/2003	V17	175	6.2	178	0.035	1818
10/22/2003	V17	177	1.55	93	0.017	1818
1/30/2004	V17	144	6.3	325	0.019	2x1818
1/30/2004	V19	147	2.75	104	0.026	2x1818
2/3/2004	V19	137	2.2	135	0.016	1813
2/3/2004	V17	139	1.6	69	0.023	1813
2/4/2004	V17	148	1.8	103	0.017	1813
2/19/2004	nsc336-2	166	14	637	0.022	1818
2/26/2004	nsc336-3	168	7.2	384	0.019	1813/SiN4
4/23/2004	DO-177e	154	6.5	355	0.018	1813/SiN4

Values common to all etches were Cl<sub>2</sub> gas at 10 sccm, BCl<sub>3</sub> gas at 30 sccm, pressure at 4 mTorr, RIE power at 50 watts and inductively coupled plasma(ICP) power at 500 watts

Table 3.3: Oxidation Furnace Data

Sample	Time (min)	Temperature(°C)	Pressure(Torr)	H2O Flow(sccm)
Sh118-1	0	400	5	500
Sh118-2	30	400	5	500
SH118-3	105	400	5	500
V17	80	400	5	500
NSC336	90	400	5	500
DO177e-1	20	400	5	500
DO177e-2	20	400	5	500

**3.3.1 RCLED (SH118) Fabrication.** A single SH118 RCLED sample was fabricated during this study using a VCSEL/RCLED mask developed by AFRL/RYYDD. The SH118 device geometry and layer structure are shown in Figure 3.3. The device has a 2.1 μm GaAs optical cavity with two oxide layers for current confinement. The bottom of the cavity has a 12 period GaAs/AlGaAs DBR mirror. P-type metal contact layer (Ti-Pt-Au) was evaporated on to the wafer and then lifted off to form the top contact rings.

The wafer was patterned with two layers of photoresist, one layer of SF-11 PMGI (poly dimethylglutarimide) photoresist followed by a layer of 1805 photoresist that was used to pattern the PMGI resist and then left on the sample to provide more protection during the etching process. However, both layers of photoresist were completely removed during the etching process. However, both layers of photoresist were completely removed during the etching process and the tops of the devices were etched slightly forming a crater.

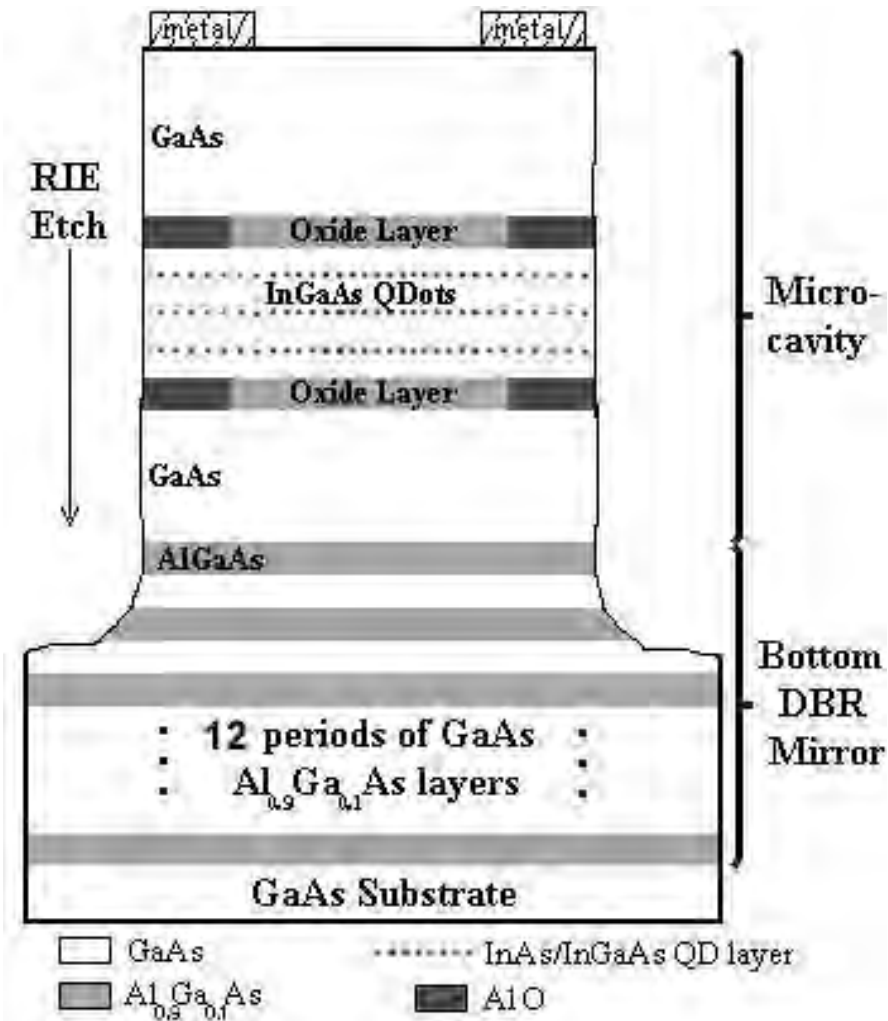


Figure 3.3: SH118 RCLED device structure



This feature did not prevent the LED from working, but likely affected the resonant cavity characteristics. All the devices fabricated in this study were dry etched with reflectance monitoring. The theoretical reflectance and refractive index profile for the RCLED is show in Figure 3.4.

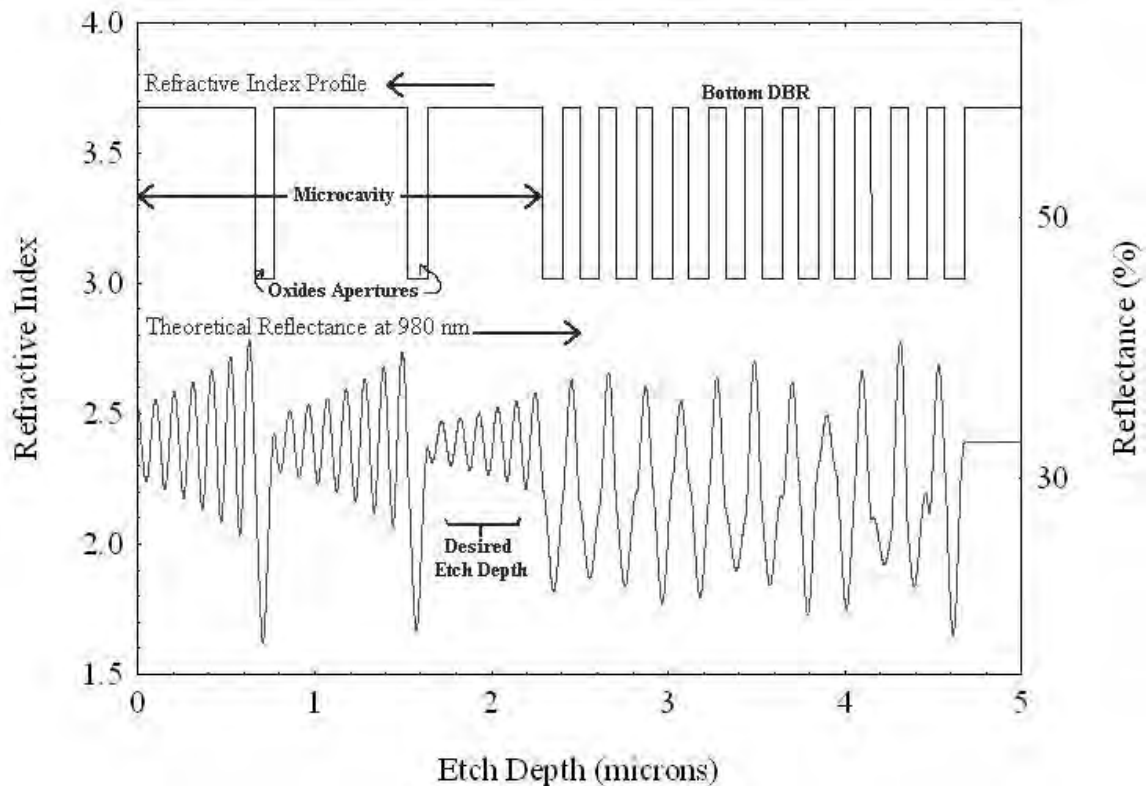


Figure 3.4: Refractive index and reflectance versus etch depth for SH118 RCLED devices

The actual reflectance data for the RCLED etch was lost during the procedure due to an equipment error and is unavailable. The etch depth was measured at  $2.1 \mu\text{m}$  with a profilometer as seen in Figure 3.5. The  $3700 \text{ \AA}$  metal layer and crater on the top of the mesa are also evident in Figure 3.5. The depth of the depression was about  $0.25 \mu\text{m}$ , but it was clearly visible under a microscope. After the mesa etch, *n*-type metal (Ni-Ge-Au-

Ni-Au) was evaporated on the back side of the sample to provide a negative electrical contact for all the devices. The original sample was cleaved into three samples, one that wasn't oxidized, one oxidized for 30 minutes, and the last oxidized for 105 minutes. The 5  $\mu\text{m}$  devices no longer conducted current after 30 minutes of oxidation. However, the next larger sized devices (10  $\mu\text{m}$ ) never completely closed off despite over an hour of oxidation. Thus, I was unable to get reliable data on oxidation rates (oxidation distance versus time) from these samples to use on future device fabrication.

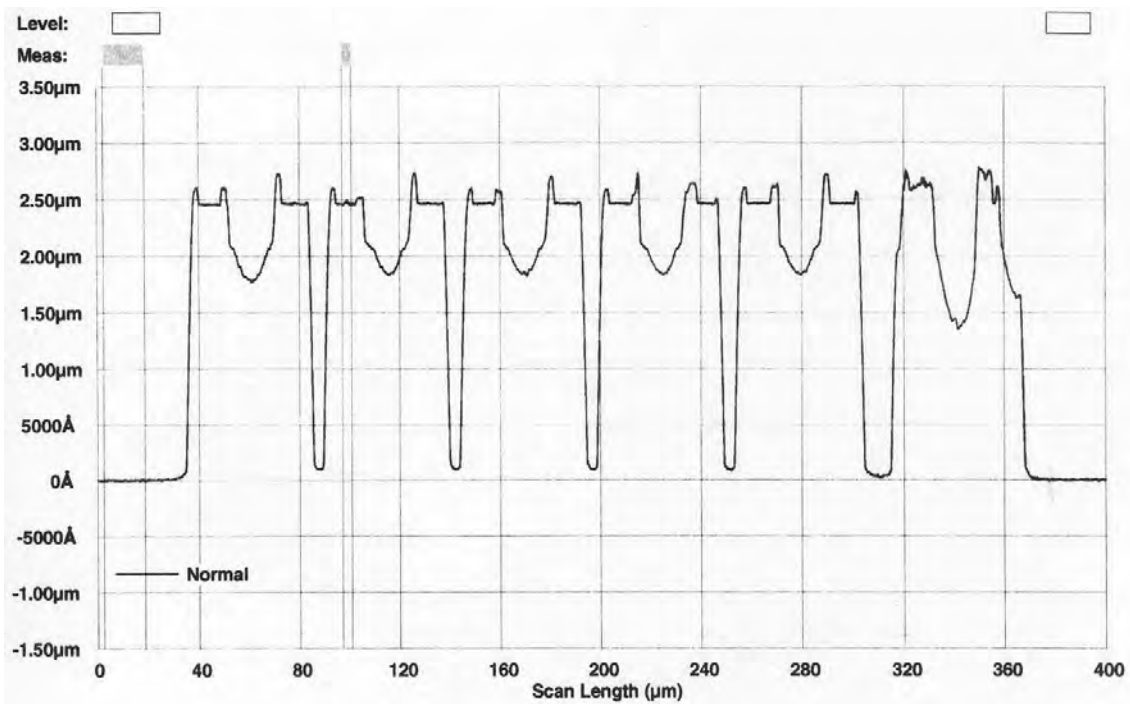


Figure 3.5: Profilometer measurement graph for SH118 RCLED devices

**3.3.2 VCSEL V17 Fabrication.** Two samples of the V17 VCSELs were fabricated (V17 and V17A). One with the AFIT VCSEL mask set (V17) and one with the mask set created in this study (V17A). The V17 VCSEL is intracavity contacted and the structure is shown in Figure 3.6. The structure is identical to the SH118 RCLED except a

29 period DBR is grown on top of the microcavity. The top mesa was etched, and then the  $p$ -type metal layers were deposited and lifted off to form the top metal contacts. Next, the middle mesa was etched, and the  $n$ -type metal was deposited and lifted off to form the bottom metal contacts. During the top and middle mesa etches, the reflectance of sample

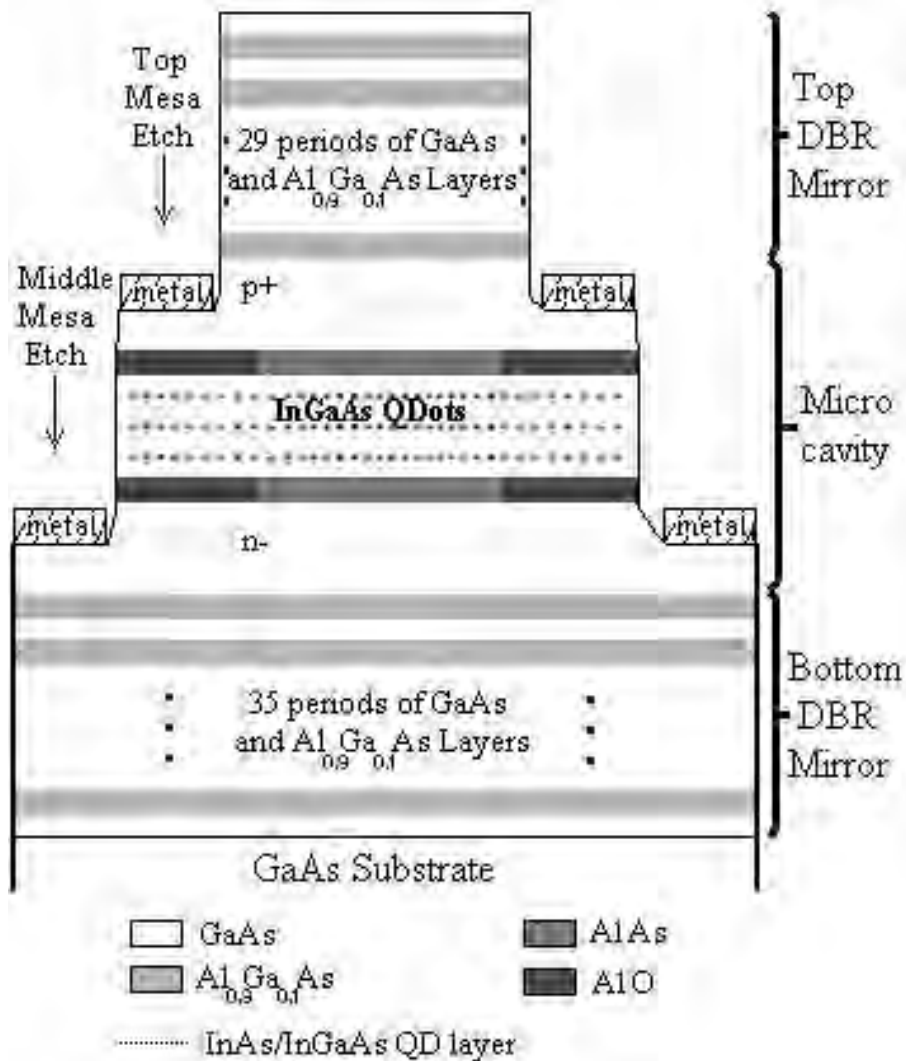


Figure 3.6: V17 VCSEL device structure

was monitored to keep track of the etch depth. The theoretical reflectance, actual reflectance and refractive index profile for the VCSEL is show in Figure 3.7. The reflectance monitoring indicated that the first mesa was etched approximately 6.2  $\mu\text{m}$  and that the middle mesa etch was about 1.5  $\mu\text{m}$  deep. The sample was tested for electroluminescence prior to any oxidation and then oxidized for 80 minutes. The different diameter devices were checked for conductivity to attempt to determine the depth of the oxide layer, but it appeared that the sample was not affected by the oxidation process. The lack of sufficient space between the mesa edge and metal contact layers seemed to prevent an even oxidation or any oxidation of the oxide layer at all.

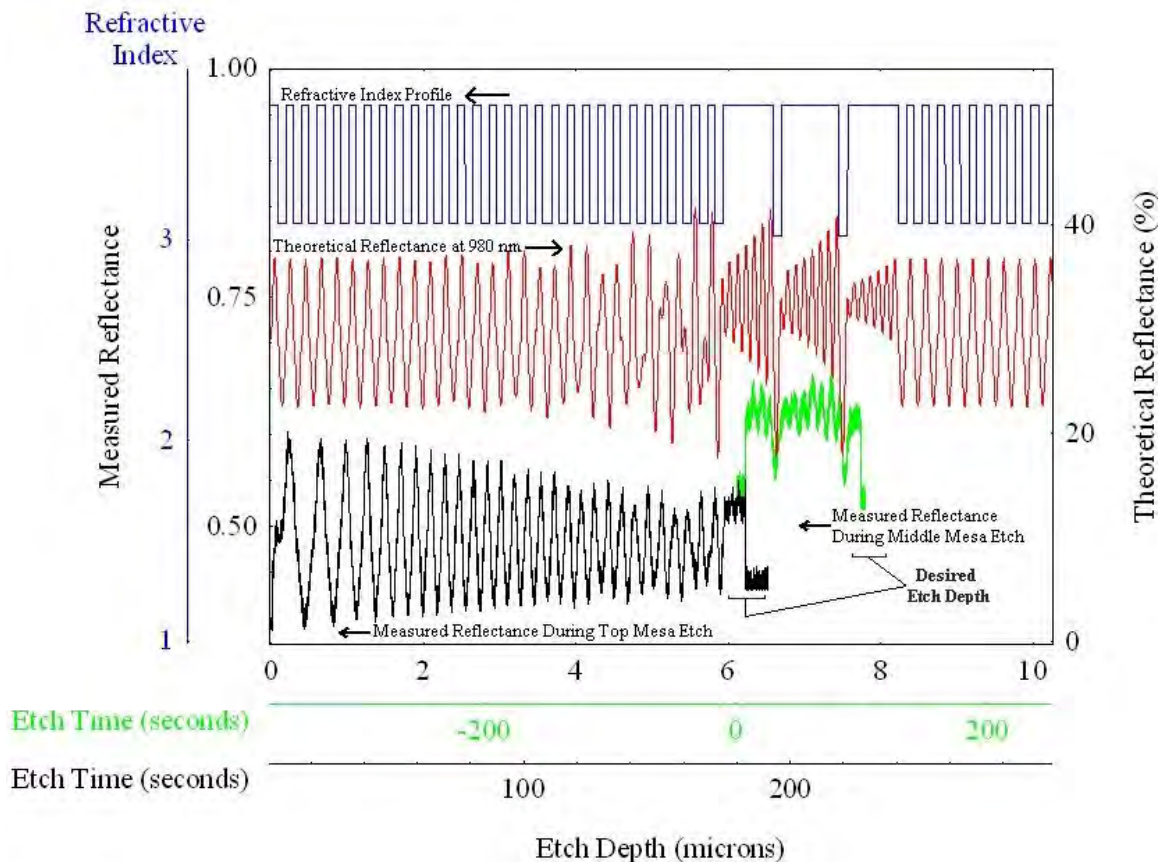


Figure 3.7: Refractive index and reflectance versus etch depth for V17 VCSEL devices

3.3.3 VCSEL V17A Fabrication. Sample V17A was fabricated using the VCSEL mask designed in this study, but the sample was over etched during the middle mesa etch. Figure 3.8 shows the reflectance data from the etches on sample V17A and how the third etch went too far into the wafer. The cavity size for VCSEL samples V17 and V19 was thought to be  $10\lambda$  ( $3.2 \mu\text{m}$ ) but was actually  $6\lambda$  ( $2.1 \mu\text{m}$ ). During the first middle mesa etch, the reflectance pattern was monitored and the etch process was stopped at the correct depth. However, the mesa height was measured at  $1.6 \mu\text{m}$  with the profilometer, so I had the sample etched an additional amount that turned out to be too deep for both cavity size specifications ( $10\lambda$  and  $6\lambda$ ).

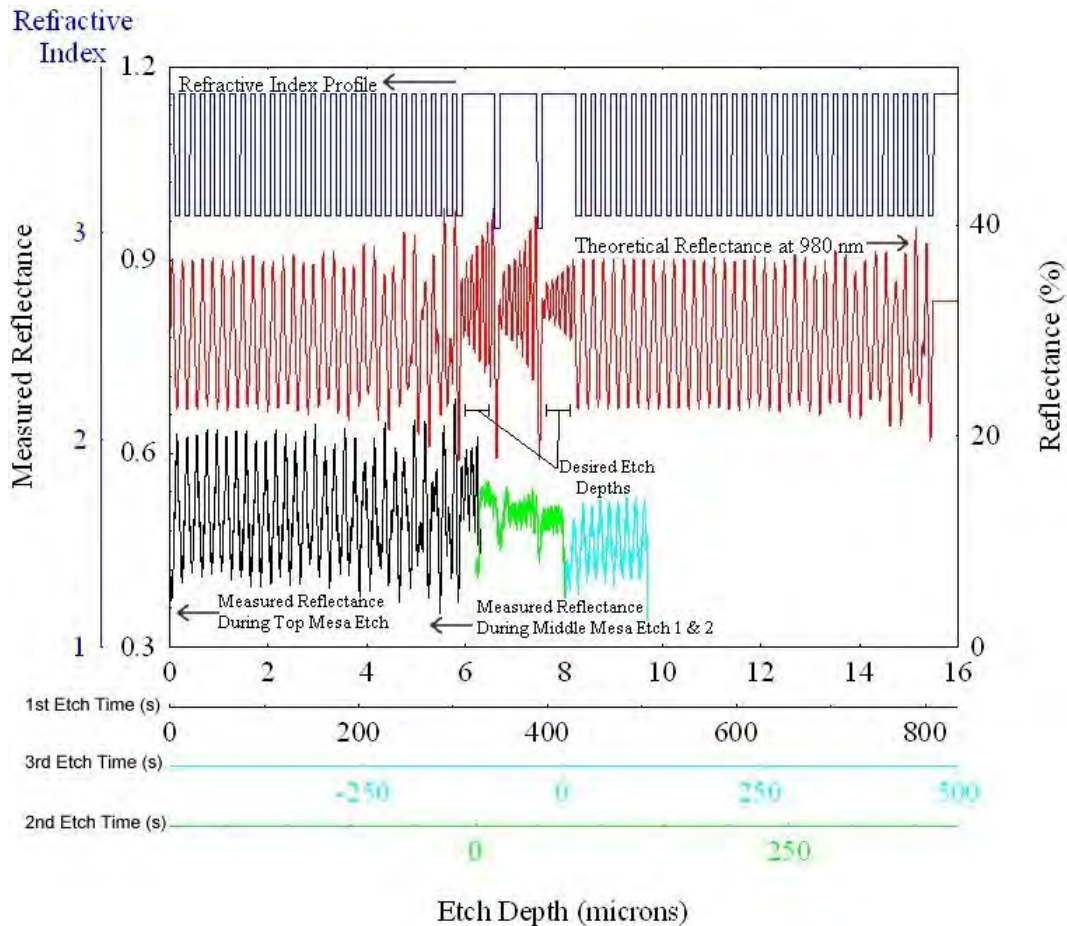


Figure 3.8: Refractive index and reflectance versus etch depth for V17A VCSEL devices

The additional amount put the depth of the third etch into the bottom DBR layers that are undoped and non-conductive. Thus, the bottom metal contacts were deposited on nonconductive layers, so the devices did not conduct a current or produce light. Figure 3.9 and Figure 3.10 show the profilometer measurements for the V17A top mesa, and both middle mesa etches. The profilometer measurements show that the reflectance monitoring was a very accurate method of controlling the etch depth. No oxidation was performed on sample V17A because none of the devices worked.

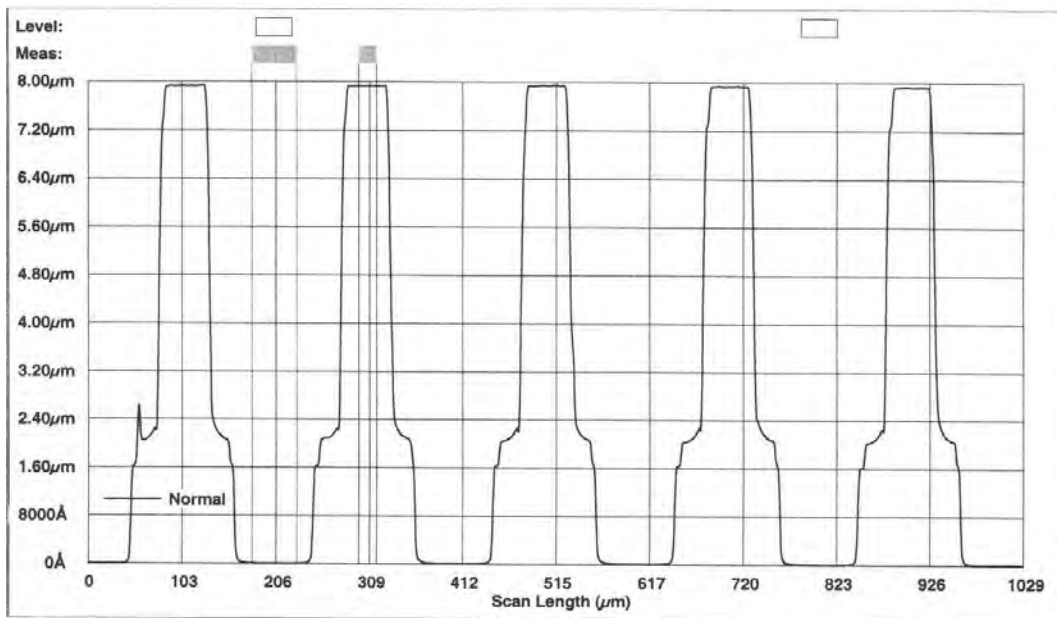


Figure 3.9: Profilometer measurement of sample V17A after top mesa (6.3 μm), top metal contact deposition, and the first middle mesa etch (1.6 μm)

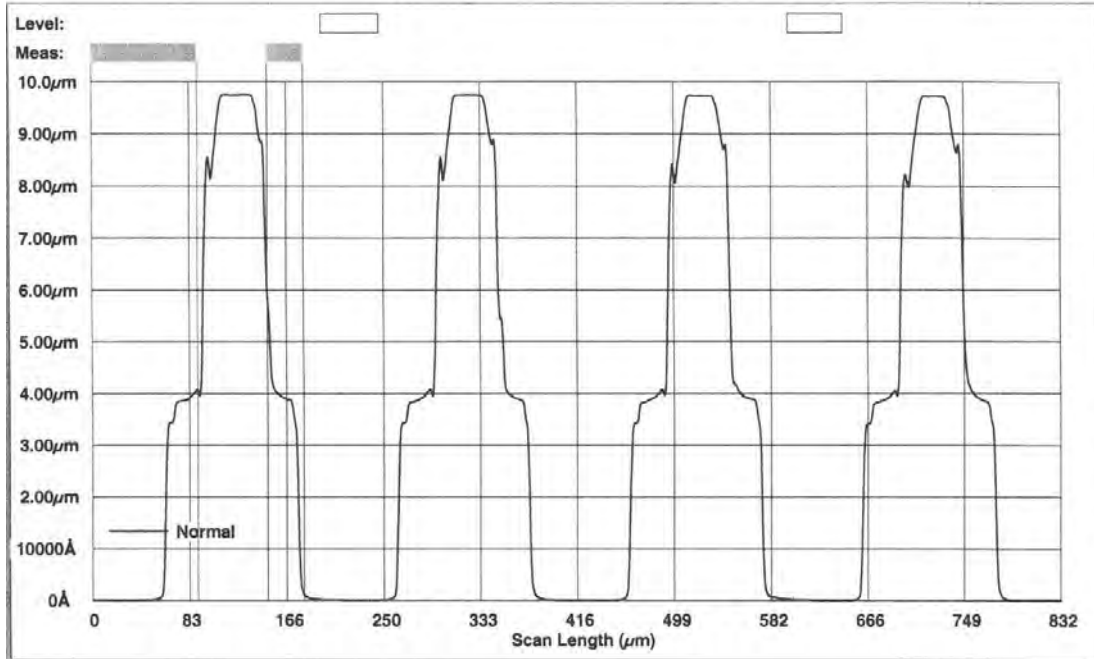


Figure 3.10: Profilometer measurement of sample V17A after top mesa, top metal contact deposition, and the first and second middle mesa etch

3.3.4 *VCSEL V19 Fabrication.* Sample V19 was an oxide DBR VCSEL with intracavity contacts. V19 was fabricated using the VCSEL mask designed during this study, but the fabrication did not yield any working devices. The middle mesa etch went too deep because the amplitude of the reflectance data was low. This made it difficult to see the transition between the cavity and the DBR layers. The middle mesa etch was too deep and the bottom metal contacts were deposited on undoped bottom DBR layers. The RIE and reflectance monitoring data are shown in Figure 3.12. From the figure, it can be seen that the top mesa etch reflectance was fairly well defined compared to the middle mesa etch. The amplitude of the reflectance monitoring signal can be affected by the alignment of the reflectance monitoring laser and sensor, the output intensity of the laser, and the optical loss of the semiconductor layers. Despite that there were no working devices; the V19 sample was oxidized to check the optical transmission of the sample. The oxide DBR is designed to have the proper reflective properties after the layers have

been oxidized. However, good transmission data was not obtained because the transmission window was too large to get completely oxidized and the device apertures were too small to check for optical transmission.

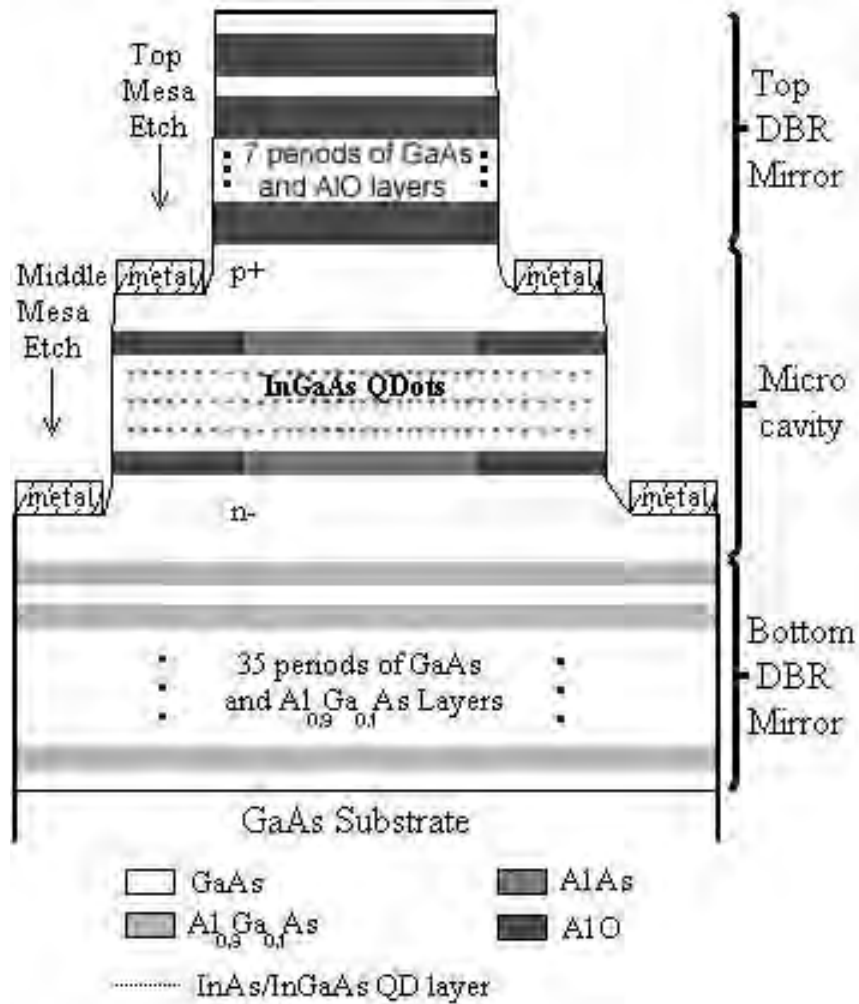


Figure 3.11: V19 VCSEL device structure



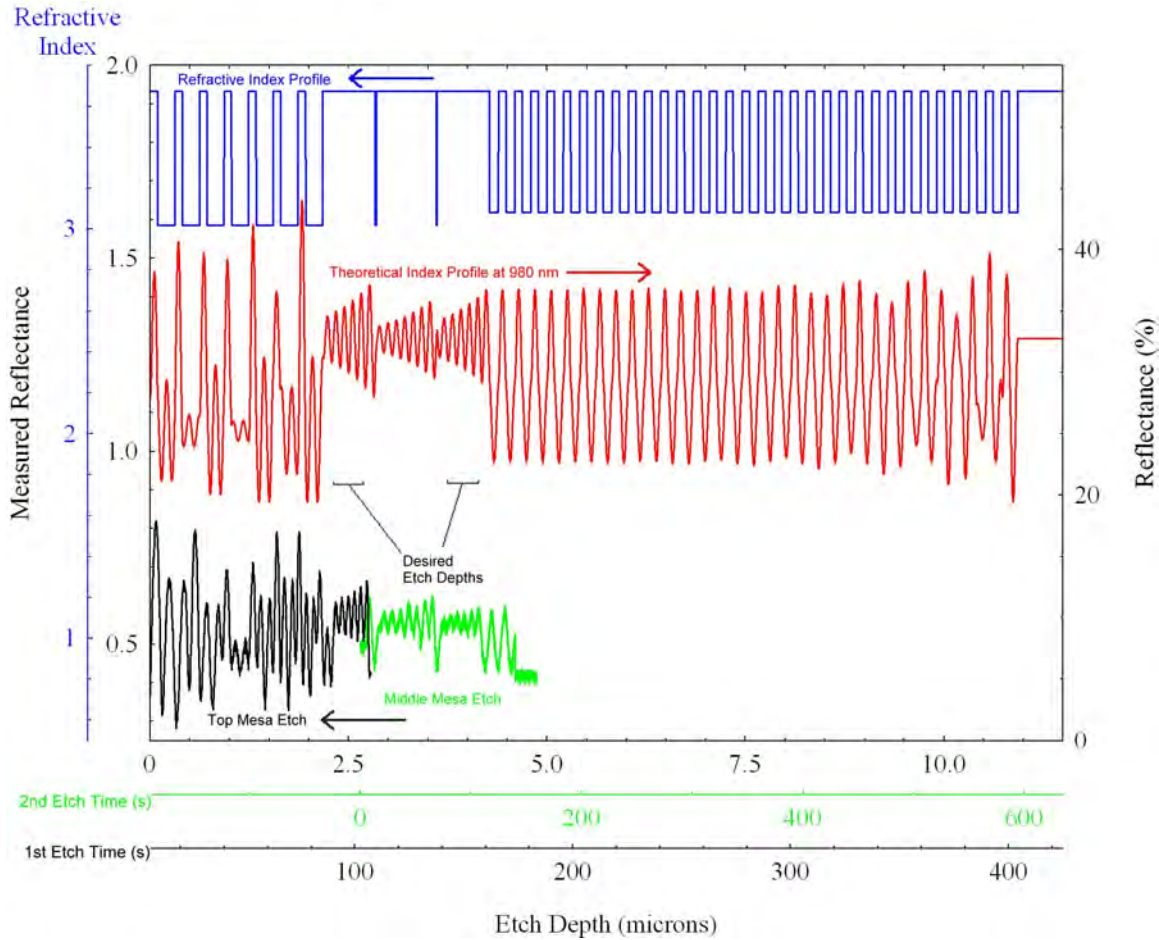


Figure 3.12: Refractive index and reflectance versus etch depth for V19 VCSEL devices

*3.3.5 Through DBR Contacted VCSEL Fabrication.* Samples NSC-336 and Do177eB are simple through-DBR contacted VCSELs that were also fabricated using the mask developed during this study. However, a silicon-nitride ( $\text{Si}_3\text{N}_4$ ) “Hard mask” was used to pattern the device mesas during the etching process. This helped significantly with the photoresist removal problem experienced while fabricating previous devices. Not only was the  $\text{Si}_3\text{N}_4$  mask much more durable and resistant to wear, but it was much more easily removed by selective etching with a Freon reactive ion etch (RIE). Table 3.4 shows the RIE information for the freon etches conducted on samples NSC-336 and Do177eB to pattern and also to remove the  $\text{Si}_3\text{N}_4$  masks.

Table 3.4: Reactive Ion Etch Data for Patterning and Removing Si<sub>3</sub>N<sub>4</sub> Masks

Sample	Freon 23 (sccm)	Freon 14 (sccm)	Pressure (mTorr)	RIE Power (Watts)	DC Bias (Volts)	Etch Depth (μm)	Etch Time (minutes)	Etch Rate (μm/min)	Photoresist Mask
NSC-336	47.4		57	99	265	0.8	40	0.020	1813
NSC-336		42.4	56	99	243	0.5	6	0.083	
Do177eB	46.5		57	97	269	0.31	17	0.018	1813
Do177eB	46.4		56	97	Unk	0.31	17	0.018	
Do177eB	46.4		56	99	246	0.31	17	0.018	

The through-DBR design used for samples NSC-336 and Do177eB only required one mesa etch to create the devices. Top metal contacts were patterned with 1813 photoresist and evaporated onto the wafers. The excess *p*-type metal was lifted off with tape, and then a layer Si<sub>3</sub>N<sub>4</sub> was deposited using a sputtering system. The layer of Si<sub>3</sub>N<sub>4</sub> was covered with a layer of 1813 photoresist patterned by typical UV exposure and developing process. Then the sample was put in the freon etching chamber to pattern the Si<sub>3</sub>N<sub>4</sub> mask in preparation for the device mesa etching. Sample NSC-336 was etched to form a mesa approximately 7.8 μm in height. Then bottom metal contacts were deposited around the base of the mesas. Figure 3.13 shows the completed device structure of a NSC-336 VCSEL with bottom metal contacts. The DBR layers are graded in order to reduce electrical resistance through the DBR, but putting the bottom metal contacts on the top of the wafer still reduces the overall electrical resistance of the device versus applying a backside metal contact. The device was etched using reflectance monitoring despite being a single mesa design that did not require an extremely precise etch depth to operate. An additional sample was etched completely through the VCSEL structure in order to determine the actual device structure to determine whether it was an intra-cavity contacted device or a thru DBR contacted device. Figure 3.14 shows the results of the NSC-336 device mesa etch measuring about 7.8 μm. The profilometer measurement of a NSC-336 device shown in Figure 3.15 indicates a mesa height of close to 8 μm. Other devices were measured with mesas measuring about 7.5 μm, so there appears to be some

variability with the RIE due to the conditions in the etching chamber of differences in the wafer material.

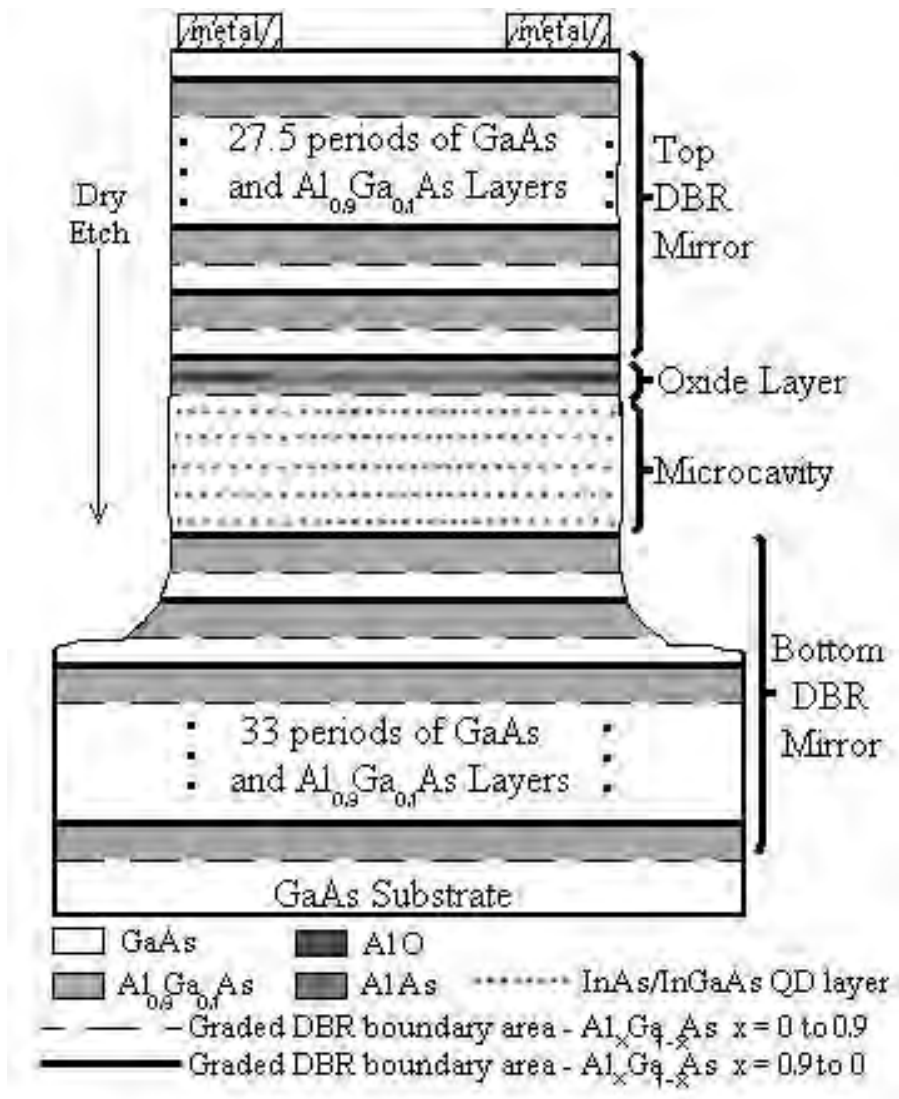


Figure 3.13: NSC-336 VCSEL device structure

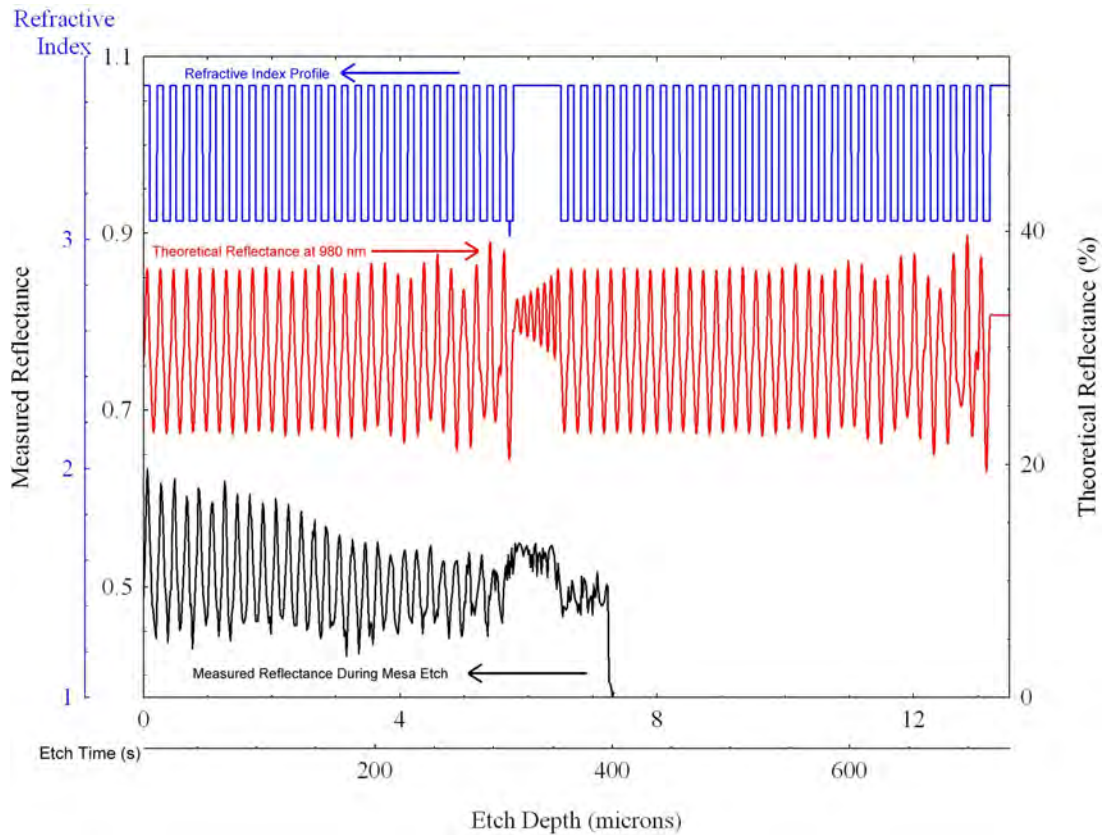


Figure 3.14: Refractive index and reflectance versus etch depth for NSC-336 VCSEL device

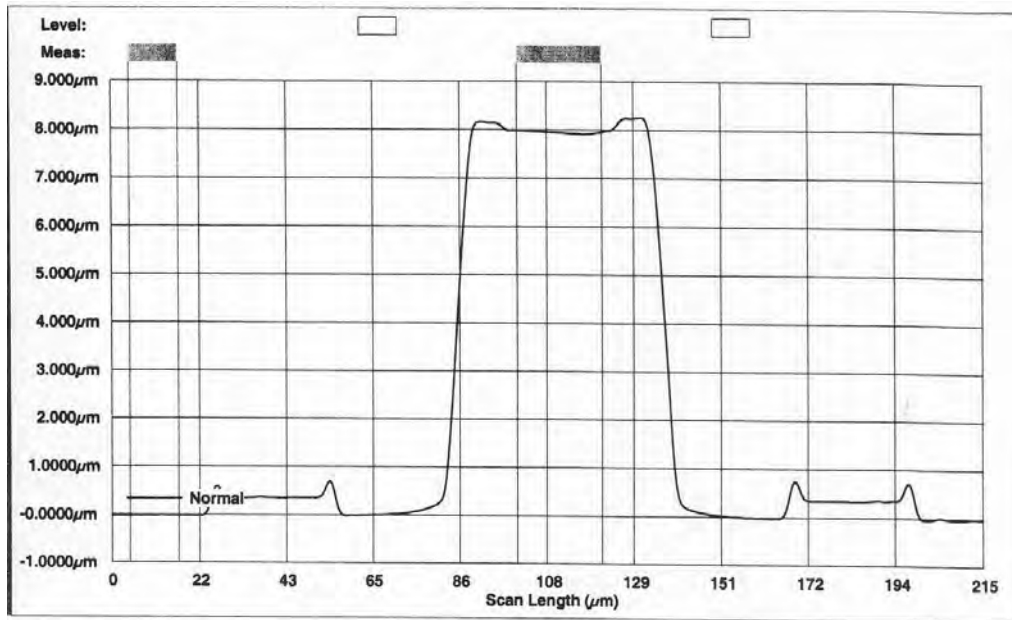


Figure 3.15: Profilometer measurement of a completed NSC-336 VCSEL device with bottom metal contacts

Sample Do177eB was also a through DBR contacted VCSEL similar to NSC-336. The device structure is shown in Figure 3.16. Do177eB was fabricated in a similar fashion as NSC-336, but a backside metal contact was deposited on Do177eB instead of bottom metal ring contacts. Only about  $0.31 \mu\text{m}$  of  $\text{Si}_3\text{N}_4$  was sputtered onto the Do177eB wafer because there was a large amount of excess  $\text{Si}_3\text{N}_4$  left over after the mesa etch of NSC-336. Prior to the Freon etch, the 1813 photoresist measured at  $1.35 \mu\text{m}$ , so the combined thickness of photoresist and  $\text{Si}_3\text{N}_4$  was  $1.66 \mu\text{m}$ . After the Freon etch to pattern the  $\text{Si}_3\text{N}_4$ , the combined thickness of photoresist and  $\text{Si}_3\text{N}_4$  was  $1.55 \mu\text{m}$ , so about

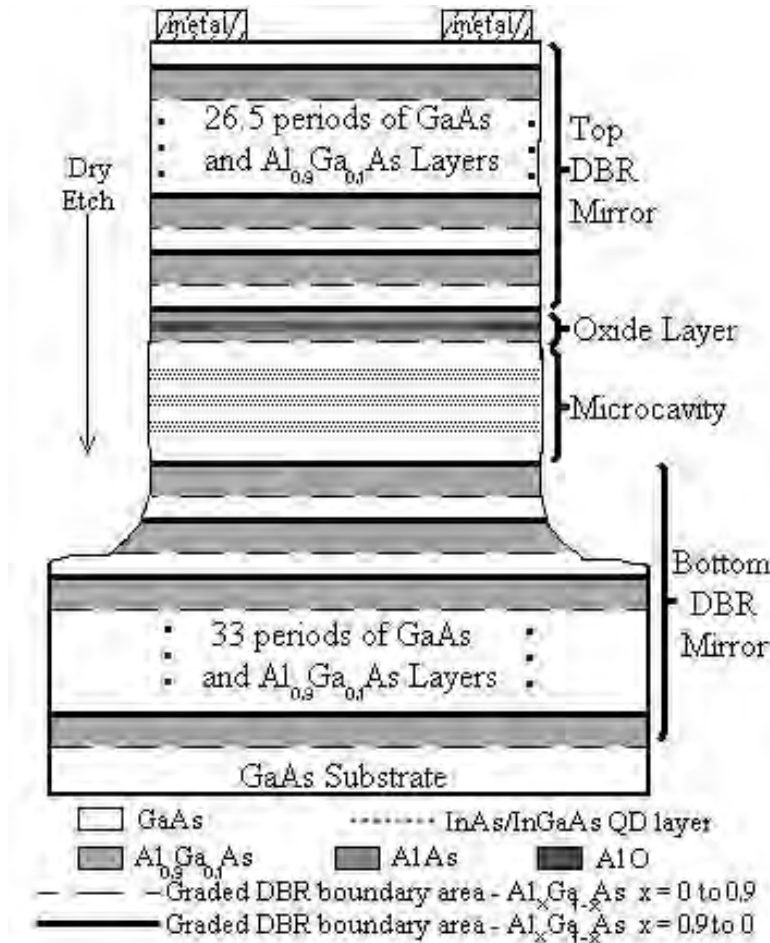


Figure 3.16: Do177eB VCSEL device structure

0.11  $\mu\text{m}$  of resist was lost during the Freon etch. Once the  $\text{Si}_3\text{N}_4$  mask was patterned, the mesa etch was accomplished. The results of the mesa etch are shown in Figure 3.17.

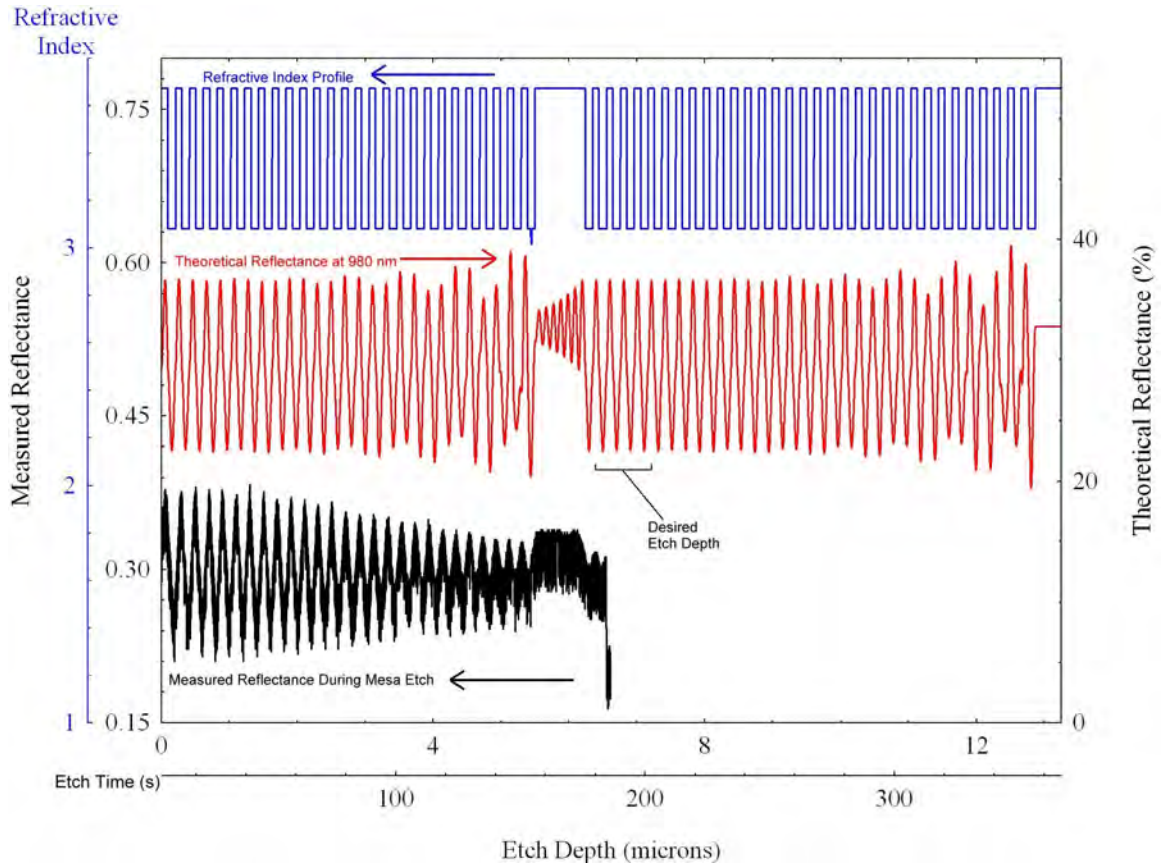


Figure 3.17: Refractive index and reflectance versus etch depth for Do177eB VCSEL device

The mesa height should be about 6.5  $\mu\text{m}$  according to the data from the reflectance monitoring. This was confirmed with the profilometer measurement of 6.81  $\mu\text{m}$  that included what was left of the  $\text{Si}_3\text{N}_4$  mask after the mesa etch. The rest of the  $\text{Si}_3\text{N}_4$  mask was removed with final 17 minute Freon etch. The completed device was not measured with the profilometer. Prior to oxidation, sample Do177eB was deposited with an *n*-type metal contact layer (50  $\text{\AA}$  of Ni, 170  $\text{\AA}$  of Ge, 330  $\text{\AA}$  of Au, 150  $\text{\AA}$  of Ni and

3000 Å of Au) on the back side of the wafer. Finally, the original sample was cleaved into two pieces, and one piece was placed in the oxide furnace at 400 °C for 20 minutes. The oxide depth for the first piece was desirable at about 3 μm, so the second piece was also oxidized at 400 °C for 20 minutes.

### 3.4 Optical Power Transmission Measurements

Measuring the optical power transmission of the wafers over a range of wavelengths provided insight into the optical characteristics of the cavity. The optical characteristics of the microcavity could then be compared with the output spectrum of devices. Prior to performing the measurement, the backside of the wafer was polished so that the surface wouldn't scatter the light passing through the wafer. The test setup is shown in Figure 3.18 and consisted of a white light source with a collimated output beam, a 386 Hz chopper, a SpectraPro 300i 0.3m spectrometer with 2 μm blazed grating with 300 grooves/mm, and an avalanche photodetector. The samples were placed in the mount and aligned using the beam reflected off the wafer surface. The spectrometer was scanned from 1100 to 1600 angstroms to ensure the entire "Stop band" of the cavity was covered. For some samples, multiple locations on the wafer were measured to check the consistency of layer thickness across the wafer. Generally, the layer thickness in the middle of the wafer is thicker than at the edges, so the resonant frequency is lower in the middle of the wafer. However, uniformity of layer thickness across the wafer is desirable for device production and will ensure that all the devices produce similar outputs.

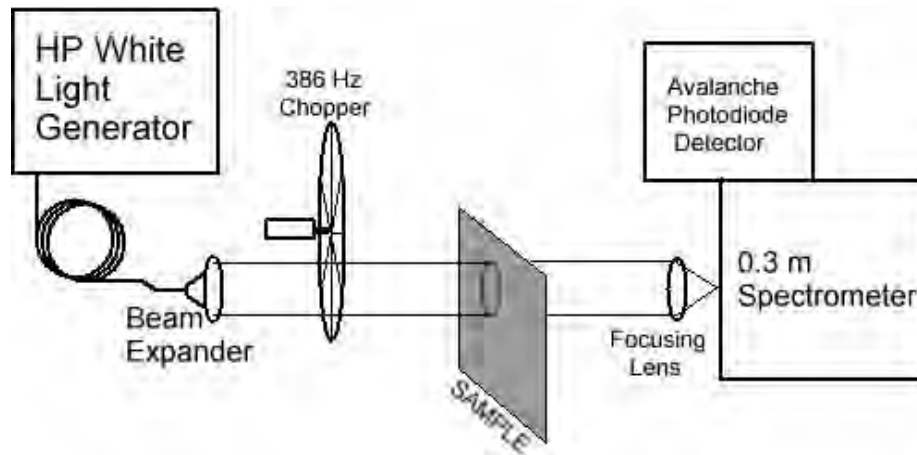


Figure 3.18: Optical power transmission measurement setup

### 3.5 Electro-Luminescence Measurements

The spectrum of light emitted from various samples was coupled through a multimode 50/125  $\mu\text{m}$  optical fiber and measured with an HP 70951B Optical spectrum analyzer under various conditions of device temperature and input current. The electroluminescence was studied for following samples: SH118, V17, NSC-336 and Do177e. An HP4145B semiconductor parameter analyzer (SPA) provided various input current levels to devices as the output spectrum was measured by the OSA. Output spectrum data versus drive current data was analyzed to characterize the optical properties of devices. All optical intensities measured were relative because of two reasons. First, not all the light output from the device was collected and coupled into the optical fiber. Second, the alignment and angle of the optical fiber varied from measurement to measurement. To set up each measurement, the optical fiber was adjusted to maximize the intensity of light indicated on the OSA. Once this alignment was peaked, it typically stayed peaked unless the temperature of the sample was changed causing expansion or contraction of the sample.

A temperature controlled stage was used to vary the sample temperature while the output spectrum was measured. As the temperature changed, thermal expansion caused



the sample to shift position, and required realignment of the optical fiber and to a lesser extent, the electrical probes. During cooling, the device chamber was flooded with nitrogen to prevent condensation and frost from building up on probes and device wafers. The devices were viewed through an optical microscope with a video camera to assist with electrically probing and aligning the optical fiber.

### **3.6 Optical Power, Current and Voltage (L-I-V) Measurements**

The optical power, current and voltage (LIV) measurements consisted of ramping current through the VCSEL device and measuring the resulting light output via a photodetector. The LIV measurements were conducted on the same probe station as the electroluminescence measurements with the HP 4145B SPA. The light output was measured with an extended range InGaAs photodetector with a responsivity of 0.697 A/W at up to 2.0  $\mu\text{m}$ . LIV measurements were taken at various temperatures and used to calculate threshold current, slope efficiency, and characteristic temperature (see chapter 2 for background on calculations). LIV data was transferred from the HP 4145B SPA to a PC via a Labview<sup>TM</sup> routine written by Dr. Robert Bedford of AFRL/RYPD.

### **3.7 Conclusions**

In this chapter I described the structures, fabrication, and testing of an RCLED and four different VCSEL devices. I discussed issues encountered during fabrication and the new mask set developed for VCSEL and RCLED fabrication to solve some issues. Some significant issues included etching device mesas to the proper depth and determining the best thickness and combination of photoresist to use for an etch mask. I described three methodologies to take measurements used to characterize each device's optical transmission, electroluminescence, and optical intensity and voltage versus drive current (LIV).

## IV. Results and Analysis

### 4.1 Introduction

In this chapter I present data collected from and analysis of four different optical microcavity devices including one RCLED, and three VCSELs. Optical transmission data was collected to characterize the optical properties of three of the VCSELs using the setup described in section 3.4. The measured optical transmission data was compared with the data from the devices modeled in Matlab using the matrix technique described in section 2.2. Optical transmission data was taken at several points across the device wafers to examine the uniformity of the wafer thickness.

Electroluminescence (EL) measurements were taken for both the RCLED and VCSEL devices. The EL plots were analyzed to characterize the active regions of the devices. Plots of optical power versus drive current and voltage applied (LIV curves) were used to determine the threshold current of VCSEL devices. LIV measurements were taken over a range of temperatures for some VCSEL devices and the output of those devices was analyzed. Lastly, the effects of temperature on the threshold current, slope efficiency, and output power and wavelength of the devices were studied.

### 4.2 Optical Power Transmission Measurements

The optical power transmission was measured for three of the four VCSELs in order to characterize the optical cavities. The oxide DBR VCSEL (V19) was not studied because the top DBR requires oxidation of the low index layers to produce a GaAs/Al<sub>2</sub>O<sub>3</sub> DBR to achieve the proper low index of refraction in the DBR. However, the optical transmission of V17, NSC336 and DO177 samples was measured and analyzed to provide insight into the performance of these devices, and validate the mathematical model created to calculate optical transmittance of optical thin film structures.

Figure 4.1 shows the power transmittance of the VCSELs at the location closest to the center of the wafer. All the devices provided sufficient reflectivity, stop-band width, and were centered about the proper wavelength to support lasing from the quantum dot active region. Therefore, the cavity resonance wavelengths and DBR characteristics were well matched. VCSEL NSC336 had the largest stop-band by a small amount and was centered about the longest wavelength. This was not surprising since NSC336 had the largest number of layers and apparently the highest index contrast between high and low DBR layers. All the devices had similar optical characteristics despite the differences in the structure and layer interfaces.

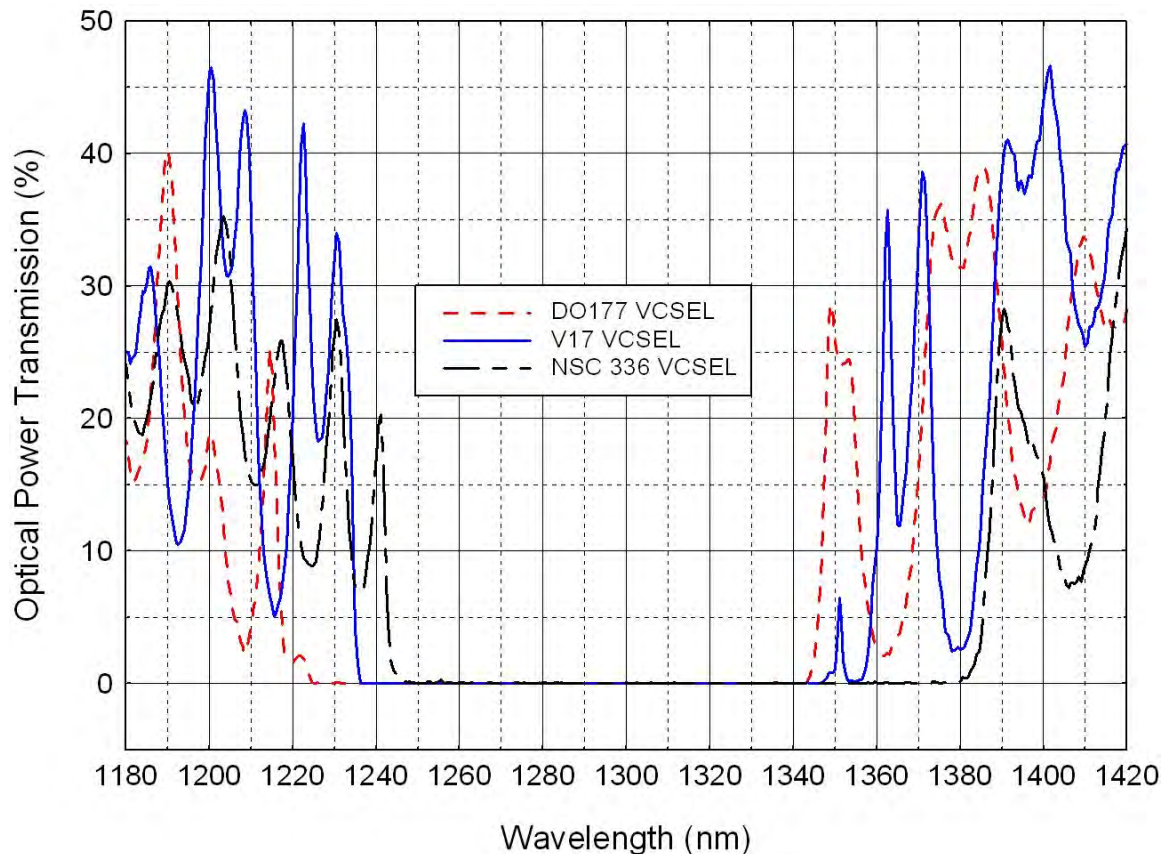


Figure 4.1: Optical Power Transmission Measured for Various Samples Studied

The V17 VCSEL model results are shown in Figure 4.2. Using the nominal values for layer thicknesses and an index of refraction routine [41], the model results matched the measured values the best out of the three devices. This could be because V17 used ungraded and non-conductive DBR layers. The model didn't account for the DBR layer grading in the other two VCSEL devices, and thus provided only an approximation for VCSELs NSC336 and DO177. This resulted in more adjustments in the models for the graded VCSEL devices to match the real measurements as shown in Figures 4.3 and 4.4.

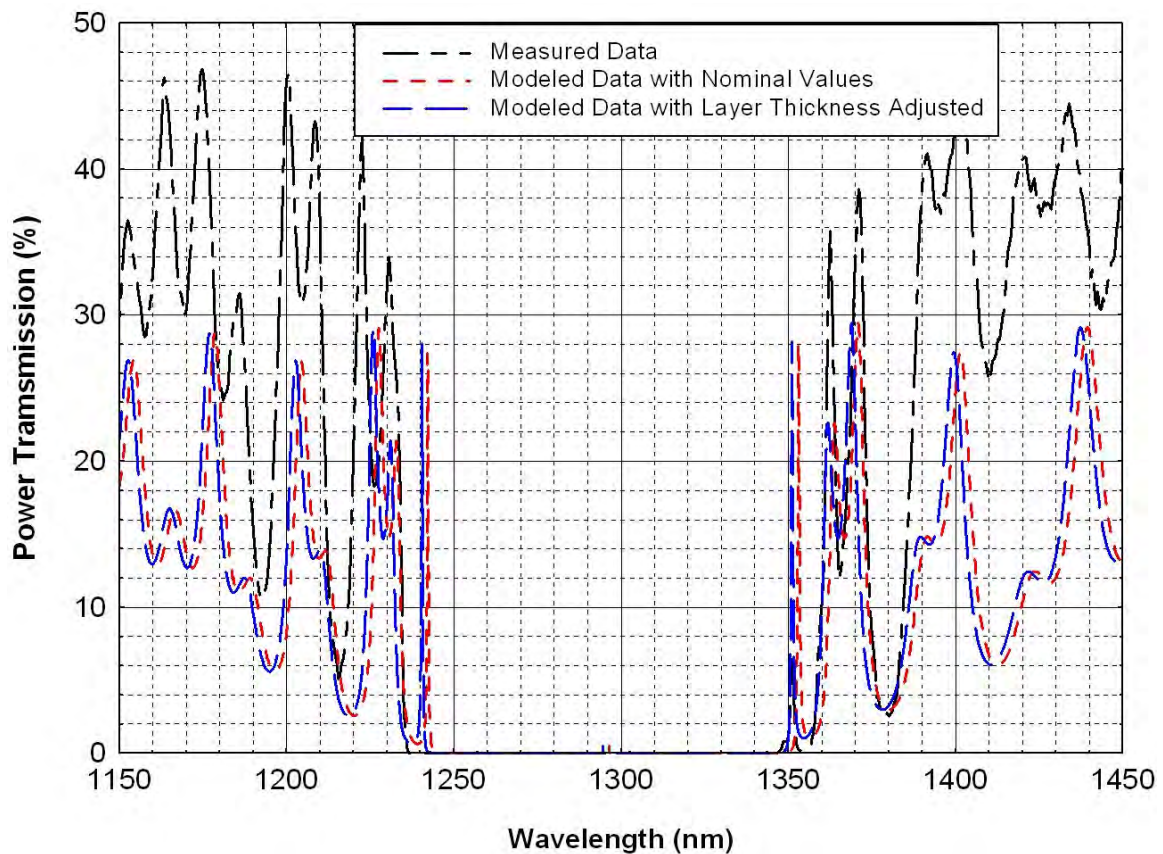


Figure 4.2: Measured power transmission of VCSEL V17 compared to modeled data with nominal values and adjusted values (reduced by a factor of 0.9985) for the layer thicknesses

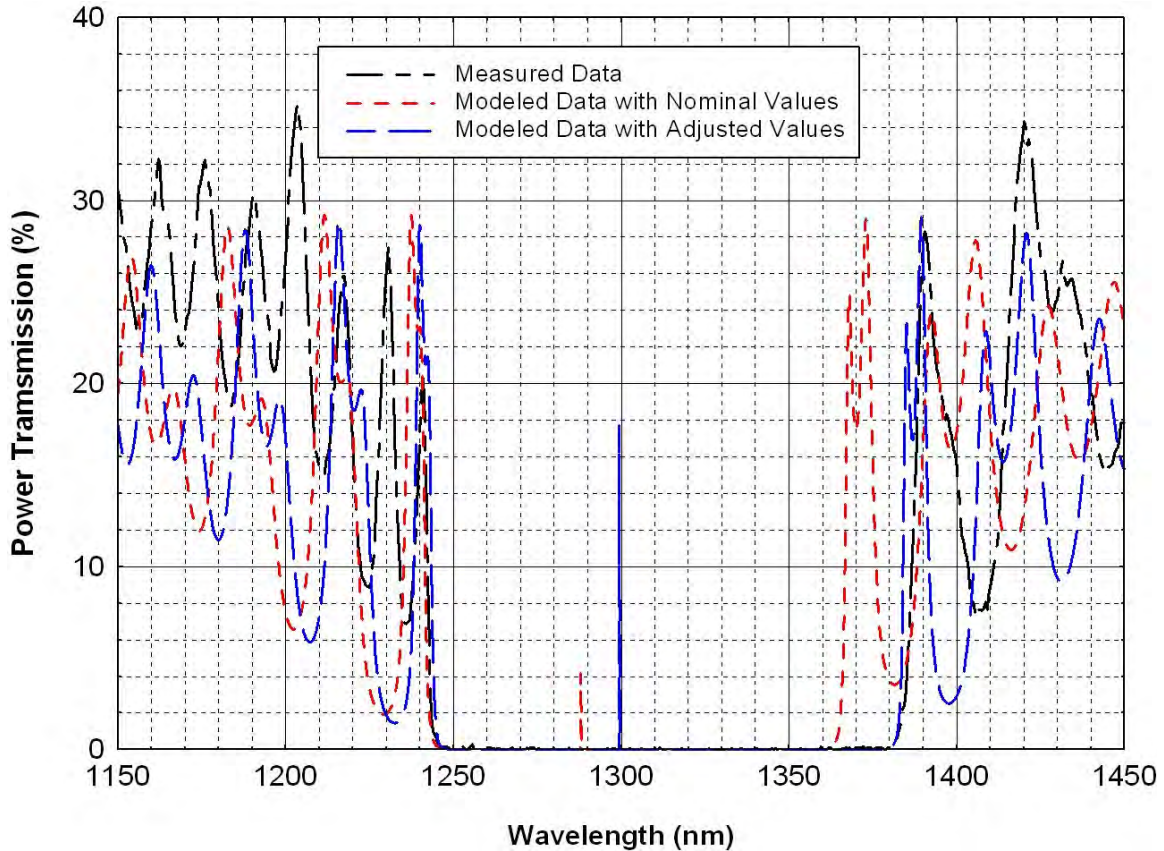


Figure 4.3: Measured power transmission of VCSEL NSC336 compared to the modeled data

The Fabry-Perot dip of the micro-cavities could not be measured with the setup used most likely because it lacked the required resolution. However, the model produces the resonant dip in reflectance shown in Figures 4.2 to 4.4, and the modeled values match well with the lasing/luminescence output of the devices.

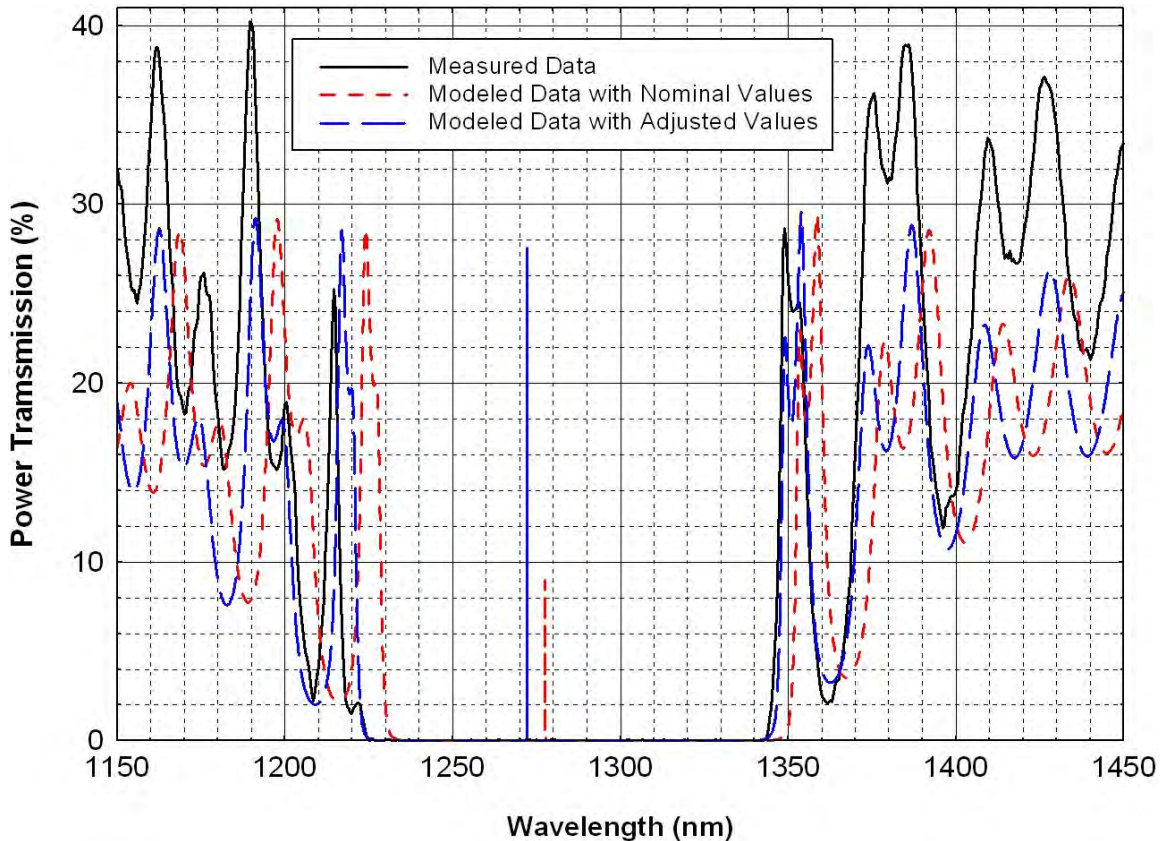


Figure 4.4: Measured power transmission of VCSEL DO177 compare to the modeled data

Optical transmission data was taken across at points across the sample wafers to examine the uniformity of the epitaxial layers. Figure 4.5 shows the optical transmission of sample V17 at three points from wafer center to the edge of the wafer. There is a definite red shift of the transmission of the sample from wafer edge to center of about 1.5 to 1.75 nm. This suggests the thicknesses of the epitaxial layers are within a range of 0.1%, based on manipulations required to get the Matlab model to shift 1.2 nm and assuming all the layers were equally thicker. A change of 1% in the thickness of all the layers of the V17 model caused a shift of 3.8 nm. A layer thickness grading is typical of wafers grown in MBE systems since there is a single source of atoms located unequal distance from one edge to the other wafer edge. Even with rotational stages in some

MBE systems a degree of variability can exist. Sample NSC336 averaged 2.71 nm/mm wavelength shift per distance across the wafer. While DO177 shifted 6.58 nm over a distance of 40 mm or had a change of only 0.165 nm/mm displaying much better uniformity.

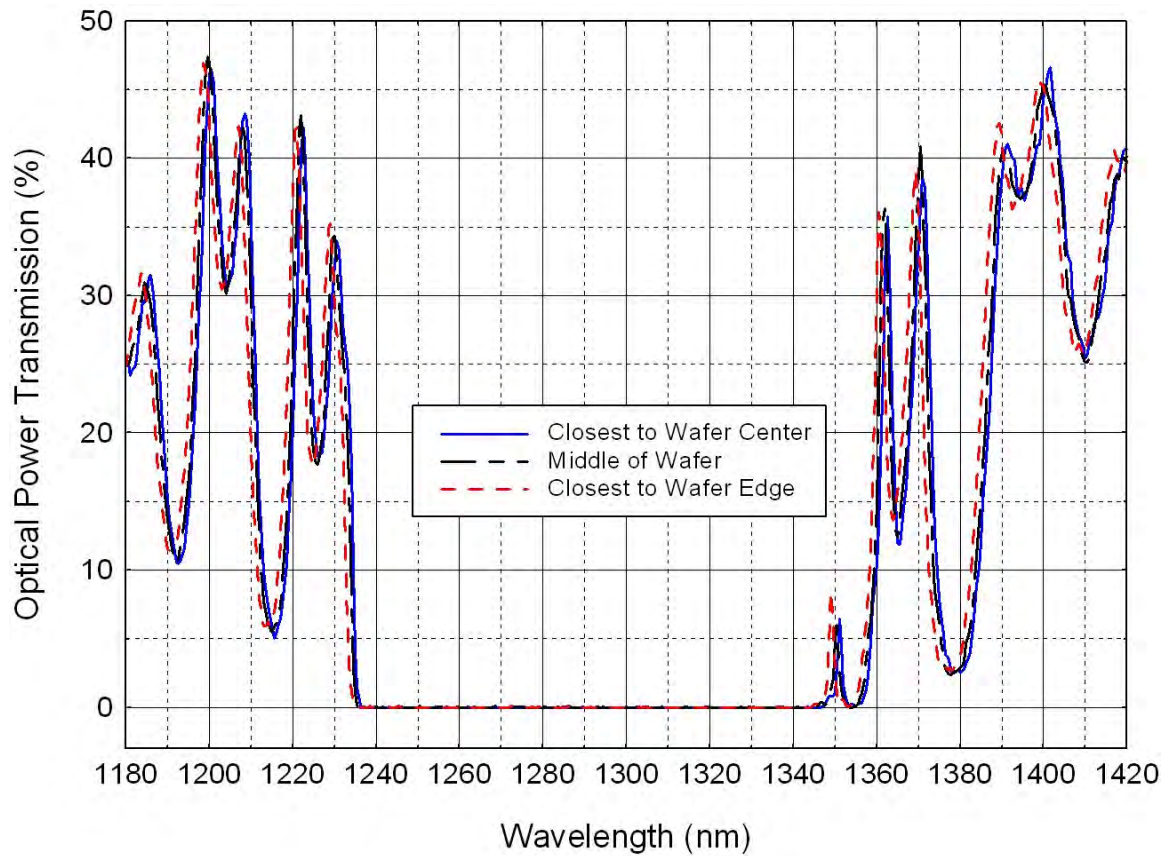


Figure 4.5: Measured power transmission of VCSEL V17 at points across a section of the wafer

Figure 4.6 shows the results of the transmission measurements on sample wafer NSC336. Optical transmission was measured at four points on the sample. The measurements produced very similar plots with an apparently linear shift in the plot as the

measurement point was moved out towards the wafer edge from the initial point (Point A). The VCSEL DO177 sample displayed very similar results as well as seen in Figure 4.7. The plots at each point are very similar, but blue shifted as the transmission measurement was taken closer to the wafer edge.

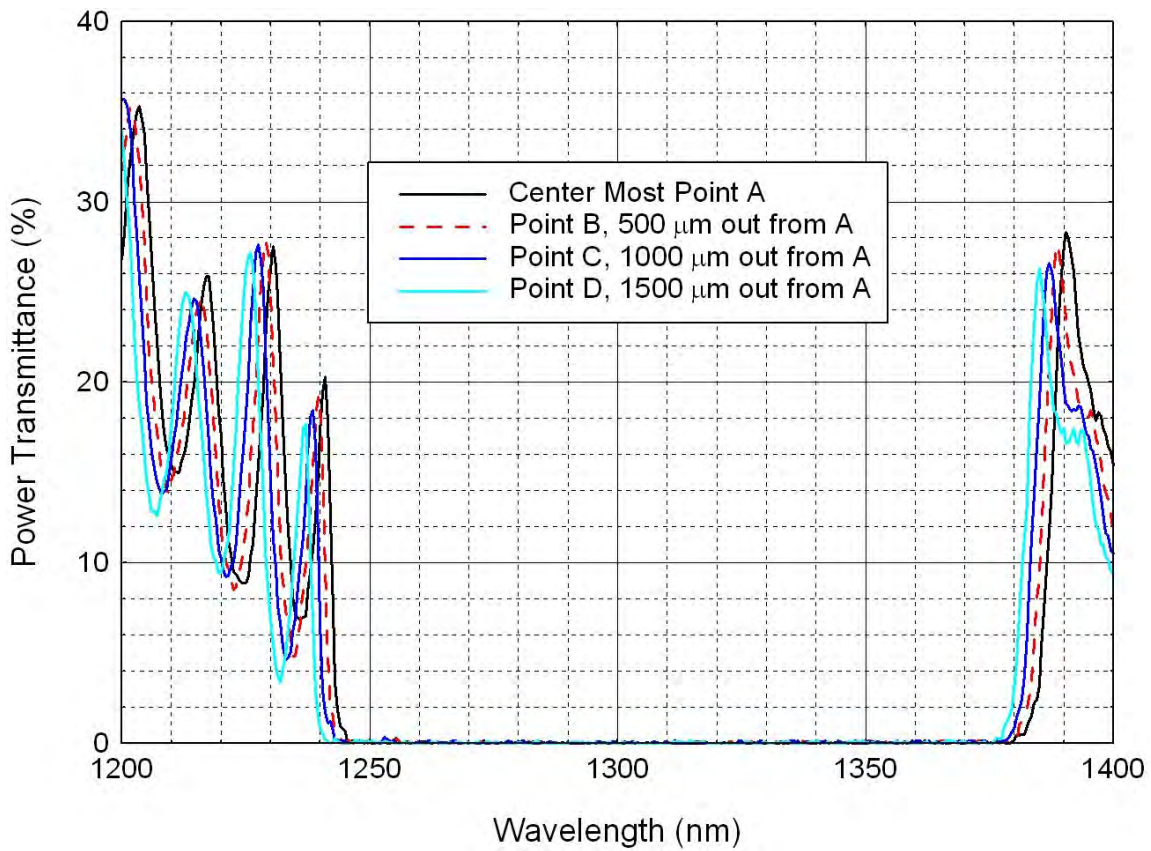


Figure 4.6: Measured power transmission of VCSEL NSC336 at four points across the wafer surface



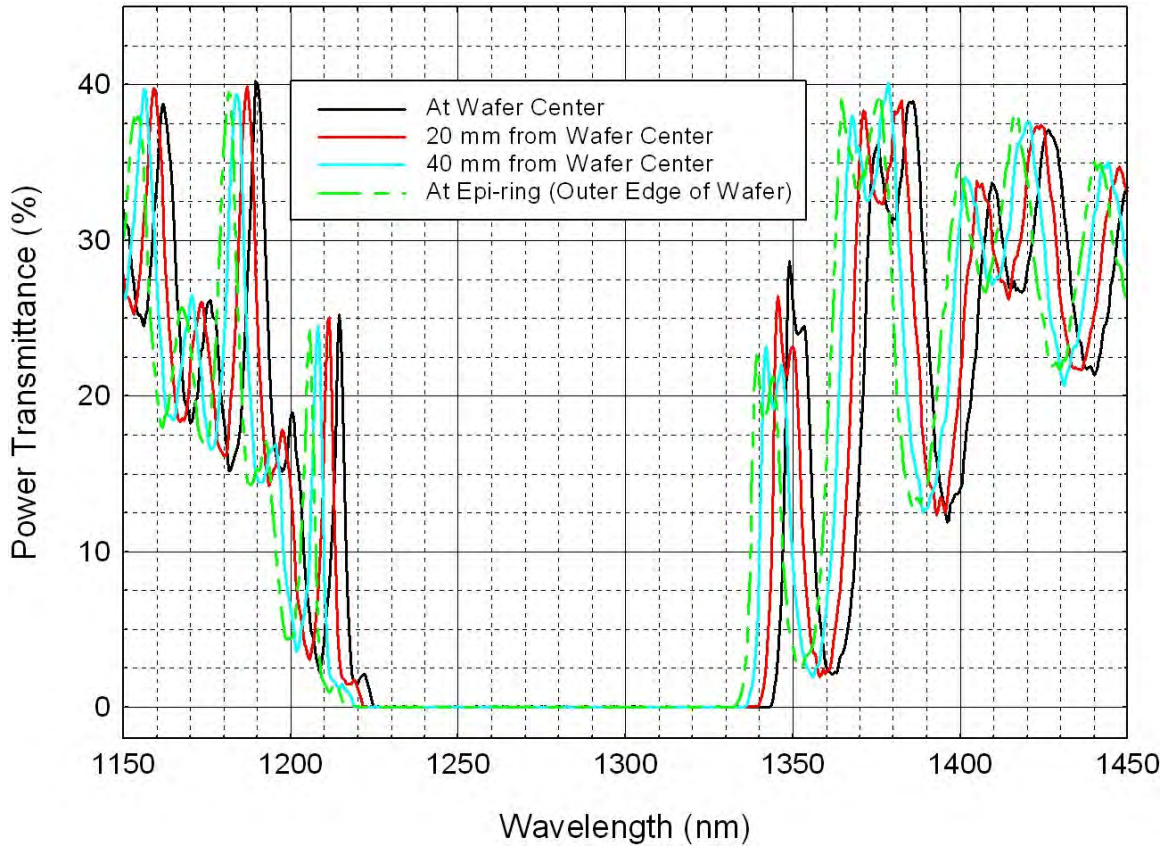


Figure 4.7: Measured power transmission of VCSEL DO177 at various points on the wafer showing the variability in layer thickness

### 4.3 Electroluminescence of RCLEDs and VCSELs

The electroluminescence of RCLED sample SH118, and VCSEL samples V17 and NSC336 was recorded over various drive currents. Peaks in the EL spectrum representing the QD ground state and excited state transitions were analyzed over various current levels, and the effect of selectively oxidized current apertures was examined.

Figure 4.8 shows the EL spectrum of an RCLED (SH118) with a mesa diameter of 50  $\mu\text{m}$  over a range of current levels. At lower current levels the gain peak of the ground state transition is 0.9671 eV (1282 nm) with an excited state transition peak at an energy of 1.028 eV (1206 nm). The energy difference between the GS peak and ES peak is 60.9

meV, more than twice the thermal noise level at room temperature (26 meV). It is desirable to have the largest energy gap possibly between the GS and first ES to suppress the excitation of carriers from the GS to ES energy levels.

The full width at half maximum of a 50  $\mu\text{m}$  diameter SH118 RCLED was measured over a range of drive currents. The results are shown in Figure 4.9, along with the photon energy levels at the upper and lower half maximums. The two extremes were recorded to gain insight into the changes in the carrier distribution as the current is increased.

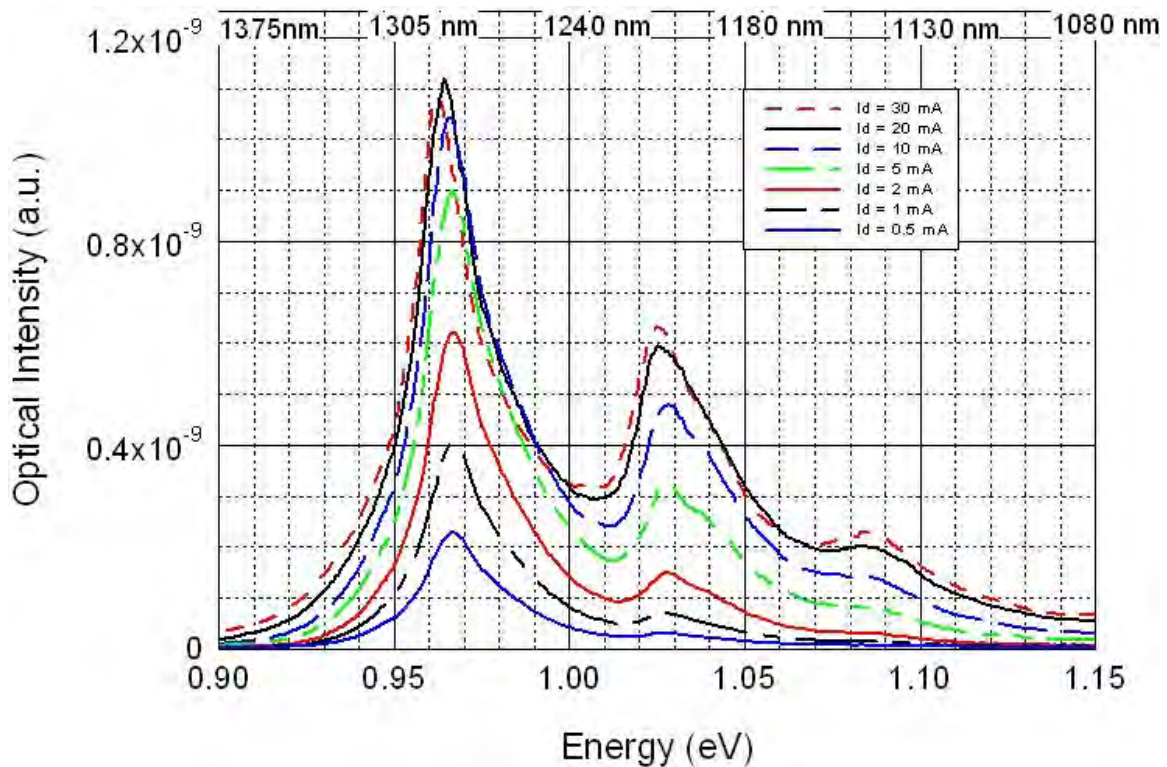


Figure 4.8: Electroluminescence of a 50um RCLED (SH118) versus drive current showing the rise of excited state transitions and red shift as the current increases

The FWHM increases as current increases as more carriers populate the QD energy states. The FWHM increases up to a point likely because the QD states become filled, photon absorption decreases and the device operates more efficiently with

increased current. However, after a certain point the current through the device causes enough heat to transition some of the carriers to higher QD energy states reducing the output of the ground state (GS) transition EL and increasing the excited state (ES) EL. This causes the EL level on the high energy end of the FWHM to decrease while the larger dots on the low end become saturated (the level remains the same) as can be seen between current levels of 20 and 30 mA in Figure 4.8.

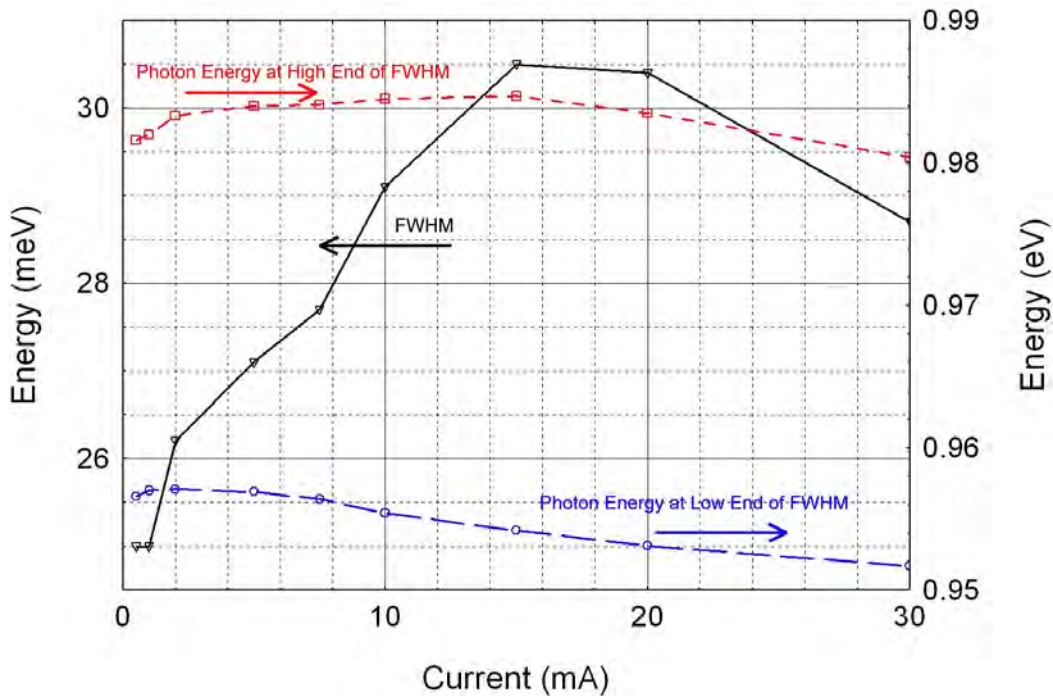


Figure 4.9: FWHM of the EL spectrum versus current of a 50um RCLED (SH118) at room temperature and the photon energy at the low and high ends of the FWHM versus drive current

Larger QDs with additional higher allowed energy states will eventually lose carriers to thermal excitation into the higher energy states and the output of the GS transition will eventually sharply decrease as current increases and continues to heat the device as can be seen in the smaller device in Figure 4.10. A larger red shift occurs as the band gap shrinks with increased temperature, and the EL output level is reduced by

thermal losses at a current level of 30 mA in the 50  $\mu\text{m}$  diameter device. The 17  $\mu\text{m}$  diameter device in Figure 4.10 has a much larger current density per input current, so the active region heats up at much lower current levels. The 17  $\mu\text{m}$  device shows signs of excessive heat at about 5 mA as the EL peak red shifts noticeably from the EL at lower current levels. As the current is increased beyond 5 mA, the device output drops gradually (relative to the increase versus current) until the output at 30 mA is actually less than the output at 1 mA.

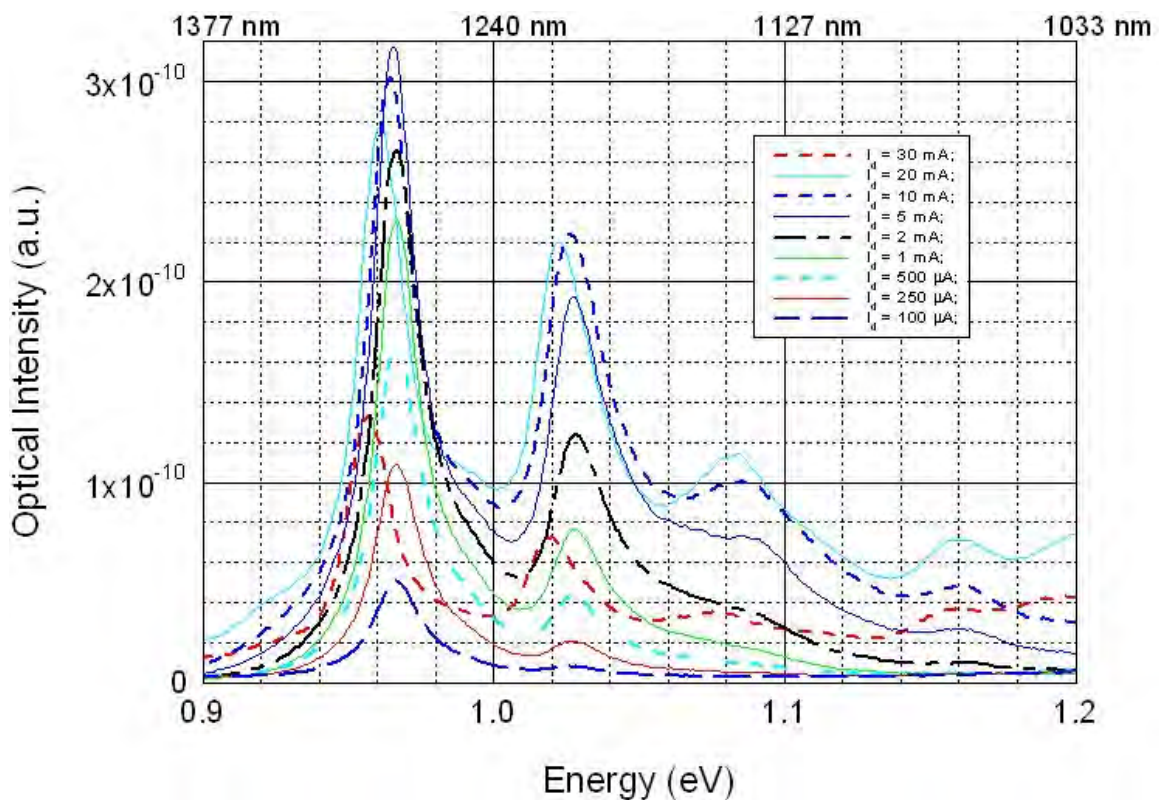


Figure 4.10: Electroluminescence of a 17 $\mu\text{m}$  RCLED (SH118) at various drive currents showing the rise of excited state transitions and red shift as the current increases

The oxidation of V17 was hindered by the excess metal covering the devices after attempting to do a metal lift off. Even so, the oxidation appears to have had a dramatic effect on the output of the device for a given current level. Although the optical

confinement doesn't appear to have improved, the light output level has jumped dramatically by a factor of nearly 4. The device appears to be much cooler as well since there is no red shift between the 5 mA outputs of the device when unoxidized and oxidized despite the increase in current density since the current aperture is smaller.

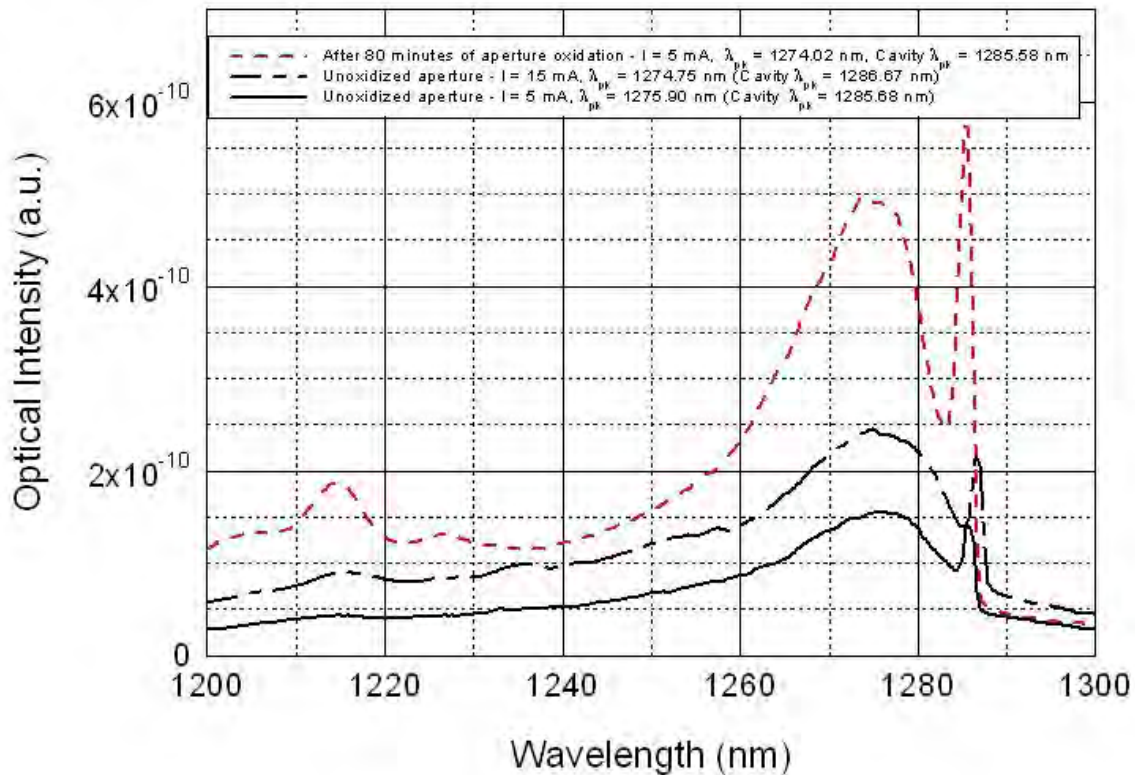


Figure 4.11: Output of a 25  $\mu\text{m}$  V17 VCSEL prior to oxidation of the oxide aperture at drive currents of 5 mA and 15 mA, and after 80 minutes of oxidation at a current of 5 mA

The VCSEL sample V17 fabricated with an AFRL mask set was oxidize four times for 20 minutes at a time (80 minutes total). The continuity of smaller devices was checked after each oxidation in an attempt to determine the depth of the oxidation. However, the oxide aperture layer ended up being unevenly oxidized and after the initial twenty minutes the oxide depth had very little change. This is probably due to the excess metal blocking the absorption of oxygen in the oxide layer, and because of the diffusion

time required for the oxygen to travel through the existing oxide. In most devices, the oxide layer could be seen through the devices as slightly lighter shaded area, so the depth could be determined visually and characterizing the rate of oxidation was not critical to fabricating other devices.

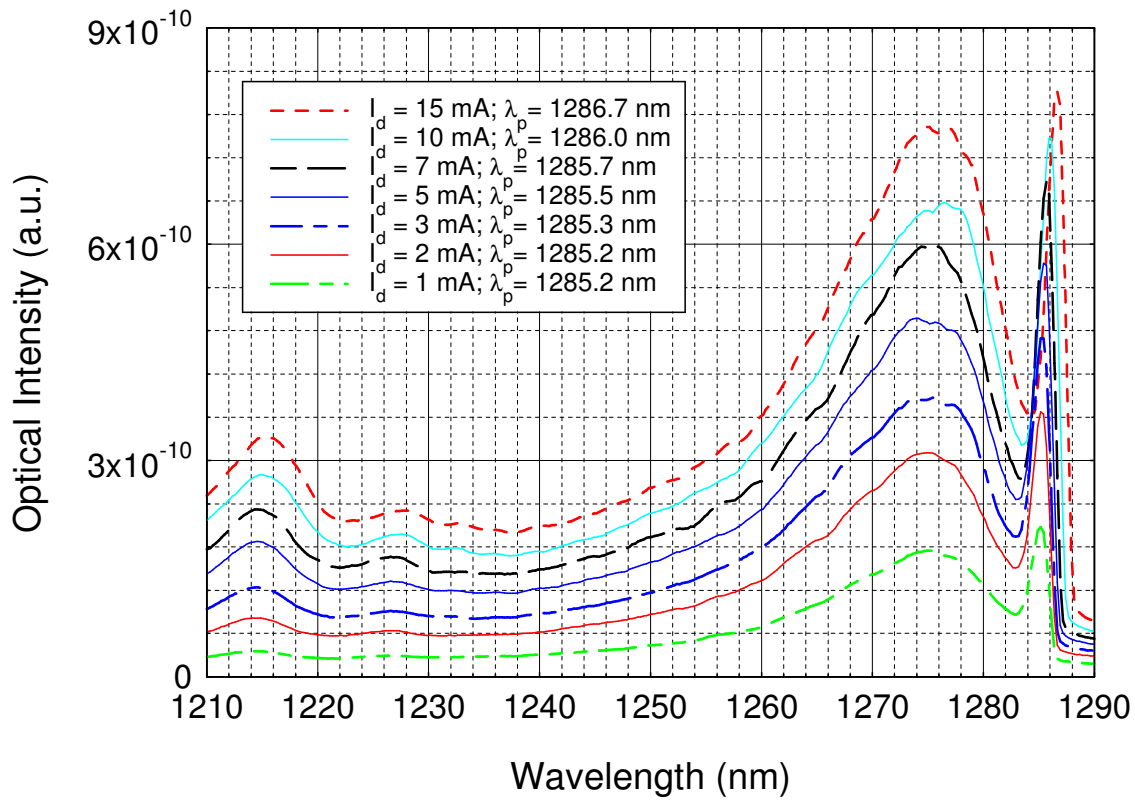


Figure 4.12: EL of VCSEL V17 with a 25  $\mu\text{m}$  diameter versus drive current

The electroluminescence of V17 was observed over a range of current levels at ambient temperature as shown in figure 4.12. The device doesn't appear to have very good optical confinement since the OSA picked up a large portion of the EL from the full gain curve that should not pass through the stop band of the cavity (1235nm to 1350 nm as seen in Figure 4.5). In addition to this, after 7 mA current internal heating of the active region creates a distinct red shift in the resonance of the VCSEL cavity of about 1 nm

between 7mA and 15 mA. The resolution (1nm) of the OSA in these scans is too low to show it, but lateral cavity modes also appear to be present and increase as the current increases since the resonant peak output broadens as current increases.

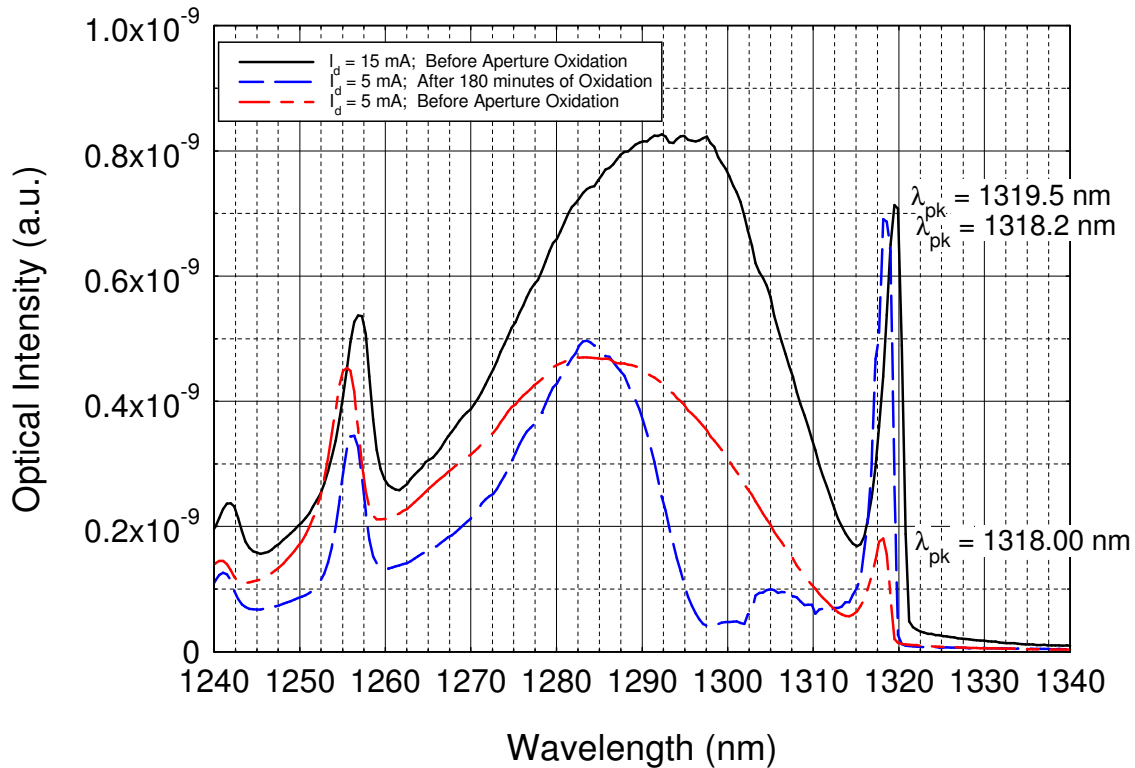


Figure 4.13: Output of a square shaped VCSEL NSC336 with a diameter of 35  $\mu\text{m}$  prior to oxidation of the oxide aperture at drive currents of 5 mA and 15 mA, and after oxidation at 5 mA

VCSEL devices were fabricated from sample NSC336 using the mask developed in this study, and oxidized for a total of 180 minutes in an attempt to close off some of the smaller devices and characterize the depth of oxidation versus time. However, these devices also seemed to have an oxide depth limit, and it appears only the 5  $\mu\text{m}$  devices lost all continuity. Still, the optical confinement of the NSC-336 device in Figure 4.13 is clearly better than the V17 device in Figure 4.12. The NSC-336 sample is a top DBR contacted VCSEL, and didn't have an issue with lifting off the metal contact layer. Thus,

the NSC336 VCSELs had more uniform oxide layers that appeared to be about 8 to 10  $\mu\text{m}$  thick.

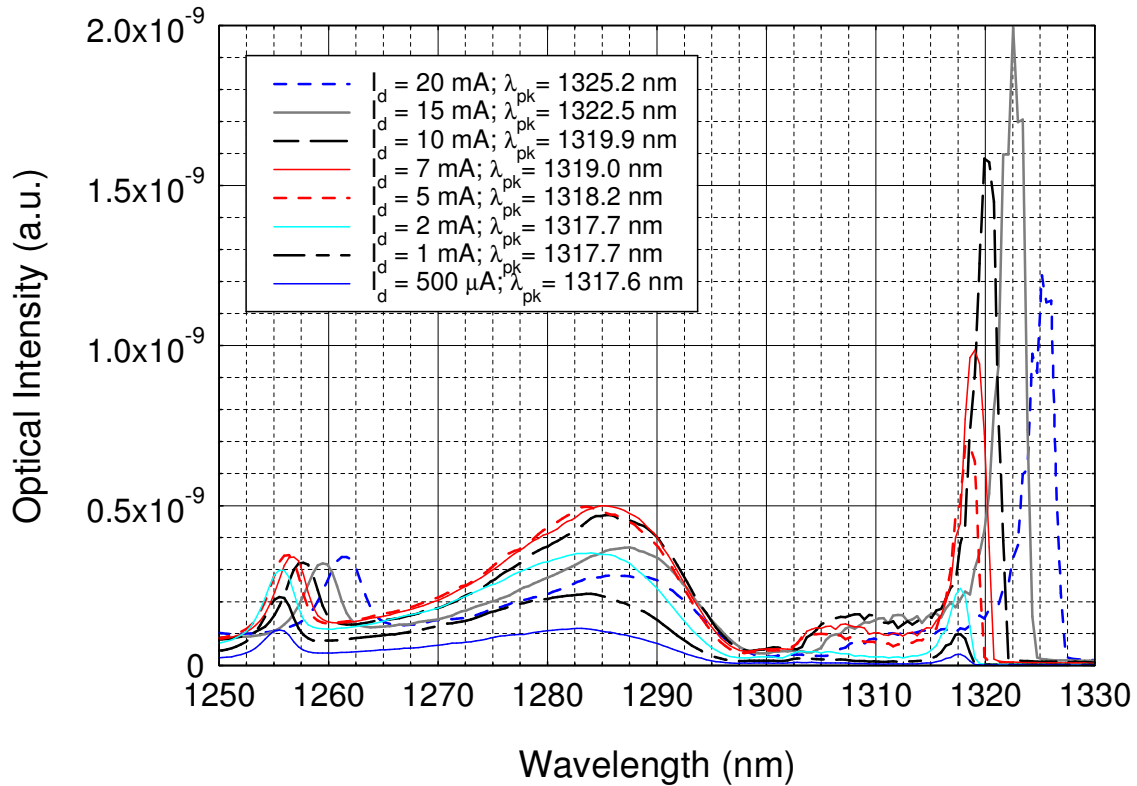


Figure 4.14: EL output of a square shaped NSC336 VCSEL versus drive current

The oxide layer clearly improved the output of the NSC336 device and EL before and after oxidation is shown in Figure 4.13. The EL in the stop band of the device is reduced significantly, but not completely as some light escaped out the side of the device mesa. Lateral modes are easily seen in the EL of the square NSC 336 device especially as the current is increased. The square shape of the VCSEL, and the irregular current distribution caused by the uneven oxide layer may have contributed to the increase in lateral modes. A higher resolution OSA (0.1 nm resolution bandwidth) scan was performed to capture more information on the cavity modes of the square NSC336 VCSEL and the Low and high resolution EL is shown in Figure 4.15. The primary lateral



modes are separated by about 0.6 nm while some of the higher order modes are separated by about 0.3 nm. These higher order modes also showed up in other devices and affected the lasing output as well. Lateral modes of the VCSELs were not intended to be studied, but from the limited number of high resolution measurements it appeared as though lateral modes were more significant in the square shaped VCSELs than the circular.

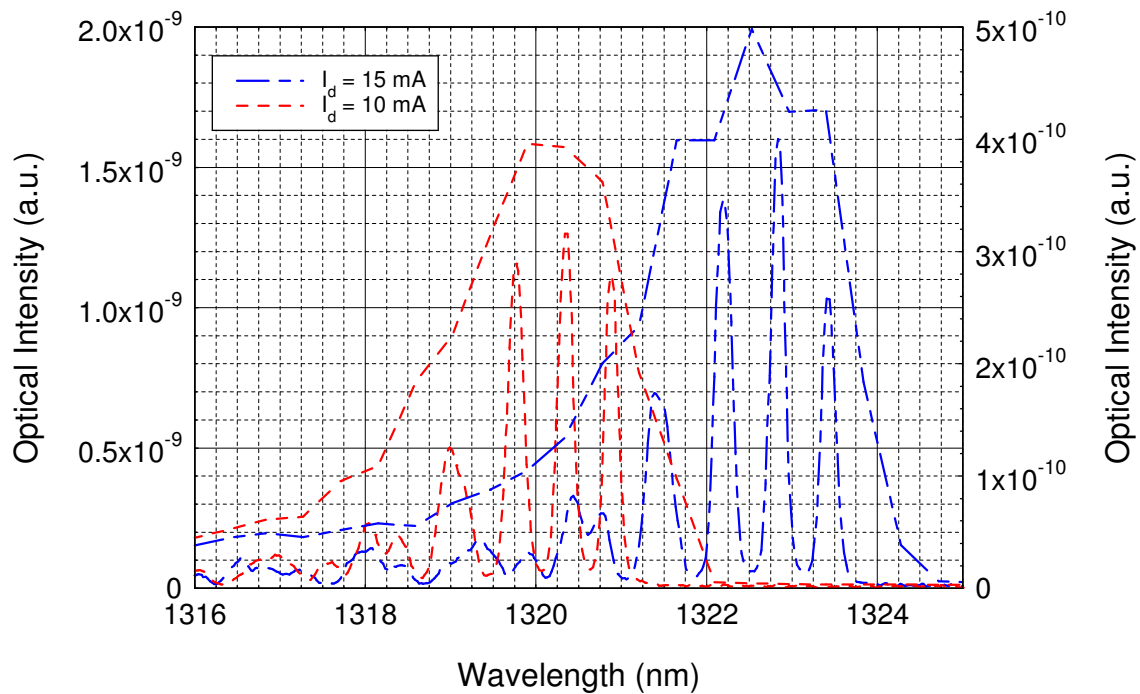


Figure 4.15: Output of a 35  $\mu\text{m}$  VCSEL NSC336 measured with an optical spectrum analyzer at 0.1 nm resolution to measure the lateral modes of the cavity compared with the output measured with 1 nm bandwidth resolution

#### 4.4 Temperature Effects on Electroluminescence of RCLEDs and VCSELs

The output of a circular 50  $\mu\text{m}$  SH118 RCLED with a 5 mA drive current was measured over various chuck temperatures from 15°C to 60°C, and is shown in Figure 4.16. The variation in chuck temperature had a profound effect on the output amplitude and slightly red-shifted the peak of the EL output of the device as the Temperature was increased. Both the GS and ES transitions were similarly affected in relative amplitude

and peak wavelength. The change in amplitude first appears to be skewed toward the higher energy QDs, but the shape of the EL curves remained proportionate. This suggests that the outputs of all the various sized QDs are being reduced evenly, but the whole ensemble is also being red-shifted with an increase in chuck temperature. Thus, the lower energy level side of the EL graphs appears to have little change in amplitude which would suggest that maybe carriers are being thermally lost to higher energy states. However, that is not likely at the temperatures and currently levels measured. It's more likely that the losses related to the heat reduce the output amplitude, and that the band gap reduction related to increases in temperature shifts the energy levels of the whole ensemble of QDs as a separate effect. Thermally excited carriers moving into higher QD energy states and/or the wetting layer of the QDs is probably minimal considering the 62 meV separation between the GS and ES of the QD ensemble.

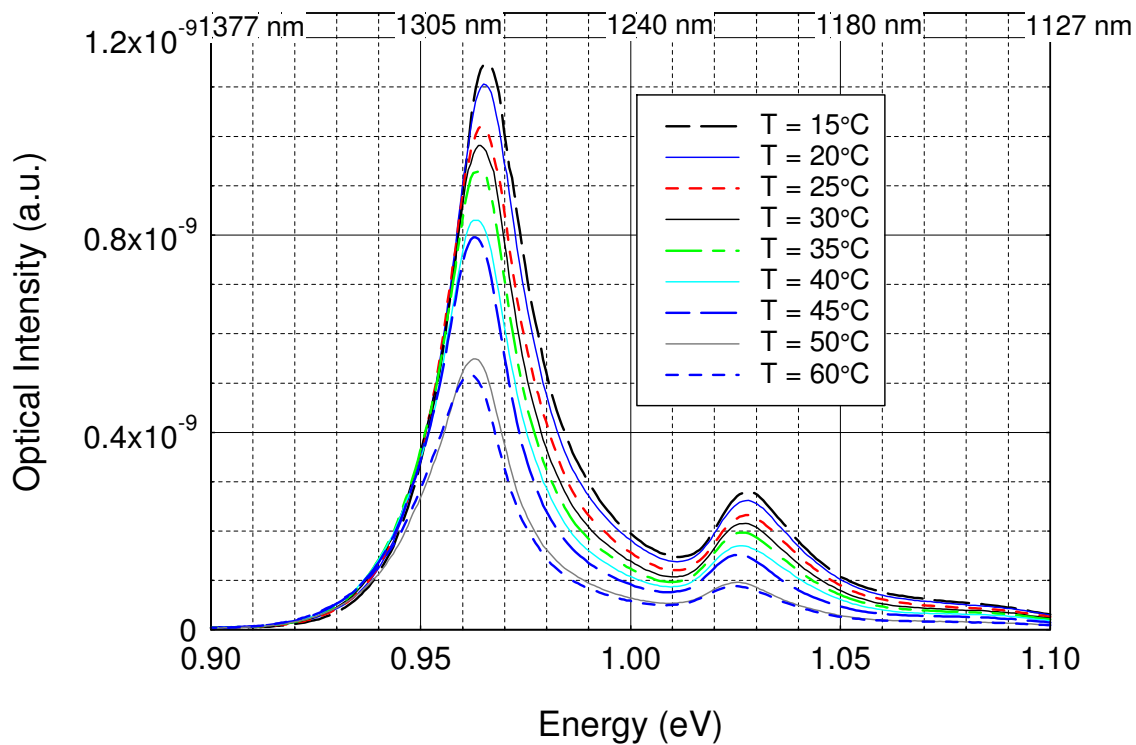


Figure 4.16: Output of a SH118 RCLED at various chuck temperatures

Figure 4.17 shows the shift in the peak energy level of the GS and ES transition of the QD active region linearly curve fit to extract an average slope to characterize the effect chuck temperature has on shifting the energy levels of the GS and ES. The GS changed at a rate of  $-82 \mu\text{eV}/^\circ\text{C}$ , while the ES changed at a rate of  $-72 \mu\text{eV}/^\circ\text{C}$ . This was most likely the result of band gap reduction with increase temperature. The change in the band gap of GaAs and InAs will affect the energy levels of the QDs, since they are based on the material band gap as well as the physical characteristics of the QDs. The physical characteristics define the discrete energy levels in QD, but the level of that discrete energy is still based on the material band gaps. The band gap of GaAs changes at a rate of  $-490 \mu\text{eV}/^\circ\text{C}$  [42]. Much less than the changes seen here, however, this can be explained because the temperature of the active region is not equal to the chuck temperature, and is a function of thermal resistance of the device and the power in the active region (current and voltage). Modeling the actual temperature of the active region was not investigated in this study.

The full width at half maximum (FWHM) of the GS EL output in Figure 4.16 was measured for the various temperatures as shown in Figure 4.17. The upper and lower values at the half maximum were also included to attempt to gain insight into how the QD ensemble shifts with temperature (i.e are the higher energy level QDs affected differently then the lower energy dots?). However, from examination of Figures 4.17 and 4.18, it appears the FWHM merely increases or decreases with the increase or decrease in the output amplitude of the QD ensemble. At higher temperatures, the EL output curve decreases and flattens out thus broadening the FWHM (in this case at  $T > 50^\circ\text{C}$ ).

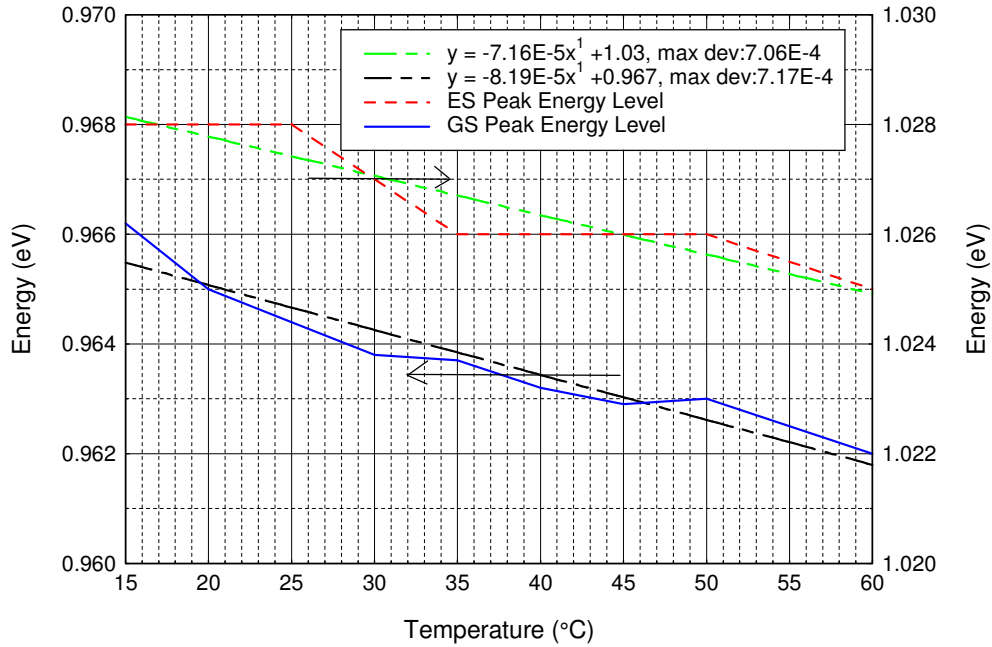


Figure 4.17: Peak energy levels of the ground state (GS) and excited state (ES) of the QD active region of a 50 μm RCLED (SH118) versus chuck temperature

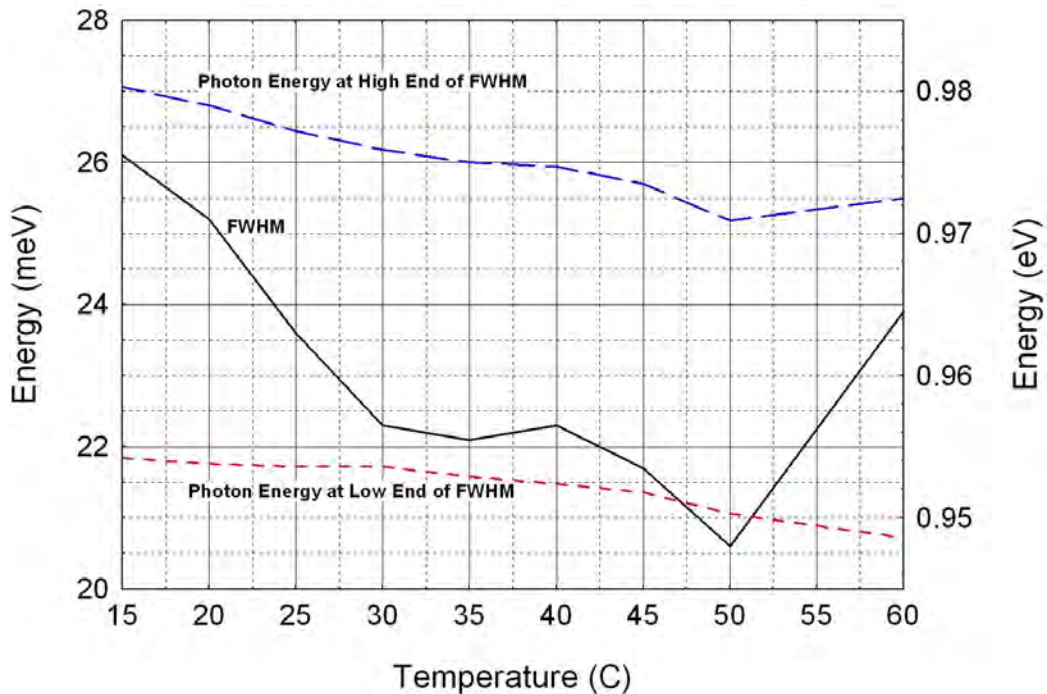


Figure 4.18: FWHM of the QD active region of a 50 μm diameter RCLED (SH118) in meV and the high and low end points at half maximum versus the device chuck temperature

The cavity output of V17 was examined over a range of chuck temperatures to see the affect of temperature on the VCSEL cavity resonance. The expectation was that the cavity material would expand with increased temperature and the resonance would red-shift to longer wavelengths, but at a rate lower than that of the QD ensemble output (as reported in previous literature).

Figure 4.19 shows the cavity output of a 20  $\mu\text{m}$  V17 VCSEL form 0°C to 50°C. V17 has the same active region and bottom DBR as the SH118 RCLED, so the cavity resonance of V17 versus chuck temperature is compared to the peak output of the SH118

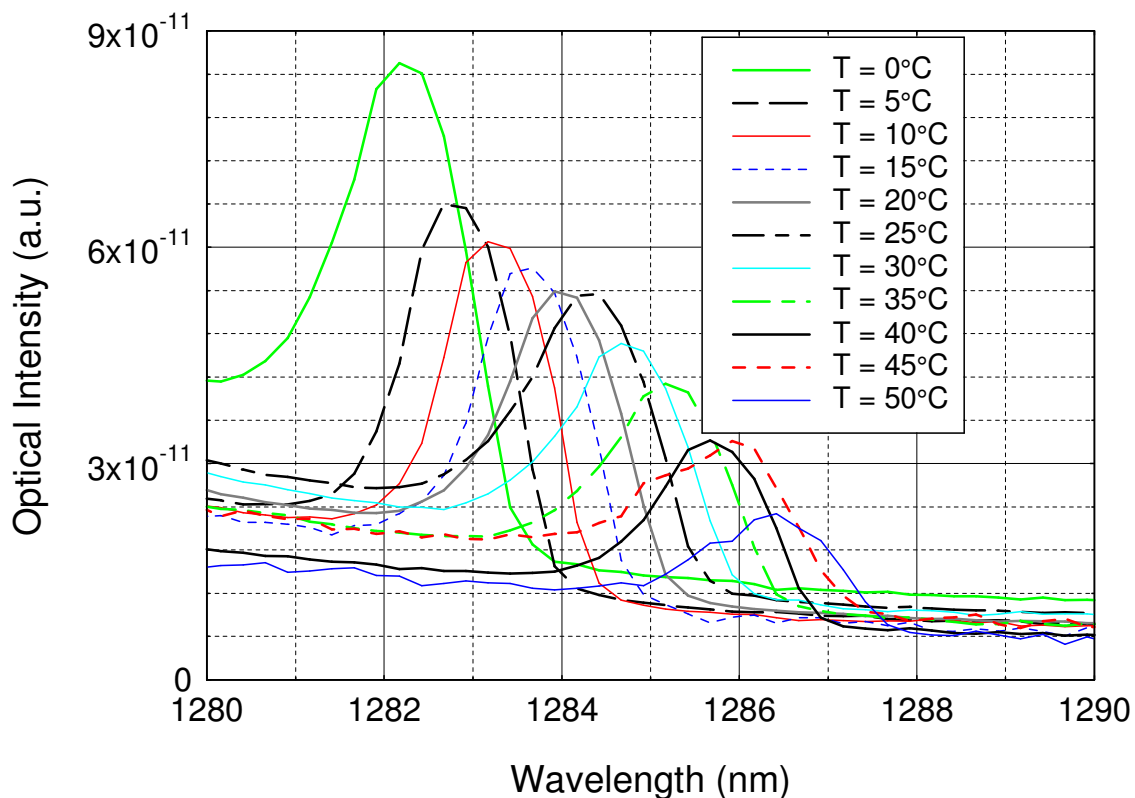


Figure 4.19: Effect of temperature on the cavity resonant peak of circular VCSEL (V17) with a diameter of 20  $\mu\text{m}$  ( $6\lambda$  cavity)

EL versus chuck temperature in Figure 4.20. Using the chuck temperature is not actually the material temperature in the active region, so the rates of change in Figure 4.20 are not actually material properties. They are more or less device properties and actually depend on the current density of each of the devices even though the devices have the same structure from the active region down. The SH118 sample had a current of 4 mA and was a 50 μm diameter device, while the V17 VCSEL was a 20 μm diameter device at a current of 1 mA. The current density of each device could not be calculated reliably because the exact oxide aperture size was unknown. Ideally the comparison in Figure 4.20 should also be made from measurements off the same wafer, however the V17 devices were fabricated on the AFRL mask which did not include RCLEDs, so there wasn't a single wafer with both working VCSELs and RCLEDs available for this study.

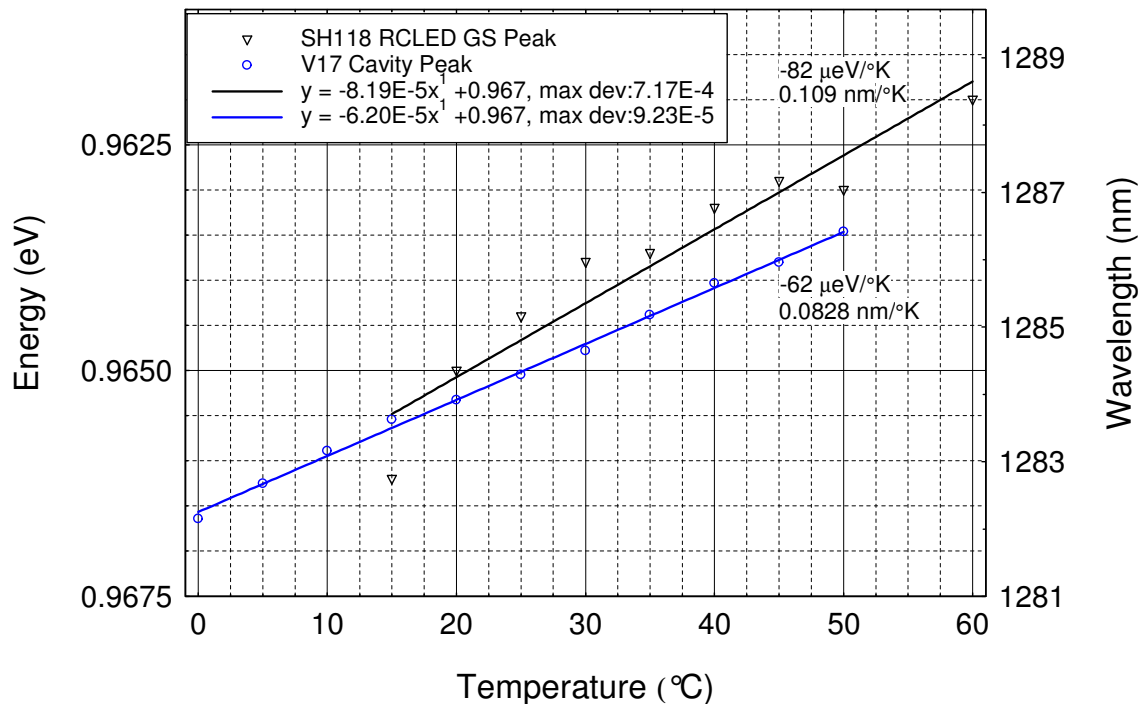


Figure 4.20: Shift in the gain curve and cavity resonant wavelength of VCSEL V17 verses the device chuck temperature

#### 4.5 Lasing and Cavity Characteristics of VCSELs

A through DBR contacted VCSEL sample, DO177, with a single oxide aperture and a  $2\lambda$  cavity was fabricated with a single mesa etch (no RCLEDs) using the mask set developed in this study (see chapter 3). The DO177 VCSELs were fabricated and oxidized once for 20 minutes at  $400^\circ\text{C}$  with 500 cfm of  $\text{H}_2\text{O}_{(\text{g})}$ . Electroluminescence and LIV data was collected at room temperature and a range of chuck temperatures. Lasing occurred at room temperature in some devices and many devices lased at lower chuck temperatures. Threshold current, slope efficiency, and wall plug efficiency were calculated. Lateral modes and spectral outputs were examined over a range of temperatures.

The oxidation of the DO177 VCSELs resulted in excellent current and optical confinement. An example is shown in Figure 4.21 with a  $15\ \mu\text{m}$  diameter square VCSEL

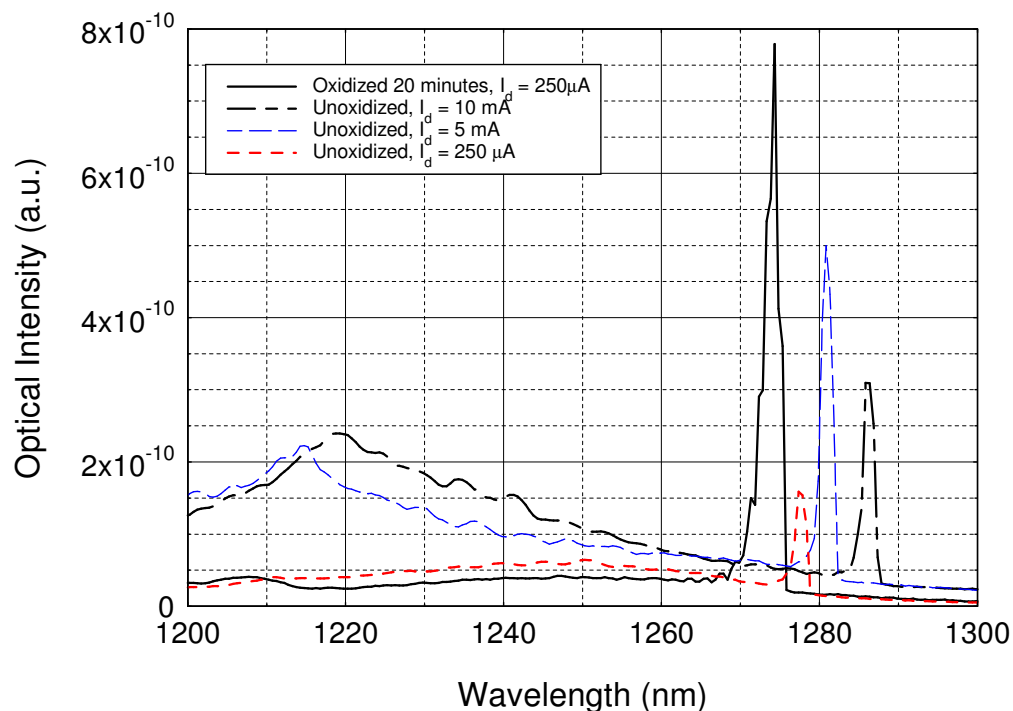


Figure 4.21: Output of a DO177 VCSEL at drive currents of  $250\ \mu\text{A}$ , 5 mA and 10 mA prior to oxidation and after oxidation of the oxide aperture output before

and after oxidation for 20 minutes. The output at 250  $\mu\text{A}$  is greater than the output of the unoxidized VCSEL's output at 10 mA current. At the same time, the output EL is very low across the stop band of the device at wavelengths other than the cavity resonance wavelengths. However, many undesired lateral modes are present as well.

The output of a 15  $\mu\text{m}$  diameter square VCSEL is shown in Figure 4.22 along with the measured power transmittance of the wafer at a point close to the VCSEL device. From Figure 4.22, it can be seen that at room temperature, the cavity resonance is largely positively detuned (by about 75 nm) from the EL (gain curve) peak which looks like it is at around 1200 nm. The EL emission peaks match well with the major peaks in cavity transmission.

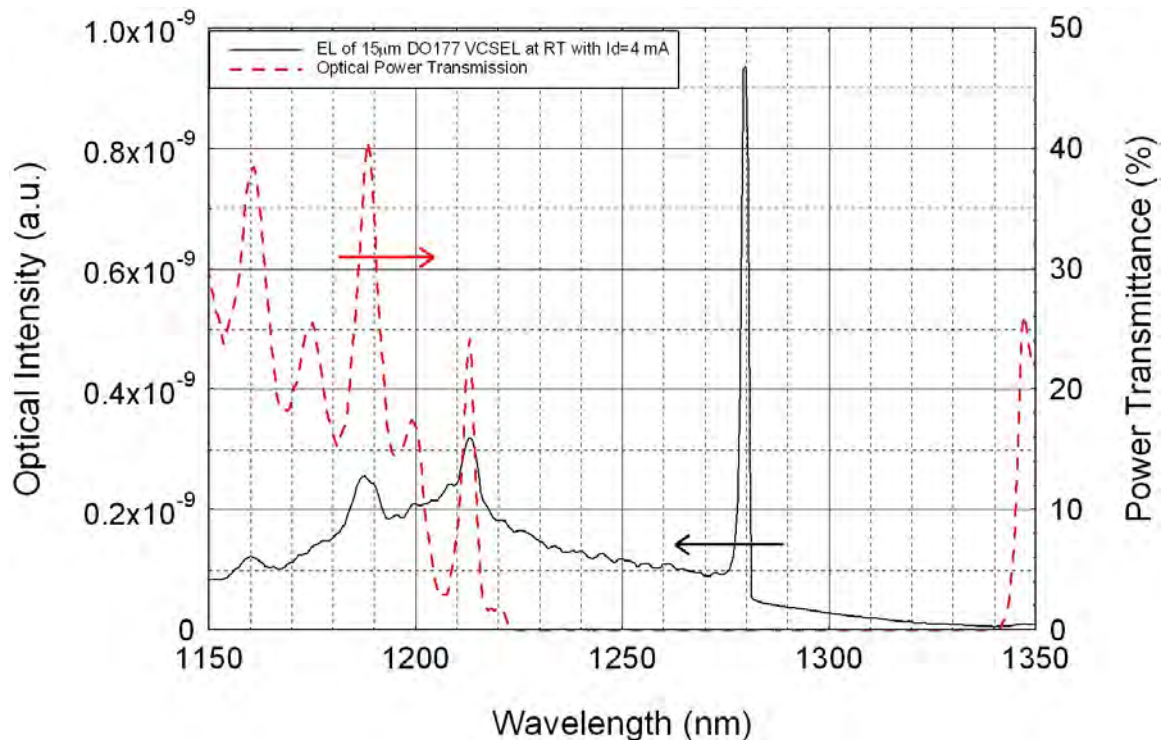


Figure 4.22: Output of a 15 $\mu\text{m}$  diameter DO177 VCSEL at 4 mA compared to the optical transmission of the wafer



The smaller VCSEL devices (10  $\mu\text{m}$  to 30  $\mu\text{m}$  diameter) usually have a more uniform current density and perform better than the larger diameter devices, so more focus was put on examining smaller DO177 devices. Figure 4.23 shows the output of a 15  $\mu\text{m}$  diameter circular VCSEL at room temperature. Three LIV curves are shown to show how erratic the output of this device was as it weakly produced lasing at and around a threshold current of about 1 mA. Some larger device were investigated, but none larger than 25  $\mu\text{m}$  in diameter displayed lasing for certain. Figure 4.24 shows the output of a 50  $\mu\text{m}$  diameter circular VCSEL that had some amount of resonance in it's output, but not likely to have gone into the realm of lasing. Oxidizing the 50  $\mu\text{m}$  device for a longer period of time may improve the output or possibly allow the device to produce lasing.

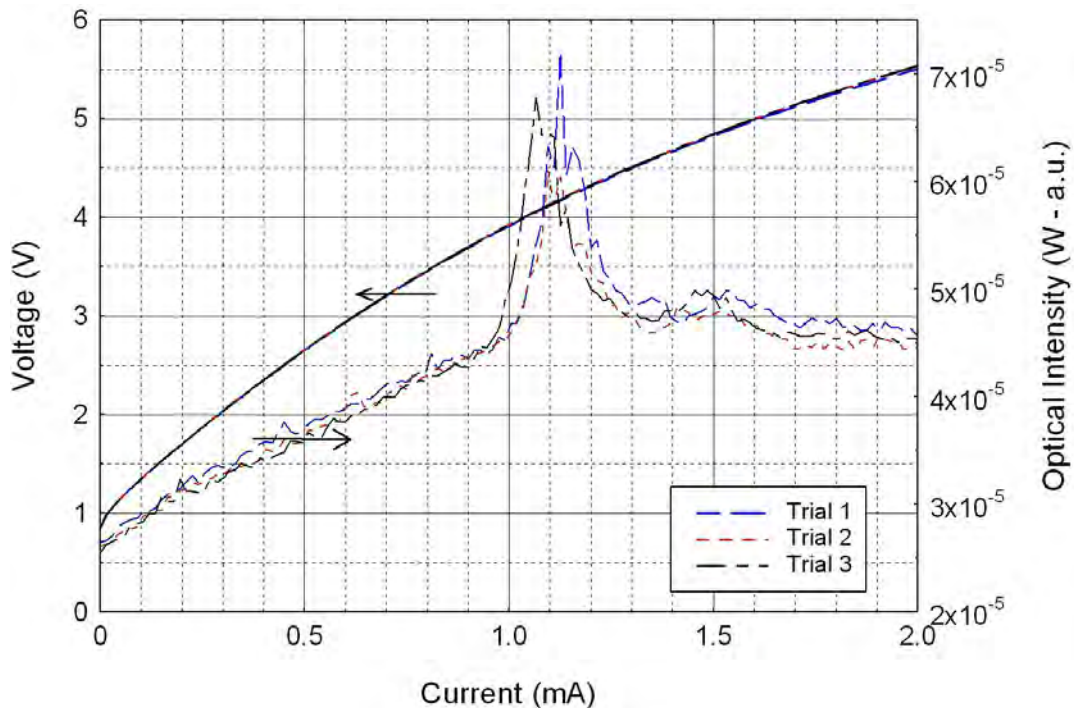


Figure 4.23: LIV curve of a 15 $\mu\text{m}$  DO177 VCSEL at room temperature showing very weak lasing activity

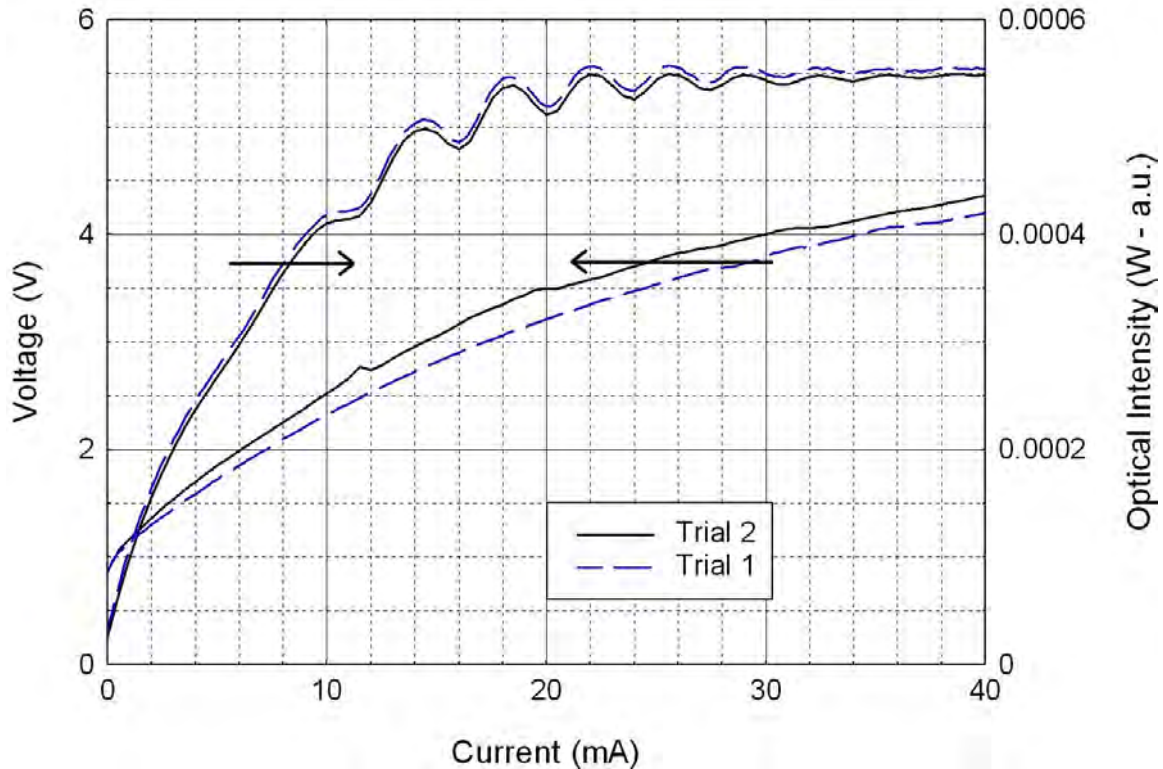


Figure 4.24: Output of a 50  $\mu\text{m}$  DO177 VCSEL after 20 minutes of oxidation of the oxide aperture

A circular DO177 VCSEL device with a diameter of 25  $\mu\text{m}$  proved to have the best performance of the devices tested. At a chuck temperature of 25°C, the device performed well enough to determine the threshold current. The threshold current at a chuck temperature of 25°C was 2.65 mA as shown in Figure 4.25. The device appears to be lasing only in a single mode given that the LIV has a single peak with a smooth slope. The slope efficiency was 3.88 W/A and is shown in Figure 4.26. The device had a maximum wall plug efficiency of 9.28% at a chuck temperature of 25°C at a current of about 2.83 mA. However, that is assuming that all the output power was captured and coupled to the photodetector and that the responsivity provided by the manufacturer for the InGaAs photodetector (0.693 W/A) is correct at 1.28  $\mu\text{m}$ . The apparatus, which

included the photodetector and an HP 4145B semiconductor parameter analyzer (SPA), was not calibrated, so I have no certainty that the output power levels, efficiency, or the slope efficiency values are absolute.

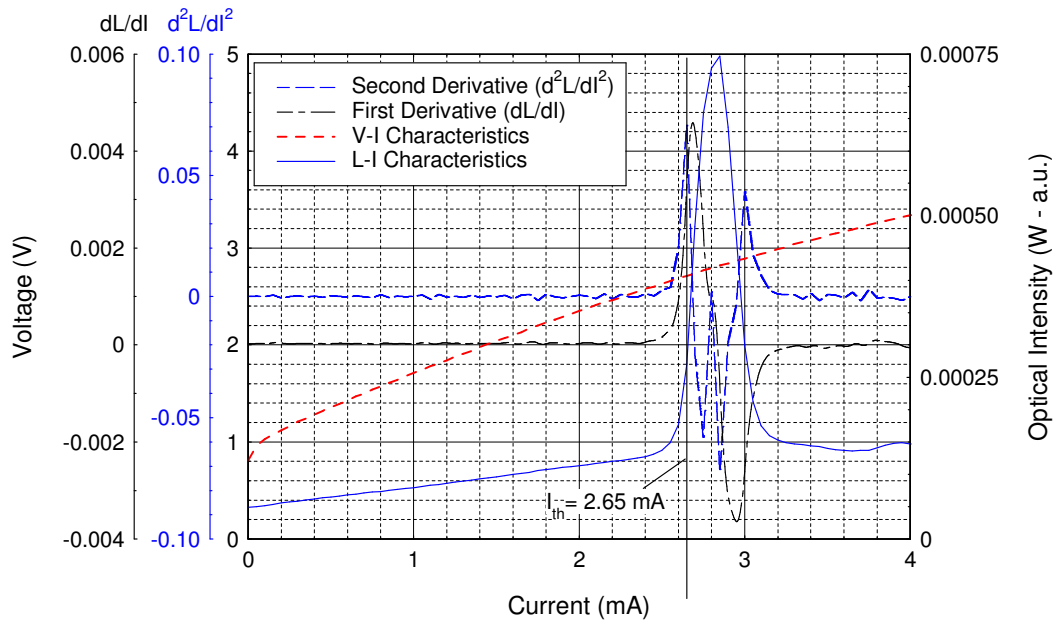


Figure 4.25: Output of a 25 μm DO177 VCSEL at room temperature (25°C) with a threshold current of 2.65 mA

The chuck temperature was set to 21 °C (room temperature) and the LIV measurements were repeated. The 25 μm DO177 VCSEL device output improved significantly and is shown in Figure 4.27. The threshold current dropped to 2.3 mA and the device lased over an increased range of current. A second lasing mode appeared at a drive current of about 3.6 mA. The wall plug efficiency peaked out at about 37% at a current of 2.66 mA. The biggest reason this device performed so well was likely because it was located near the edge of the wafer and therefore had a shorter cavity that was resonant closer to the peak of the gain curve.

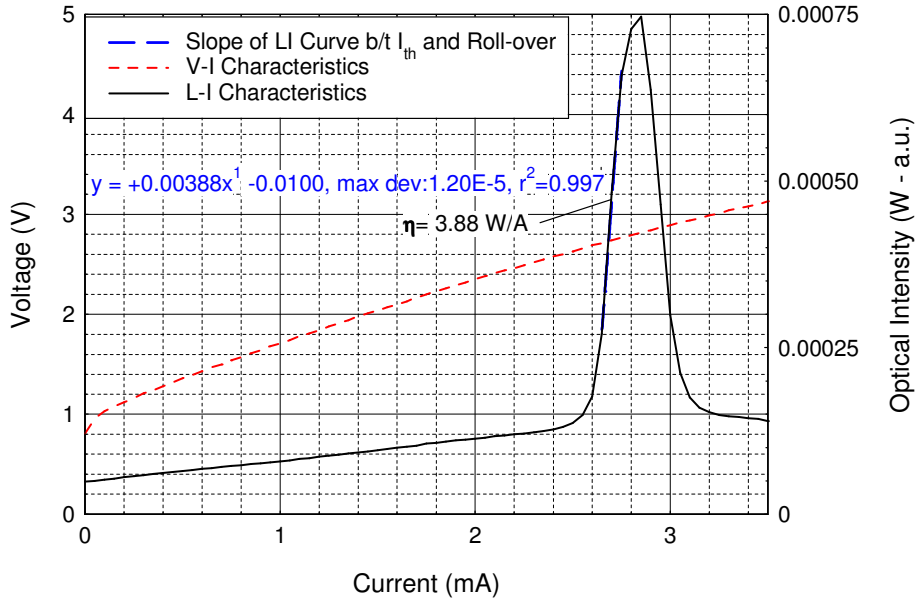


Figure 4.26: LIV of a 25  $\mu\text{m}$  DO177 VCSEL at a chuck temperature of 25°C

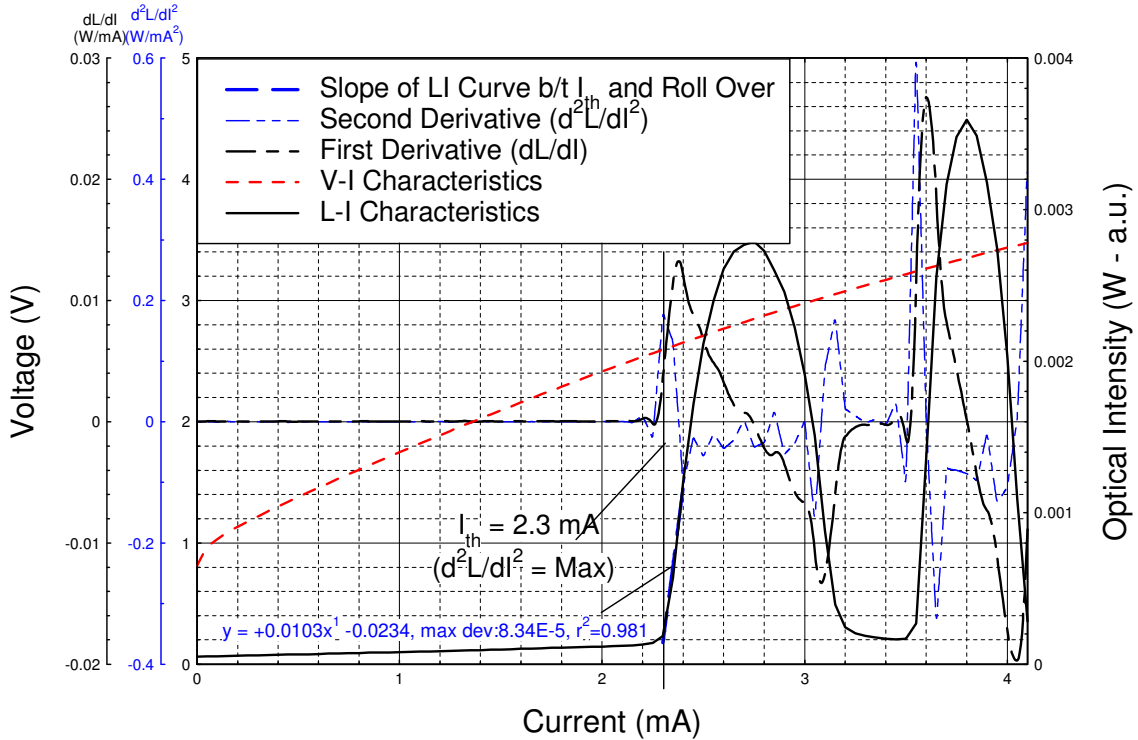


Figure 4.27: LIV of a 25  $\mu\text{m}$  DO177 VCSEL at a chuck temperature of 21°C (room temperature) with  $I_{\text{th}}$  of 2.3 mA and slope efficiency of 10.3 W/A

#### 4.6 Temperature Effects on LIV Curves and VCSEL Threshold Current

The LIV curve of the circular 25  $\mu\text{m}$  DO177 VCSEL was measured over a range of chuck temperatures from  $-30^\circ\text{C}$  to  $25^\circ\text{C}$ . Multiple lateral modes were observed, and the output level increases dramatically as the chuck temperature is reduced as seen in Figure 4.28. This is most likely due to the reduction in device losses that occurs as the

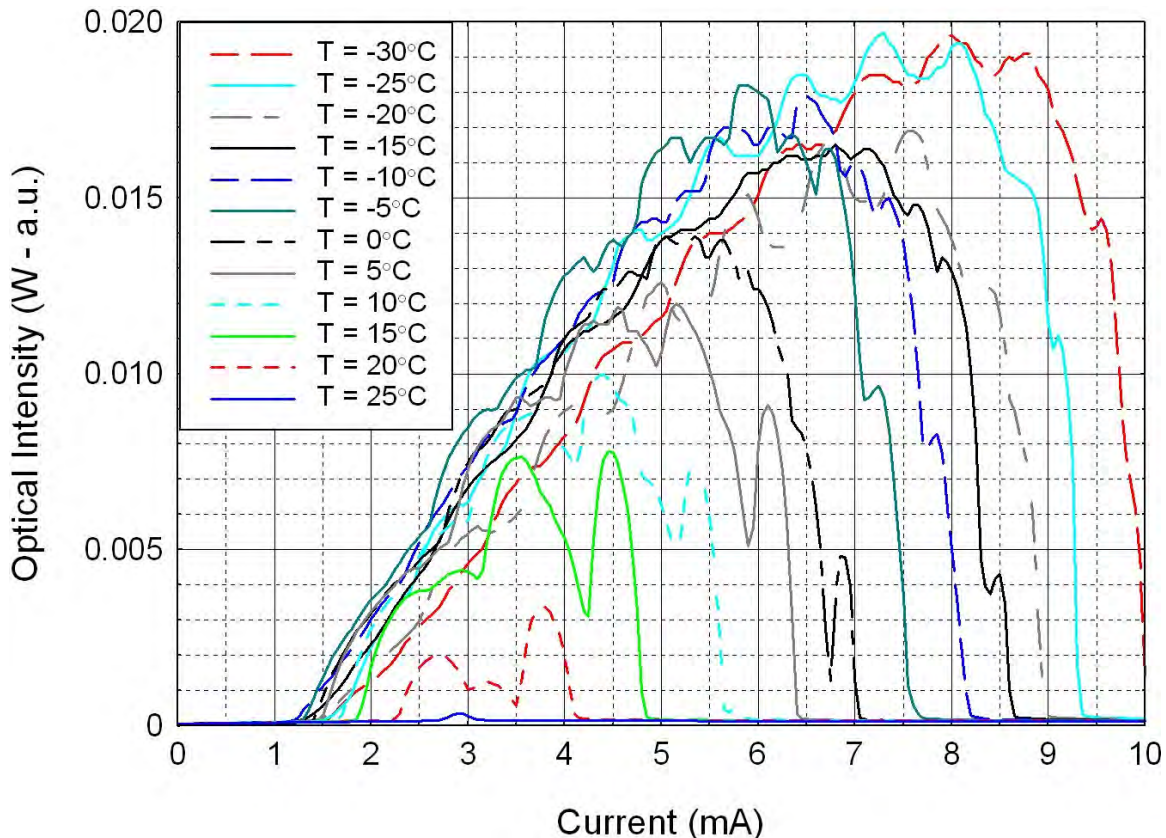


Figure 4.28: LIV plots of a 25  $\mu\text{m}$  DO177 VCSEL over a range of chuck temperatures (T)

temperature decreases since the gain curve and cavity resonance peaks should actually detune further with a decrease in temperature. The cavity peak changes at a rate slower than the change in the gain curve of the QD active region and both the cavity peak wavelength and the gain peak wavelength decrease with decreasing temperature. At room temperature the cavity peak is normally set at a wavelength longer than that of the gain

peak, so that the increase in active region temperature will align the two. However, it was difficult to determine the peak of the gain in the DO177 sample because I didn't have an RCLED device fabricated from it.

To examine the lateral modes of the device, the chuck temperature was set to a temperature of  $-30^{\circ}\text{C}$  and current levels along the LI curve were selected to measure the spectral output of the VCSEL at a bandwidth resolution of 0.1 nm. At this resolution, the separate lateral modes would be distinguishable. The points selected are shown on the LI curve in Figure 4.29 with green circles and they were generally selected point in which it appeared as though a single dominant mode existed at that point, and not at a point where a mode was rolling over (the LI curve was level or decreasing in slope).

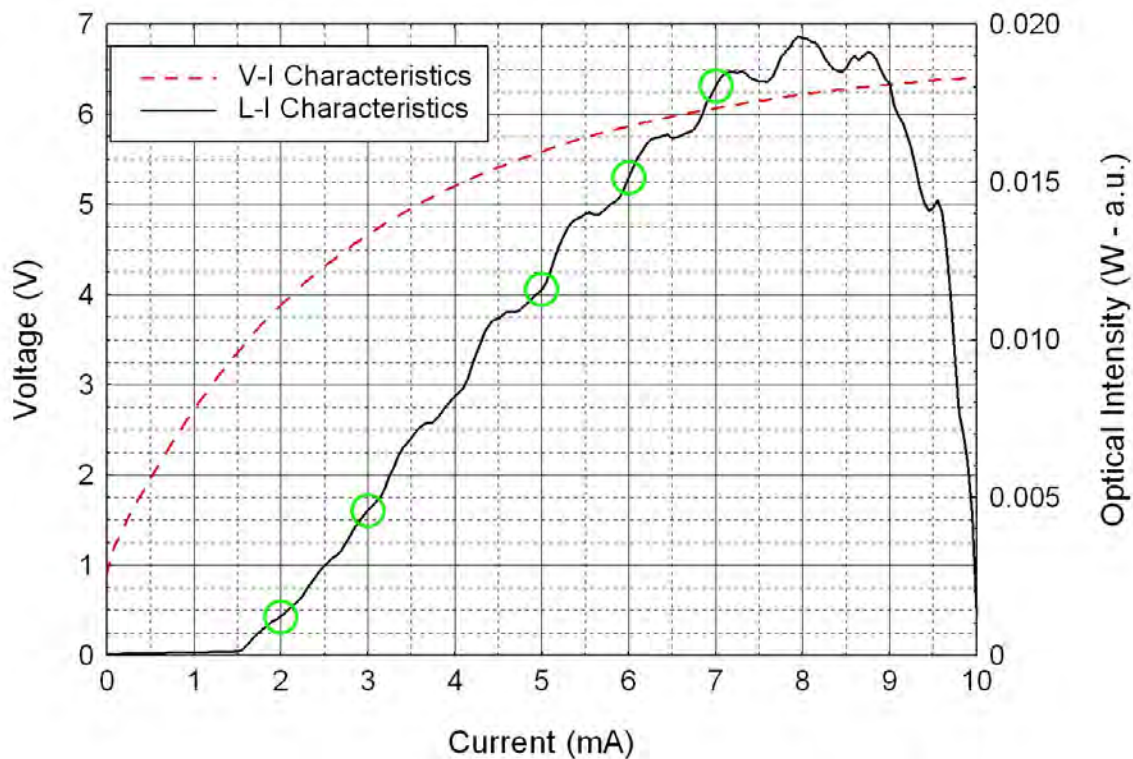


Figure 4.29: LIV plot of a 25  $\mu\text{m}$  DO177 VCSEL at a chuck temperature of  $-30^{\circ}\text{C}$  with markers where the output spectrum was measured

Figure 4.30 shows the spectrum of the output at the current levels marked on the LI curve in Figure 4.29. Some of the mode outputs got clipped on the graph because the device saturated the OSA and it wasn't apparent on the display at the time of the measurement. Even so, some shifts in wavelength and changes in which mode is largest occurs as the current through the device is increased. The device is lasing in multiple modes separated by 0.5 to 0.3 nm.

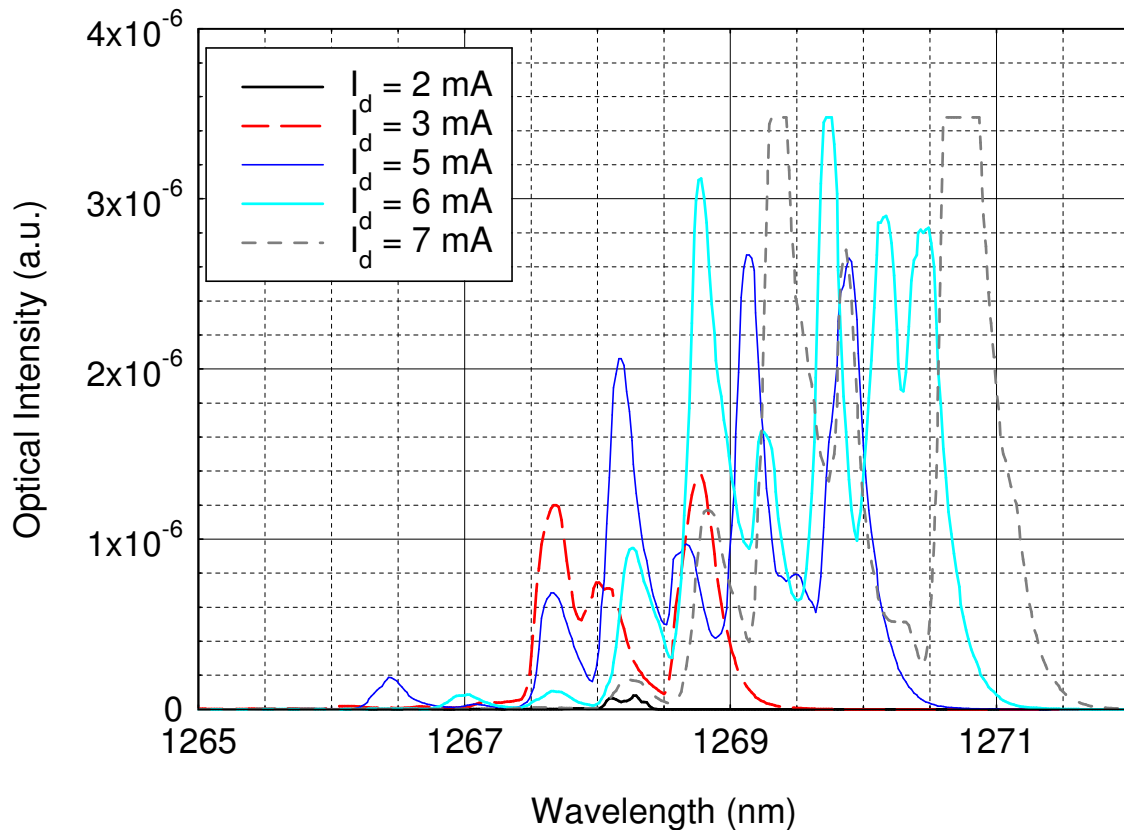


Figure 4.30: Multimode output spectrum of a 25  $\mu\text{m}$  DO177 VCSEL at a chuck temperature of  $-30^\circ\text{C}$  at various drive currents

To look at the effect of temperature on threshold and slope efficiency, a 25  $\mu\text{m}$  circular VCSEL device was placed on the temperature controlled chuck and the chuck temperature was set to temperatures between  $-30^\circ\text{C}$  and  $25^\circ\text{C}$ . LIV curves were taken,

and are shown on Figure 4.31 and zoomed in Figure 4.32 for the range of currents just above the threshold. The threshold current and slope of the LI curve are noticeably different at different temperatures. The threshold current and slope efficiency were determined for the LI curve at each temperature and shown on Figure 4.33. As the chuck temperature was decreased the threshold current decreased down to a minimum at a chuck temperature of  $-10^{\circ}\text{C}$ . Then the threshold current increased. Generally, the threshold current will depend largely on the alignment of the gain curve peak wavelength and the cavity peak wavelength (resonant wavelength).

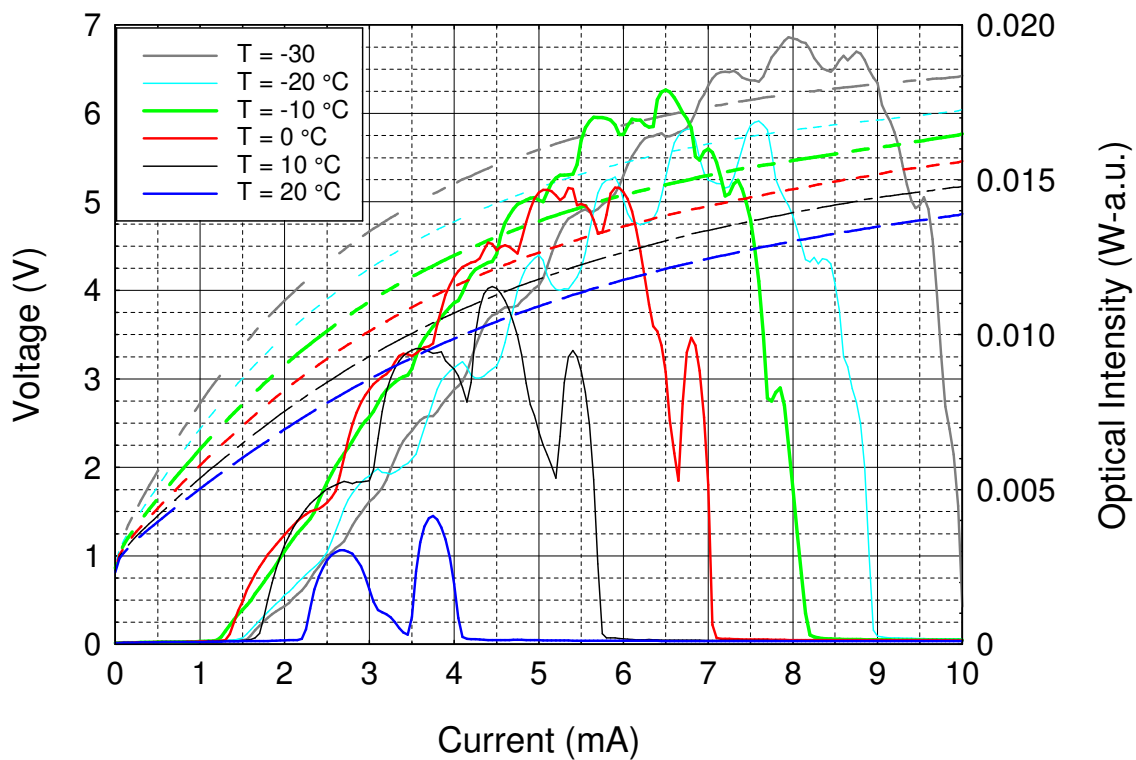


Figure 4.31: LIV plots of a  $25\ \mu\text{m}$  DO177 VCSEL over various chuck temperatures



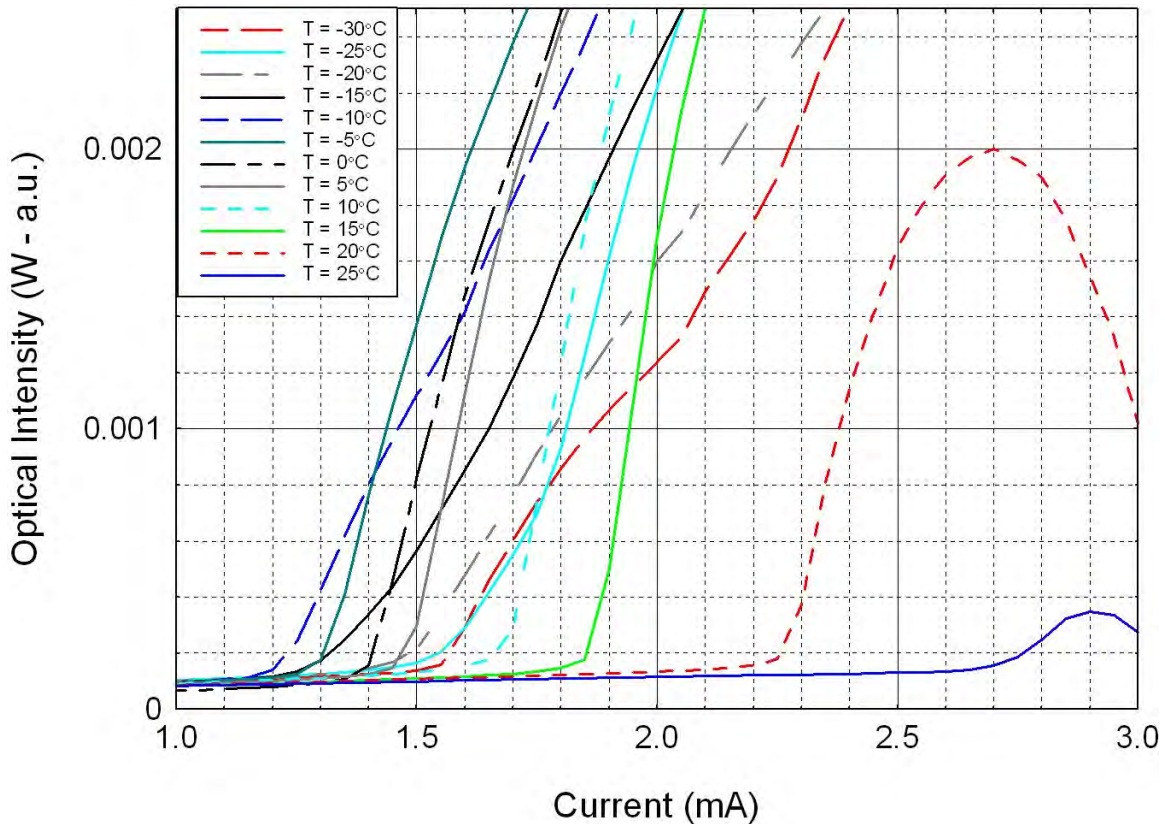


Figure 4.32: LIV plots of a 25  $\mu\text{m}$  DO177 VCSEL over various chuck temperatures at and around the threshold current level

The effect threshold current versus temperature shown in Figure 4.33 suggests that the gain curve and cavity peaks align best at somewhere close to  $-10^\circ\text{C}$ . The slope efficiency appears to increase as the temperature is increased but at a certain temperature, the device becomes in efficiency and the slope efficiency drops sharply. This can be explained by thermal losses in the device and non-radiative recombination decreasing the output of the device for a given current level.

The characteristic temperature, a measure of temperature insensitivity of the threshold current, for the 25  $\mu\text{m}$  DO177 VCSEL is shown in Figure 4.34. Equation 2.29 from chapter two was used with the temperature and threshold current data from Figure 4.33 and next higher temperature's data used as the reference temperature in the equation. Normally, with semiconductor diode lasers, the threshold current has a proportional and

exponential relationship between the threshold current and temperature. Typically the threshold current doesn't decrease with increasing  $T$ , and the characteristic temperature is taken with the temperature at operating range (i.e. 293 K) and the reference temperature at a much higher temperature representing the upper limit of operation (i.e. 277 K or 85°C). However, there was no lasing at temperatures much higher than room temperature, but if calculated using data at  $T = 297.15$  K, and  $T_{\text{ref}} = 242.15$  K then  $T_0 = 111$  K. Possibly a better measure would be to use the minimum threshold current and temperature at the minimum (i.e.  $T_{\text{ref}} = -10^\circ\text{C}$  or 262.15 K, and  $I_{\text{th-ref}} = 1.25$  mA), then  $T_0 = 49.4$  K. This would likely best describe the relationship between temperature and threshold current in the operating range of the laser if the cavity resonance was better

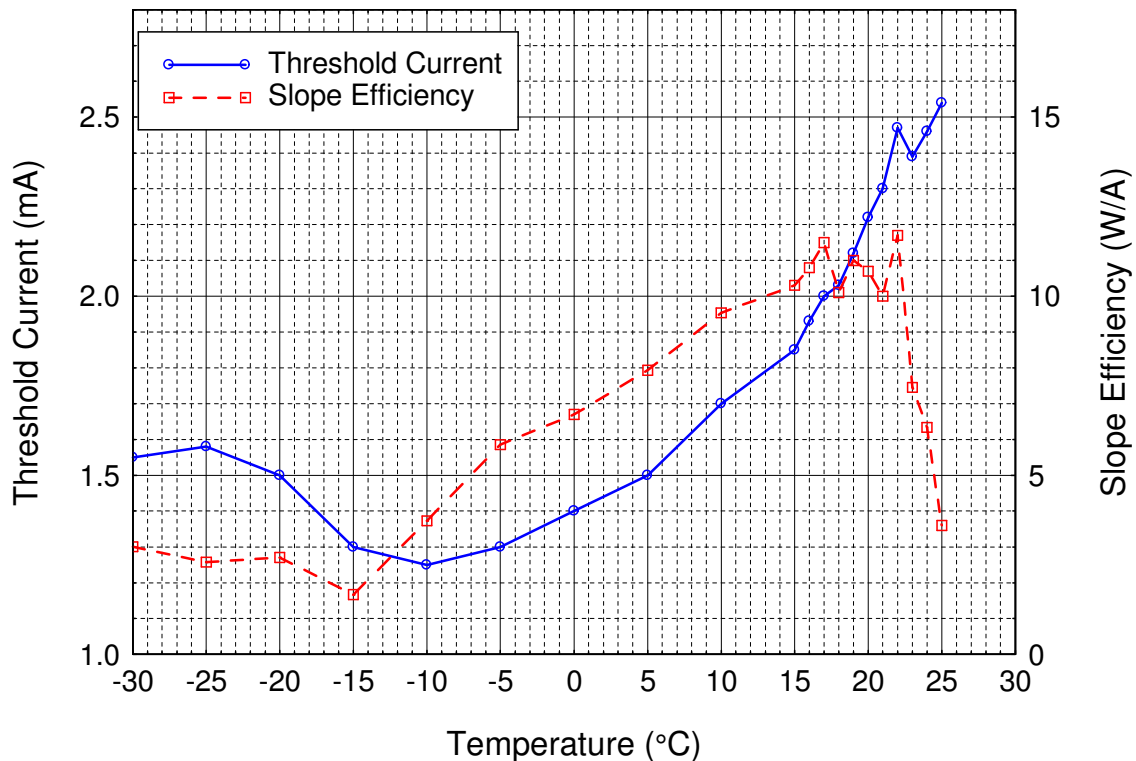


Figure 4.33: Threshold current and slope efficiency of a 25  $\mu\text{m}$  DO177 VCSEL over various chuck temperatures

tuned to the gain curve peak. In other words, the room temperature device performance would be better if the cavity resonance was at a slightly longer wavelength than the gain peak at room temperature instead of a slightly shorter wavelength. Using the active region temperature in this calculation would likely increase these values of  $T_0$  as long as the increase in temperature between the chuck and active region is close to the same at both temperatures because the ratio in the denominator of the  $T_0$  equation would decrease. VCSELs tend to have a greater difference between chuck and junction temperatures because the extremely small active regions have a higher current density and less area to dissipate heat than edge emitting lasers.

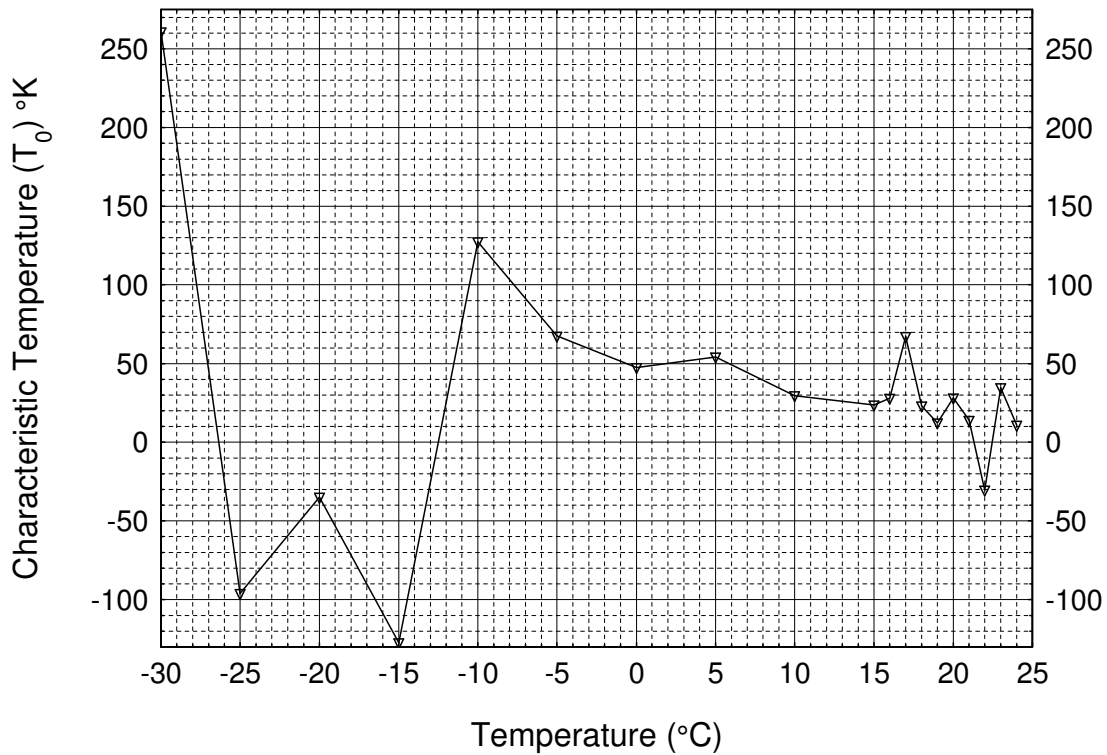


Figure 4.34: Characteristic temperature of a 25  $\mu\text{m}$  DO177 VCSEL over various chuck temperatures

To characterize the effect of temperature on the DO177 VCSEL cavity peak wavelength, the output of a 15  $\mu\text{m}$  diameter VCSEL at 4 mA current was coupled into the HP OSA at different chuck temperatures as shown in Figure 4.34. The peak wavelength of the same individual mode was measured at each temperature and the data was plotted versus wavelength (nm) and energy (eV) as shown in Figure 4.35. The DO177 VCSEL cavity peak varies at close to the same rate as the cavity peak in the V17 VCSEL this would be expected as the devices are fabricated of similar materials even though DO177 has a shorter cavity length ( $2\lambda$  versus the  $6\lambda$  cavity in V17).

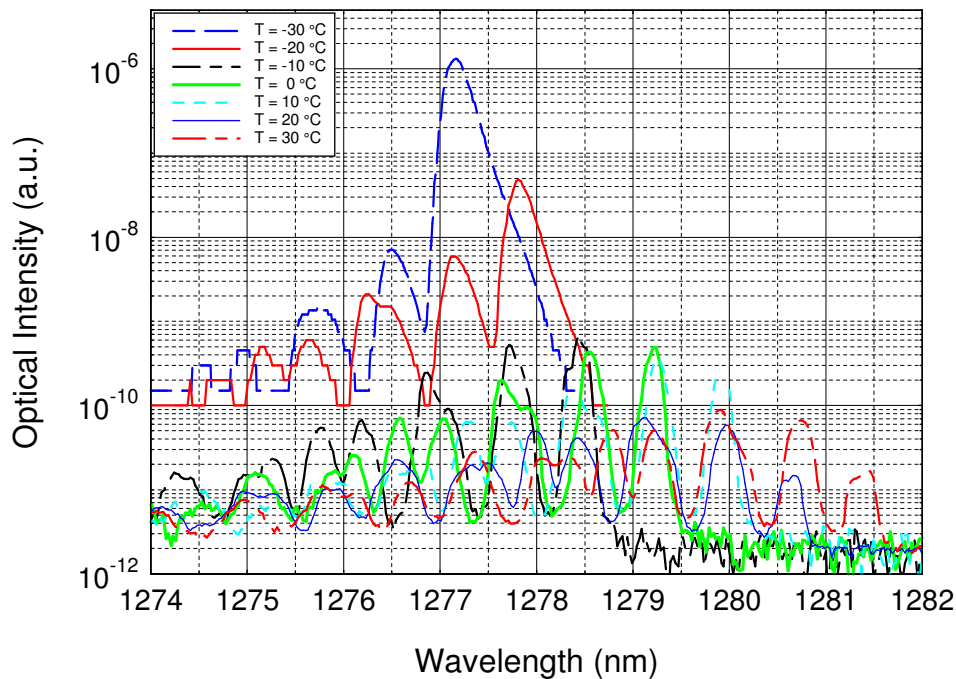


Figure 4.35: Output of a 15  $\mu\text{m}$  DO177 VCSEL at  $I_d = 4 \text{ mA}$  over various chuck temperatures in a log scale

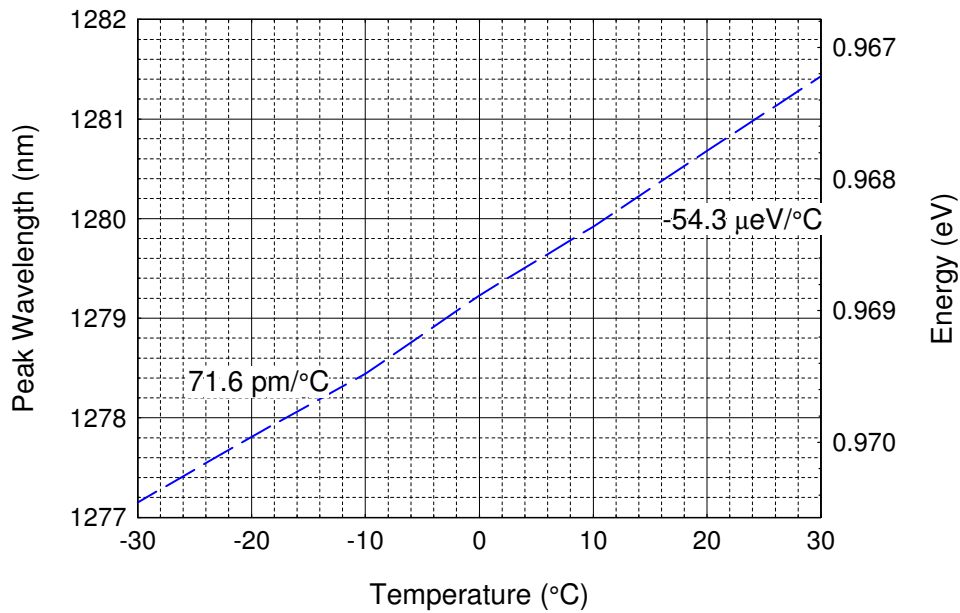


Figure 4.36: Cavity resonance wavelength of a 15  $\mu\text{m}$  DO177 VCSEL at  $I_d = 4 \text{ mA}$  versus chuck temperature

#### 4.7 Summary of Results

In this chapter, the results of experiments conducted on three VCSEL samples and one RCLED sample that included optical transmission measurements and electroluminescence measurements examined over various currents and temperature ranges were presented. Optical transmission characteristics were studied for three VCSEL devices and compared with the computer models developed to represent those devices. The models matched well with the measured results and required only a slight adjustment of the model layer thicknesses to align the power transmission plots. Differences in the calculated and actually material indices of refraction could explain the difference.

The electroluminescence of the SH118 RCLED was investigated to characterize the QD active region over a range of current and temperature. The RCLED active region showed a separation between the QD GS and ES of 62 meV which should provide for a

large amount of insensitivity to changes in device temperature. Over a range of device temperatures, the output amplitude of the RCLED varied considerably. However, the EL output remained relatively proportional over the entire range of photon energies. The active region showed good temperature stability as the peak energy of the EL curve changed at a rate over four times smaller than the rate of change of the GaAs band gap energy versus temperature over a range from 15°C to 60°C.

The electroluminescence output of NSC336, V17, and DO177 VCSEL devices was characterized to determine shortfalls and find ways to improve the performance of future devices. The AlAs oxide apertures were very successful at current confinement and less successful at optical confinement in the active region. Optical confinement seemed more sensitive to the uniformity in the depth of the oxide layer. Smaller devices had more success with lasing, especially at higher temperatures. Some DO177 VCSELs lased at room temperature but the cavity resonance was aligned at too short a wavelength for the gain curve at higher device temperatures. Cooling the devices increased the device output very significantly since the gain curve and cavity resonance aligned at lower temperatures of around 10°C. Even so, room temperature lasing with a threshold current of 2.3 mA and a slope efficiency of 10.3 W/A was achieved in a DO177 VCSEL device. The characteristic temperature of a 25µm DO177 VCSEL varied drastically with temperature, but was 49.4 K between two temperatures where the laser displayed the typical proportional exponential relationship to temperature ( $T = -10^{\circ}\text{C}$ ,  $T_{\text{ref}} = 25^{\circ}\text{C}$ ).

Multiple lateral cavity modes were observed in all the VCSEL devices. The DO177 VCSEL even lased in more than one mode simultaneously. Most Mode spacing in the cavity was about 0.6 nm and 0.35 nm. Finally, Wall plug efficiency at room temperature was greater than 36% and increased inversely with temperature.

## V. Conclusions and Recommendations

The long wavelength GaAs/AlGaAs based microcavity devices in this study proved difficult to fabricate due to the need for deep dry etch processes with precise stopping points. The high aspects of the mesas complicated the application of metal contacts. Photolithography with silicon nitride ( $\text{Si}_3\text{N}_4$ ) masking proved essential to dry etching the devices since typical photoresist was not robust enough to withstand the full etching process of greater than about  $2\ \mu\text{m}$  deep. Multiple layers of photoresist only complicated fabrication and it proved difficult to remove all the photoresist residue. Reflectance monitoring during the dry etch was also essential for the depth and precision VCSEL devices. After these adjustments in the fabrication process, long wavelength GaAs/AlGaAs microcavity devices with quantum dot (QD) active regions were successfully fabricated and then characterized.

The optical transmission of the microcavity structures was measured and matches well with the calculated values in a Matlab model. Uncertainty in the index of refraction likely drove differences that were noted as there are many sources of refractive index data that had slight differences in values over the device wavelength range. Differences in the layer thicknesses between nominal and actual values also could have been a factor since varying the layer thicknesses of the model helped to better match it with the measured optical transmission. The stop bands of all the devices were sufficiently matched to the range of wavelengths emitted by the devices. Studying the effects of temperature on the optical transmission and absorption of the devices may help to better align the optical cavity with the laser gain curve, and also characterize thermally induced optical losses to improve the output power of the lasers.

The InAs QDs in the RCLED active region emitted light at a peak wavelength of 1282nm (0.9668 eV) from the ground state QD transition at room temperature, and

showed a temperature dependence of  $-82 \mu\text{eV}/\text{K}$ . The peak excited state transition was about 62 meV above the ground state at 1.028 eV. This appeared to be a large enough gap to avoid undesired thermal excitation from the ground state, since effects of thermal excitation were not apparent as the temperature of the device was increased. The FWHM of the GS was about 27 meV, indicating that the QDs in the active region had good uniformity. Further studies with new VCSELs grown with a longer cavity resonant wavelength (tuned slightly above the peak gain) would be helpful since the microcavity resonance of these devices was tuned too below the peak wavelength of the gain curve. Reducing thermal losses would also improve the device performance since temperature had such a profound effect on the output level.

Vertical cavity surface emitting lasers with aluminum oxide InAs quantum dot active regions emitting near  $1.28 \mu\text{m}$  were fabricated and characterized. The VCSELs demonstrated continuous wave lasing at room temperature at power levels above 3 mW with a threshold current of 2.3 mA and slope efficiency of 10.3 mW/mA. The characteristic temperature was 49.4 K over a range of  $-10^\circ\text{C}$  to room temperature where the laser demonstrated a consistent change in the threshold current. The minimum threshold current was 1.25 mA at a chuck temperature of  $-10^\circ\text{C}$ . A study into determining the junction temperature or active region temperature would be beneficial to really understand the temperature characteristics of these devices. The temperature of the active region varies significantly with the device current because of the relatively small active region and the high thermal resistance of the VCSEL structures.

A study on direct high-speed modulation of these devices or a pulsed operation study would be beneficial to characterizing how well these devices might perform for high speed data links. If higher order transverse modes are still present in pulsed operation, then studying ways to inhibit the transverse modes would also be useful.



## Bibliography

1. Yoo, Hoi-Jun, A. Sherer, J.P. Harbison, L.T. Florez, E.G. Paek, B.P. Van der Gaag, J.R. Hayes, A. Von Lehmen, E. Kapon and Young-Se Kwon. "Fabrication of a two-dimensional phased array of vertical-cavity surface emitting lasers" *Applied Physics Letters*, Volume 56, Number 4, 1990, Pages 1198-1200.
2. Geib, K.M. Choquette, K.D. Serkland, D.K. Allerman, A.A. Hargett, T.W. "Fabrication and performance of two-dimensional matrix addressable arrays of integrated vertical-cavity lasers and resonant cavity photodetectors" *IEEE Journal of Selected Topics in Quantum Electronics*, Volume 8, Issue 4, 2002, Pages 943-947.
3. Krstajić, N., L.E. Smith, S.J. Matcher, D.T.D. Childs, M. Bonesi, P.D.L. Greenwood, M. Hugues, K. Kennedy, M. Hopkinson, K.M. Groom, S. MacNeil, R.A. Hogg, R. Smallwood. "Quantum Dot Superluminescent Diodes for Optical Coherence Tomography: Skin Imaging" *IEEE Journal of Selected Topics in Quantum Electronics*, Volume 16, Number 4, 2010, Pages 748-754.
4. Hofmann, W., M.C. Amann. "Long-wavelength vertical-cavity surface-emitting lasers for high-speed applications and gas sensing" *Institute of Engineering and Technology, Optoelectronics*, Volume 2, Number 3, 2008, Pages 134-142.
5. Lytkine, A., B. Lau, A. Lim, W. Jäger and J. Tulip. "Range-resolved gas concentration measurements using tunable semiconductor lasers" *Applied Physics B: Lasers and Optics*, Volume 90, Number 2, 2008, Pages 339-343.
6. Nozik, A.J. "Quantum dot solar cells" *Physica E: Low-dimensional Systems and Nanostructures* Volume 14, Issues 1-2, April 2002, Pages 115-120.
7. Okada, Y., et al. "Characteristics of InAs/GaNAs strain-compensated quantum dot solar cell" *J. of Applied Physics* Volume 106, 024306, July 2009, 3 pages.
8. Guimard, D., R. Morihara, D. Bordel, K. Tanabe, Y. Wakayama, et al. "Fabrication of InAs/GaAs quantum dot solar cells with enhanced photocurrent and without degradation of open circuit voltage" *Applied Physics Letters* Volume 96, 203507, May 2010, 3 pages.
9. Rowe, M. A., E. J. Gansen, M. Greene, R. H. Hadfield, T. E. Harvey, M. Y. Su, S. W. Nam, R. P. Mirin and D. Rosenberg. "Single-photon detection using a quantum dot optically gated field-effect transistor with high internal quantum efficiency" *Applied Physics Letters*, Volume 89, Issue 25, 2006, Pages 1198-1200.

10. Henini, M. "Quantum dot nanostructures" *Materials Today*, Volume 5, Issue 6, 2002, Pages 48-53.
11. Marent, A., M. Geller and D. Bimberg. "A novel nonvolatile memory based on self-organized quantum dots" *Microelectronics Journal*, Volume 40, Issue 2, 2009, Pages 492-495.
12. Hecht, Eugene. *Optics (Fourth Edition)*, San Francisco: Addison Wesley 2002.
13. Saleh, B.E.A. and M.C. Teich. *Fundamentals of Photonics*. . New York: John Wiley & Sons, Inc., 1991.
14. MacCloud, H Angus. *Thin-Film Optical Filters(Third Edition)*. London: The Institute of Physics Publishing, 2002.
15. Guden, M. and J. Piprek, "Material Parameters of Quaternary III-V Semiconductors for Multilayer Mirrors at 1.55-micron Wavelength," *Modeling and Simulation in Materials Science and Engineering*, 6: 349-357 (1996).
16. Wilmsen, Carl, Henryk Temkin, and Larry A. Coldren. *Vertical-Cavity Surface-Emitting Lasers*. New York: Cambridge University Press, 1999.
17. Ustinov, Victor M., Alexey E. Zhukov, Anton Yu. Egorov, and Nikolai A. Maleev. *Quantum Dot Lasers*. New York: Oxford University Press, 2003.
18. Venables, John A. *Introduction to Surface and Thin Film Processes*. United Kingdom: Cambridge University Press, 2000.
19. Chen, J.X., et al. "Tuning InAs/GaAs quantum dot properties under Stranski-Krastanov growth mode for 1.3  $\mu\text{m}$  applications," *Journal of Applied Physics*, 91: 10 6710-6716 (2002).
20. Gong, Q, R. Notzel, P. J. van Veldhoven, T. J. Eijkemans, and J. H. Wolter. "Wavelength tuning of InAs quantum dots grown on InP (100) by chemical-beam epitaxy" *Applied Physics Letters*, Volume 84, Number 2, 2003, Pages 275-277.
21. Hsu, T. M., Y. S. Lan, W.-H. Chang, N. T. Yeh and J.-I. Chyi. "Tuning the energy levels of self-assembled InAs quantum dots by rapid thermal annealing" *Applied Physics Letters*, Volume 77, Number 4, 2000, Pages 466-468.
22. Franchi, S., G. Trevisi, L. Seravalli, and P. Frigeri. "Quantum dot nanostructures and molecular beam epitaxy," *Progress in Crystal Growth and Characterization of Materials*, Volume 47, Issues 2-3, 2003, Pages 166-195.

23. Grundmann, M., O. Stier, and D. Bimberg. "InAs/GaAs pyramidal quantum dots: Strain distribution, optical phonons, and electronic structure" *Physical Review B*, Volume 52, Number 16, 1995, Pages 11969-11988.
24. Shchekin, O., G. Park, D. Huffaker, and D. Deppe. "Discrete energy level separation and the threshold temperature dependence of quantum dot lasers" *Applied Physics Letters*, Volume 77, Number 4, 2000, Pages 466-468.
25. Bimberg, D., M. Grundmann and N.N. Ledentsov. *Quantum Dot Heterostructures*. New York: Wiley & Sons, Inc., 1999.
26. Yu, Siu F. *Analysis and Design of Vertical Cavity Surface Emitting Lasers*. Hoboken, New Jersey: John Wiley & Sons, Inc., 2003.
27. Blokhin, S. A., A. V. Sakharov, N. A. Maleev, A. G. Kuz'menkov, I. I. Novikov, N. Yu. Gordeev, Yu. M. Shernyakov, M. V. Maximov, V. M. Ustinov, A. R. Kovsh, S. S. Mikhrin, N. N. Ledentsov, G. Lee, and J. Y. Chi. "Experimental study of temperature dependence of threshold characteristics in semiconductor VCSELs based on submonolayer InGaAs QDs" *Semiconductors*, Volume 40, Number 10, 2006, Pages 1232-1236
28. Ding, Y., W.J. Fan, D.W. Xu, C.Z. Tong, L.J. Zhao, W. Wang, D.S. Li, B.S. Ma, S.F. Yoon, and D.H. Zhang. "Investigation of Temperature Characteristics for 1.3- $\mu\text{m}$  InAs Quantum Dot VCSELs with Planar Electrodes Configuration" *Semicond. Sci. Technol.*, Volume 22, 2007, Pages 203–208.
29. Blokhin, S A, et al. "The impact of thermal effects on the performance of vertical-cavity surface-emitting lasers based on sub-monolayer InGaAs quantum dots" *Semicond. Sci. Technol.*, Volume 22, 2007, Pages 203–208
30. Yokouchi, N., A. J. Danner, and K. D. Choquette. "Two dimensional photonic crystal confined vertical cavity surface emitting lasers" *IEEE Journal of Quantum Electronics*, Volume 43, Number 12, 2007, Pages 1140-1146
31. Jin, C Y, H. Y. Liu, K. M. Groom, Q. Jiang, M. Hopkinson, T. J. Badcock, R.J. Royce, and D. J. Mowbray. "Effects of photon and thermal coupling mechanisms on the characteristics of self-assembled InAs/GaAs quantum dot lasers" *Physical Review B*, Volume 76, Number 8, 2007, Pages 085315-1 to 085315-12
32. Badcock, T. J., R. J. Royce, D. J. Mowbray, M.S. Skolnick, H. Y. Liu, M. Hopkinson, K. M. Groom, and Q. Jiang. "Low threshold current density and negative characteristic temperature 1.3  $\mu\text{m}$  In As self-assembled quantum dot lasers" *Applied Physics Letters*, Volume 90, Number 11, 2007, 111102-1 (3 pages)

33. Sandall, I. C., P. M. Snowton, J.D. Thomson, T. Badcock, D. J. Mowbray, H. Y. Liu, and M. Hopkinson. "Temperature dependence of threshold current in p-doped quantum dot lasers" *Applied Physics Letters*, Volume 89, Number 15, 2007, 151118-1 (3 pages)
34. Fathpour, S., Z. Mi, and P. Bhattacharya. "The role of Auger recombination in the temperature-dependent output characteristics ( $T_0 = \infty$ ) of p-doped 1.3  $\mu\text{m}$  quantum dot lasers" *Applied Physics Letters*, Volume 85, Number 22, 2004, Pages 5164-5166
35. Marko, I. P., A. D. Andreev, A. R. Adams, R. Krebs, J. P. Reithmaier, and A. Forchel. "The Importance of Auger recombination in InAs 1.3  $\mu\text{m}$  quantum dot lasers" *Electronics Letters*, Volume 39, Number 1, 2003, Pages 58-59
36. Yang, H. P. D., I. C. Hsu, F. I. Lai, G. Lin, R. S. Hsiao, N. A. Maleev, S. A. Blokhin, H. C. Kuo, S. C. Wang and J. Y. Chi. "Single-mode InGaAs submonolayer quantum dot photonic crystal VCSELs" *Semicond. Sci. Technol.*, Volume 21, 2006, Pages 1176–1180
37. Haglund, A., J. S. Gustavsson, J. Vukusic, P. Modh, A. Larsson. "Single fundamental-mode output power exceeding 6 mW from VCSELs with a shallow surface relief" *IEEE Photonics Technology Letters*, Volume 16, Issue 2, 2004, Pages 368-370
38. Yokouchi, N., A. J. Danner, and K. D. Choquette. "Two dimensional photonic crystal confined vertical cavity surface emitting lasers" *IEEE Journal of Selected Topics in Quantum Electronics*, Volume 9, Number 5, 2003, Pages 1439-1445
39. Birkedal, D., N. Gregersen, S. Bischoff, M. Madsen, F. Romstad, and J. Oestergaard. "Large-Area Single-Mode Photonic Bandgap VCSELs" 2003 *Proc. Of Optical Fiber Comm. Conf.*, Volume 1, Pages 83-85
40. Maciej Kuc, Robert P. Sarzala, and Wlodzimierz Nakwaski. "Physics of mode selectivity of vertical-cavity surface-emitting diode lasers" *Journal of Applied Physics*, Volume 108, Issue 4, 2010, Pages 044501-1 – 044501-8.
41. Deri, R. J., and M. A. Emanuel. "Consistent formula for the refractive index of  $\text{Al}_x\text{Ga}_{1-x}\text{As}$  below the band edge" *Journal of Applied Physics*, Volume 77, Number 9, 1995, Pages 4667-4672.
42. Blakemore, J. S. "Semiconducting and other major properties of gallium arsenide" *Journal of Applied Physics*, Volume 53, Number 10, 1982, DOI: 10.1063/1.331665.

REPORT DOCUMENTATION PAGE			Form Approved OMB No. 074-0188		
The public reporting burden for this collection of information is estimated to average 1 hour per response, including the time for reviewing instructions, searching existing data sources, gathering and maintaining the data needed, and completing and reviewing the collection of information. Send comments regarding this burden estimate or any other aspect of the collection of information, including suggestions for reducing this burden to Department of Defense, Washington Headquarters Services, Directorate for Information Operations and Reports (0704-0188), 1215 Jefferson Davis Highway, Suite 1204, Arlington, VA 22202-4302. Respondents should be aware that notwithstanding any other provision of law, no person shall be subject to a penalty for failing to comply with a collection of information if it does not display a currently valid OMB control number. <b>PLEASE DO NOT RETURN YOUR FORM TO THE ABOVE ADDRESS.</b>					
1. REPORT DATE (DD-MM-YYYY) 22-12-2011		2. REPORT TYPE Master's Thesis		3. DATES COVERED (From - To) Aug 2002 to Dec 2011	
4. TITLE AND SUBTITLE Electroluminescence Studies on Longwavelength Indium Arsenide Quantum Dot Microcavities Grown on Gallium Arsenide			5a. CONTRACT NUMBER		
			5b. GRANT NUMBER		
			5c. PROGRAM ELEMENT NUMBER		
6. AUTHOR(S) Ramsey, John C			5d. PROJECT NUMBER N/A		
			5e. TASK NUMBER		
			5f. WORK UNIT NUMBER		
7. PERFORMING ORGANIZATION NAMES(S) AND ADDRESS(S) Air Force Institute of Technology Graduate School of Engineering and Management (AFIT/EN) 2950 Hobson Way Wright Patterson AFB, OH 45433			8. PERFORMING ORGANIZATION REPORT NUMBER AFIT/GE/ENG/11-46		
9. SPONSORING/MONITORING AGENCY NAME(S) AND ADDRESS(ES) Electro-Optic Components Branch, Sensors Directorate, Air Force Research Laboratory Thomas Nelson, Branch Chief 2241 Avionics Circle Wright-Patterson AFB, OH 45433-7301 (937) 938-8710 (DSN: 798-8710) Thomas.Nelson@wpafb.af.mil			10. SPONSOR/MONITOR'S ACRONYM(S) AFRL/RYPD		
			11. SPONSOR/MONITOR'S REPORT NUMBER(S)		
12. DISTRIBUTION/AVAILABILITY STATEMENT APPROVED FOR PUBLIC RELEASE; DISTRIBUTION IS UNLIMITED					
13. SUPPLEMENTARY NOTES This material is declared work of the U.S. Government and is not subject to copy right protection in the United States.					
14. ABSTRACT A comprehensive study of the electroluminescence of four GaAs/AlGaAs microcavity devices with InAs/GaInAs quantum dot active regions emitting near 1.3 μm was conducted. The four molecular beam epitaxial grown samples with AlAs oxide aperture confinement layers were fabricated, characterized, and optically modeled. Optical power transmission of the samples was modeled using Matlab and compared with measured transmission data. Resonant cavity light emitting diodes (RCLEDs) and three vertical cavity surface emitting laser (VCSEL) samples were fabricated and electro-optically characterized over a range of injection currents and temperatures. Devices achieved continuous wave room temperature lasing at 1.28μm with an output power of more than 3 mW, a threshold current of 2.3 mA, and a slope efficiency of 10.3 W/A. The characteristic temperature was 49.4 K and the wall plug efficiency at was a maximum of over 36%. The minimum threshold current, 1.25 mA, was at a temperature of -10°C. The cavity resonance wavelength was tuned too short for the peak wavelength of the active region gain curve which limited the temperature at which the VCSELs produced lasing to about room temperature.					
15. SUBJECT TERMS VCSEL, Quantum Dot, InGaAs, AlGaAs, Semiconductor Laser, Microcavity, RCLED.					
16. SECURITY CLASSIFICATION OF:		17. LIMITATION OF ABSTRACT UU	18. NUMBER OF PAGES 124	19a. NAME OF RESPONSIBLE PERSON Dr. Ronald A. Coutu, Jr.	
REPORT U	ABSTRACT U			c. THIS PAGE U	19b. TELEPHONE NUMBER (Include area code) (937) 255-3636, X7230 ronald.coutu@afit.edu

Standard Form 298 (Rev: 8-98)  
Prescribed by ANSI Std. Z39-18